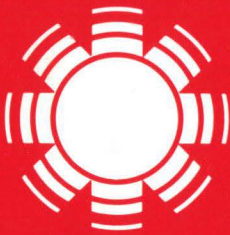


# Photovoltaic Research Branch Semiannual Report

---

Period Covered: 1 October 1979  
to 31 March 1980

Alex Zunger, Editor



# SERI

**Solar Energy Research Institute**

A Division of Midwest Research Institute

1617 Cole Boulevard  
Golden, Colorado 80401

Operated for the  
**U.S. Department of Energy**  
under Contract No. EG-77-C-01-4042

Printed in the United States of America  
Available from:  
National Technical Information Service  
U.S. Department of Commerce  
5285 Port Royal Road  
Springfield, VA 22161

Price:

Microfiche \$3.00

Printed Copy \$6.50

NOTICE

This report was prepared as an account of work sponsored by the United States Government. Neither the United States nor the United States Department of Energy, nor any of their employees, nor any of their contractors, subcontractors, or their employees, makes any warranty, express or implied, or assumes any legal liability or responsibility for the accuracy, completeness or usefulness of any information, apparatus, product or process disclosed, or represents that its use would not infringe privately owned rights.

SERI/PR-611-737  
UC CATEGORY: UC-63

PHOTOVOLTAIC RESEARCH BRANCH  
SEMIANNUAL REPORT

PERIOD COVERED: 1 OCTOBER 1979  
TO 31 MARCH 1980

ALEX ZUNGER, EDITOR

JULY 1980

PREPARED UNDER TASK NO. 3221.10

**Solar Energy Research Institute**

1536 Cole Boulevard  
Golden, Colorado 80401

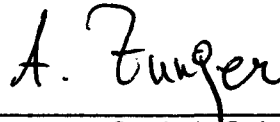
A Division of Midwest Research Institute

Prepared for the  
U.S. Department of Energy  
Contract No. EG 77-C-01-4042

## PREFACE

This report summarizes the research activities in the Photovoltaic Research Branch during the period 1 October 1979 to 31 March 1980.

I would like to express my thanks to the members of the Photovoltaic Research Branch for their invaluable help in editing the individual sections of the report.

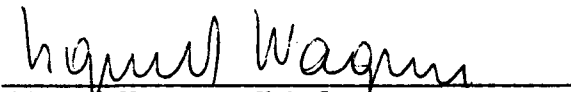


---

Alex Zunger, Senior Scientist  
Report Editor

Approved for:

SOLAR ENERGY RESEARCH INSTITUTE



---

Sigurd Wagner, Chief  
Photovoltaic Research Branch



---

Donald Feucht, Manager  
Photovoltaics Division

## EXECUTIVE SUMMARY

This report covers the research activities in SERI's Photovoltaic Research Branch during the period 1 October 1979 to 31 March 1980. It includes reports on solid-state theory, high-efficiency cells, thin-film cells, silicon purification, silicon crystallization, thick-film technology, surface and interface analysis, and growth of GaAs and related compounds by metal-organic chemical vapor deposition.

Each separate report summarizes the scientific and technical aspect of the research done during the reporting period, emphasizing the purpose behind the project, its status, significant results, and assessment of future research directions. Included in each report is a list of references that describe each project in greater detail.

The major issues covered in this report are:

(1) Solid-state theory:

This effort is intended to obtain a fundamental understanding of the systems and physical processes underlying photovoltaic solar cells. This includes the understanding of electronic states at semiconductor surfaces, semiconductor interfaces, metal-semiconductor junctions, and the effects of various defects on these. The present report includes discussions on development of reliable pseudopotentials for semiconductors; development of theoretical techniques for solving the electronic structure problem of surfaces and interfaces; applications to the relaxed GaAs (110) surface; application to the Ge-GaAs and ZnSe-GaAs heterojunctions; theoretical systematization of structural properties of binary compounds; transition metal impurities in bulk semiconductors; systematization of energy levels of point defects in semiconductors; theory of Schottky-barrier formation; computer modeling of the electronic structure of defects at heterojunctions; and the theory of metal-semiconductor transitions in doped semiconductors.

(2) Cascade solar cells:

This research is aimed at studying the properties of coupled solar cells having semiconductors of different band gaps. It includes LPE growth of  $\text{Ga}_{1-x}\text{Al}_x\text{As}$  layers, photoluminescence studies of the alloys establishing the variations of band edges with composition, and design of tunnel diodes from this material (including selection of doping).

(3) Photovoltaic properties of  $\text{Si-V}_2\text{O}_5$  and  $\text{GaAs-V}_2\text{O}_5$ :

This study investigates the photovoltaic properties of junctions between  $\text{V}_2\text{O}_5$  and "conventional" semiconductors such as Si and GaAs. The cell characteristics have been measured as well as the photo-response. Improvement of these values by doping was examined. The optical spectra of the  $\text{V}_2\text{O}_5$  films was measured. In addition, fabrication and investigation of Ge-GaAs heterostructures made by epitaxial alloying was initiated.

(4) Growth of GaAs by metal-organic chemical vapor deposition (MOCVD):

The potential and properties of the MOCVD method for growing layers of III-V compounds have been studied. A CVD system was designed, built, and put into operation. The growth rate, surface morphology, compositional control, electrical properties of grown samples have been characterized.

(5) Thin film cells:

The aim of this effort was to modify amorphous silicon in ways that will lead to improved photovoltaic materials by alloying, doping, and altering the chemical bond in the solid state. An amorphous silicon deposition system using RF discharge was designed, built and used to obtain the first a-Si films. An EPR system, to be used for characterization of the samples, was installed.

(6) Silicon purification:

A low-temperature (< 900°C) electrochemical process for producing a high-purity, low-cost, solar-grade silicon has been developed. The novel use of a molten tin cathode avoids a number of problems encountered in previous work and yields material that is structurally and chemically compatible with silicon solar cell process technology. The material is n-type and 99.999% pure. The cost of this silicon should be \$3-5 per kg, well below the DOE cost goal of \$14 per kg.

(7) Silicon crystallization:

This research project is concerned with the investigation of melt growth processes with a potential for low-cost silicon sheet formation. The techniques pursued involve sheet support structures: one technique is contiguous capillary coating of Si on and in open-pore carbon sheets and the other technique is edge-supported pulling. Contiguous silicon coatings were applied by substrate dipping to several types of porous carbon substrates. For both perforated graphite sheets and reticulated vitreous carbon, grain sizes on the order of 0.5 mm could be achieved with thick Si coating of 0.5-1 mm.

(8) Thick-film technology:

The aim of this research effort is to define and study the potential applications of the screen-printing process to low-cost photovoltaic generation. It involved the examination of metal systems for contacting to photovoltaic devices as well as the analysis of the screen printing of active semiconductor materials.

(9) Surface and interface research:

This effort is composed of two major activities: (1) device and material analysis by different surface-sensitive spectroscopies, and (2) controlled

device and material fabrication. For analysis, Auger electron spectroscopy (AES), secondary ion mass spectroscopy (SIMS), and X-ray photoelectron spectroscopy (XPS) are used to examine semiconductor interfaces, Schottky barriers, and grain boundaries. The analysis described dealt with many photovoltaic materials such as Si, CdS, CdTe, InP, and GaAs. The material and device preparation activity has dealt with controlled fabrication methods of thin-film layers, such as molecular beam epitaxy (MBE). The report lists a large number of specific systems that were either prepared or analyzed by these techniques.

## TABLE OF CONTENTS

	<u>Page</u>
INTRODUCTION.....	I-1
SOLID-STATE THEORY	
1.0 Introduction and General Objectives.....	SS-1
2.0 Description of Progress.....	SS-2
2.1 Development of Reliable Pseudopotentials for Semiconductors..	SS-2
2.2 Development of Techniques for Solving the Electronic Structure Problem of Surfaces and Interfaces in the Pseudo- potential Framework.....	SS-3
2.3 Many-Body Corrections to the Electronic Structure Problem....	SS-5
2.4 Applications to the Electronic Structure of Surfaces: The Relaxed GaAs (110) Surface.....	SS-6
2.5 Application to the Electronic Structure of Interfaces: The Ge-GaAs Heterojunction.....	SS-6
2.6 Theoretical Systematization of Structural Properties of Binary Compounds.....	SS-9
2.7 Transition Metal Impurities in Semiconductors.....	SS-9
2.8 Systematics of Energy Levels of Point Defects in Semi- conductors.....	SS-12
2.9 Theory of Schottky-Barrier Formation.....	SS-12
2.10 Computer Modeling of the Electronic Structure of Defects at Heterojunctions.....	SS-14
2.11 Metal-Insulator Transition in Highly Doped Semiconductors....	SS-14
3.0 Future Directions.....	SS-15
4.0 References.....	SS-16
CASCADE SOLAR CELL	
1.0 Introduction.....	CS-1
2.0 Determination of the Composition of the Layer by Photoluminescence and Auger Spectroscopy.....	CS-3
2.1 Experimental Technique and Results.....	CS-3
2.2 Discussion of Results.....	CS-3
3.0 Electronic Structure of $Ga_{1-x}Al_xAs$ .....	CS-3
4.0 Design of a Tunnel Diode in $Ga_{1-x}Al_xAs$ .....	CS-6
4.1 Degeneracy in $Ga_{1-x}Al_xAs$ .....	CS-6
4.2 Tunnel Diodes.....	CS-8
5.0 High Doping Concentration in $Ga_{1-x}Al_xAs$ .....	CS-8
5.1 Selection of n- and p-Type Dopants.....	CS-8
5.2 n-Type Doping.....	CS-8
5.3 p-Type Doping.....	CS-9



## TABLE OF CONTENTS (Continued)

	<u>Page</u>
6.0 Future Developments.....	CS-9
6.1 Diffusion Experiments.....	CS-9
6.2 Test of the Tunnel Diodes.....	CS-9
6.3 Te Doping in GaAs.....	CS-11
7.0 References.....	CS-11
 PHOTOVOLTAIC PROPERTIES OF Si-V <sub>2</sub> O <sub>5</sub> AND GaAs-V <sub>2</sub> O <sub>5</sub> HETEROSTRUCTURES	
1.0 Introduction.....	PP-1
2.0 Results.....	PP-1
3.0 Discussion.....	PP-2
4.0 References.....	PP-2
 GROWTH OF GaAs AND RELATED COMPOUNDS BY METAL-ORGANIC CHEMICAL VAPOR DEPOSITION	
1.0 Introduction.....	GO-1
2.0 Apparatus Design and Construction.....	GO-2
3.0 Experimental Results.....	GO-5
3.1 Growth Rate.....	GO-5
3.2 Surface Morphology.....	GO-5
3.3 Compositional Control.....	GO-7
3.4 Electrical Properties.....	GO-7
3.5 Photoluminescence.....	GO-9
4.0 Conclusions and Future Directions.....	GO-9
5.0 References.....	GO-9
 THIN-FILM CELLS	
1.0 Introduction.....	TC-1
2.0 Progress.....	TC-1
2.1 Amorphous Silicon Deposition Apparatus.....	TC-1
2.2 Electron Spin Resonance System.....	TC-3
2.3 Results.....	TC-4
3.0 Future Directions.....	TC-4

## TABLE OF CONTENTS (Continued)

	<u>Page</u>
4.0 References.....	TC-4
SILICON PURIFICATION	
1.0 Introduction.....	SP-1
2.0 Background.....	SP-1
3.0 Experimental.....	SP-5
4.0 Results and Discussion.....	SP-7
4.1 Current-Voltage Measurements.....	SP-7
4.2 Electrochemical Current Efficiency.....	SP-7
4.3 Product Morphology.....	SP-10
5.0 Future Plans.....	SP-10
6.0 References.....	SP-12
SILICON CRYSTALLIZATION	
1.0 Introduction.....	SC-1
2.0 Status Summary.....	SC-1
2.1 Contiguous Capillary Coating.....	SC-1
2.1.1 Apparatus.....	SC-1
2.1.2 Substrates.....	SC-3
2.1.3 Perforated Bulk Graphite Sheets.....	SC-3
2.1.4 Reticulated Vitreous Carbon.....	SC-3
2.1.5 Cell Performance.....	SC-6
2.1.6 Summary and Discussion.....	SC-6
2.2 Edge-Supported Pulling.....	SC-6
3.0 Acknowledgments.....	SC-7
4.0 References.....	SC-7
THICK-FILM TECHNOLOGY	
1.0 Introduction.....	TF-1
2.0 Research and Results.....	TF-1
2.1 Metallization.....	TF-1
2.2 Active Layers.....	TF-4

TABLE OF CONTENTS (Concluded)

	<u>Page</u>
3.0 Future Directions.....	TF-5
4.0 Summary.....	TF-5
5.0 References.....	TF-5
 PHOTOVOLTAIC SURFACE AND INTERFACE RESEARCH	
1.0 Introduction.....	PS-1
2.0 Laboratory Capabilities.....	PS-2
2.1 Surface Analysis Capabilities.....	PS-2
2.2 Preparation Capabilities.....	PS-2
3.0 Research Summary.....	PS-3
4.0 References.....	PS-9

## LIST OF FIGURES

	<u>Page</u>
SS-1. Experimental (top) and Calculated (bottom) Valence Charge Density of Crystalline Silicon in the (110) Plane.....	SS-4
SS-2. Calculated (a) and Observed (b) Electronic States of the GaAs (110) Surface.....	SS-7
SS-3. Calculated Valence Electronic Charge Density of the GaAs-ZnSe (110) Interface.....	SS-8
SS-4.	
(a) The Rate of Convergence for the Bound $T_2$ Level in the Si Gap for the Vacancy in Si.....	SS-11
(b) Rate of Convergence for the Bound E Level in the Si Gap for Substitutional Fe in Si.....	SS-11
CS-1. Schematic Cascade Solar Cell.....	CS-2
CS-2. The 75 K Photoluminescence Peak.....	CS-5
CS-3. The Conduction Band Edge Values at 300 K.....	CS-7
CS-4. Typical Multilayered Structure Grown by LPE for Diffusion Experiments.....	CS-10
GO-1. Schematic of Metal-Organic Chemical Vapor Deposition (MOVCD) Apparatus.....	GO-3
GO-2. MOVCD Apparatus in the High-Efficiency Cell Laboratory.....	GO-4
GO-3. Top Row, Surface Morphology under Nomarski Interference Contrast, All 200X; Bottom Row, View of Cleaved Epitaxial Layer, (a) and (b) 1000X, (c) 500X.....	GO-6
GO-4. $Ga_{1-x}Al_xAs$ Epitaxial Layer Containing Polycrystalline Nugget, 100X.....	GO-8
TC-1. Deposition Apparatus for Preparing Thin Films of Amorphous Materials from Plasma Discharges.....	TC-2
SP-1.	
(a) Electrowinning of Silicon.....	SP-2

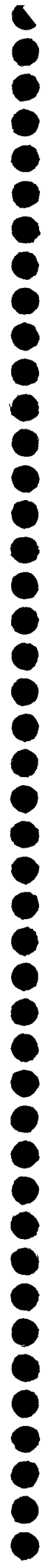
## LIST OF FIGURES (Concluded)

	<u>Page</u>
(b) Electrorefining of Silicon.....	SP-2
SP-2. Schematic of Electrolysis Cell.....	SP-6
SP-3. Cell Polarization Curve.....	SP-8
SP-4. Cell Current vs. Integrated Cell Current Q.....	SP-9
SP-5. Silicon Electrodeposited on (a) Molten Tin Cathode; (b) Solid (Graphite) Cathode.....	SP-11
SC-1. Hot-Zone Components for Contiguous Capillary Coating of Silicon on Porous Substrates.....	SC-2
SC-2. Reticulated Vitreous Carbon (left) and Perforated Graphite Sheet (right) Substrates.....	SC-4
SC-3. Grain Size Variation in a Thin Silicon Film Near a 1.5-mm- Diameter Perforation in the Graphite Substrate (72X).....	SC-4
SC-4. Typical Grain Configuration for a Thick Si Film on a Perforated Graphite Substrate (72X).....	SC-5
SC-5. Several Porosity Grades of Reticulated Vitreous Carbon Contigu- ously Coated with Silicon (24, 18, and 6 pores per cm).....	SC-5
SC-6. Schematic Diagram for Edge-Supported Pulling of Silicon Sheets...	SC-8
SC-7. Grain Structure of an Unseeded Silicon Sheet Grain by Edge- Supported Pulling.....	SC-8
TF-1. I-V Curve of Single-Crystal Silicon Solar Cell Before and After HF Etch.....	TF-3
PS-1. AES Spectrum of Polycrystalline GaAs Grown by LPE.....	PS-4
PS-2. AES Spectrum of Polycrystalline GaAs Grown by MBE, Taken under Same Conditions as Figure PS-1.....	PS-5
PS-3. Expanded AES Spectra Showing 800-1300 eV Range for LPE and MBE Samples in Figures PS-1 and PS-2.....	PS-6
PS-4. SIMS Spectra from LPE and MBE Polycrystalline GaAs Surfaces.....	PS-7
PS-5. AES Spectrum of LPE Polycrystalline GaAs Fractured to Expose Grain Boundary.....	PS-8

## LIST OF TABLES

	<u>Page</u>
SS-1. Comparison of the Band Structure of Crystalline Silicon as Obtained from an All-Electron (Core + Valence) Calculation and a Valence-Only Pseudopotential Calculation.....	SS-3
CS-1. $Ga_{1-x}Al_xAs$ -Te Doping: LPE Experiments at 780°C.....	CS-4
CS-2. Be Doping: LPE Experiments at 780°C.....	CS-4
CS-3. Mg Doping: LPE Experiments at 780°C.....	CS-4
SP-1. Standard Electrode Potentials at 1300 K.....	SP-4
SC-1. Solar Cell Data for a Contiguously Coated Silicon Sheet.....	SC-6
TF-1. Properties of Screen-Printed CdS.....	TF-5

**SERIO** 



## INTRODUCTION

The present report covers the research activities in the Photovoltaic Research Branch during the period 1 October 1979 to 31 March 1980. It includes reports on:

- Solid-State Theory;
- High-Efficiency Cells;
- Thin-Film Cells;
- Silicon Purification;
- Silicon Crystallization;
- Thick-Film Technology;
- Surface and Interface Analysis; and
- Growth of GaAs and Related Components by Metal-Organic Chemical Vapor Deposition.

This report concentrates on scientific and technical aspects alone. While it is strictly technical, the desire to keep it short and clear has necessarily led to a concise report, emphasizing predominantly the motivation behind each research project, its present status, the most significant results, and assessment of future research directions. The individual reports contain, therefore, reference to sources that describe each project in detail. The interested reader is encouraged to consult these publications (available on request) for more details. The list of references includes only papers submitted to or published in peer-reviewed journals.

While the report covers the six-month period from 1 October 1979 to 31 March 1980, it occasionally describes some previously accomplished results, as may be needed for a coherent and logical description of the present research efforts.

The reader will notice that for many of the presently reporting research groups, the period covered here has constituted a significant effort in establishing laboratories and techniques. Such an incubation period is not only necessary for a relatively young research group but is essential for developing the appropriate tools to conduct sophisticated research. Indeed, a considerable amount of the effort in this period was spent on making technical decisions as to significant research directions to be undertaken.

The individual sections describing each area are largely independent units and were numbered internally as such. Figures and tables are numbered sequentially in each section, prefixed by the initial letters of the first two words of the report title. This permits convenient access to individual sections for readers interested in selected subjects.



**SERI** 



## SOLID-STATE THEORY

Investigators: A. Zunger, U. Lindefelt,  
R. Allen (Sabbatical, 1 year),  
J. Dow (Sabbatical, 6 months)

## 1.0 INTRODUCTION AND GENERAL OBJECTIVES

While it is conceivable that the advancement of the photovoltaic (PV) approach as an economically viable, energy-producing method may be based on the refinement of existing techniques (i.e., presently selected semiconductors, geometries, and configurations), it may well be true that major improvements in effectiveness will result from new ideas (viz; new materials, a more fundamental understanding of limiting factors, etc.). The simplest possible approach to identifying new PV ideas is the empirical trial-and-error method involving experimentation with new materials, different doping, and varied configurations. An alternative method involves developing a theoretical understanding of those different factors, providing thereby the essential clues required for making rational guesses about new or improved methods to then be tested experimentally. This basic research effort comprises, by definition, a long-term project.

In addition to the search for new ideas and better understanding of limiting factors, the solid-state theory group is assisting in theoretical understanding of in-house experimental results, as well as organizing numerous inside seminars and discussion groups designed to cover the solid-state theory pertaining to photovoltaics.

The basic research thrust of the solid-state theory group in the Photovoltaic Research Branch is to develop the theoretical tools for studying the electronic structure of:

- bulk semiconductors;
- semiconductor surfaces;
- impurities and other defects in semiconductors; and
- interfaces between different semiconductors, as well as metal-semiconductor interfaces.

In contrast with the many existing phenomenological models that treat macroscopic effects in semiconductors (morphology of systems, current-voltage characteristics, etc.) from an engineering point of view, in the present approach quantum-mechanical models are used to treat these effects microscopically from a solid-state point of view.

Since the basic reason for avoiding such an approach to semiconductor devices in the past was the lack of suitable techniques, the work has first concentrated on developing fundamental methodologies. This has constituted the basis for a theoretical laboratory. Applications to problems of photovoltaic interest are then described.

## 2.0 DESCRIPTION OF PROGRESS

We describe here briefly the problems that have been treated, the rationale for choosing them, and the major results. A detailed description is available in the papers we have published or submitted to scientific journals [1-19].

The research effort is described below in logical order. It includes sections on:

- development of reliable pseudopotentials for semiconductors;
- development of techniques for solving the electronic structure problem of surfaces and interfaces in the pseudopotential framework;
- many-body corrections to the electronic structure problems;
- application to the electronic structure of surfaces--the relaxed GaAs (110) surface;
- application to the electronic structure of interfaces--the Ge-GaAs heterojunction;
- theoretical systematization of structural properties of binary compounds;
- transition-metal impurities in semiconductors;
- systematics of energy levels of defects in bulk semiconductors;
- theory of Schottky-barrier formation;
- computer modeling of the electronic structure of defects at heterojunctions; and
- metal-insulator transitions in highly doped semiconductors.

### 2.1 Development of Reliable Pseudopotentials for Semiconductors (A. Zunger)

In order to treat quantum mechanically complex solids, one would like to be able to discard the inner atomic electrons from the problem (e.g., 1s, 2s, and 2p for Si) and treat only a smaller number of the chemically and physically relevant valence electrons accurately (3s, 3p, 3d in Si). Although many empirical methods that do this have been suggested (e.g., the tight-binding method), we prefer to adopt a first-principles approach to the problem since the empirical data required in establishing an empirical theory are, in themselves, frequently questionable. A method allowing one to treat valence electrons only has been developed by the author [1]. This first-principles pseudopotential method has been tested on a number of semiconductors (Si, [2], Ge [2], and GaAs [3]) and achieved a reproduction of the electronic band structure as accurate as that obtained by theories that treat all (core + valence) electrons. For example, Table SS-1 gives the electronic band structure of silicon as calculated with the present pseudopotential approach (i.e., treating only 4 electrons per atom), compared with that obtained in an all-electron theory (14 electrons/atom). The average deviation is seen to be only 0.06 eV over an energy range of 20 eV of valence and conduction bands.

Table SS-1. COMPARISON OF THE BAND STRUCTURE OF CRYSTALLINE SILICON AS OBTAINED FROM AN ALL-ELECTRON (CORE + VALENCE) CALCULATION AND A VALENCE-ONLY PSEUDOPOTENTIAL CALCULATION\*

Level	All-Electron	Pseudo-potential	Level	All-Electron	Pseudo-potential
$\Gamma_{1,v}$	-12.02	-11.88	$X_{1,c}$	0.55	0.62
$\Gamma_{25,v}$	0.00	0.00	$X_{4,c}$	10.32	10.26
$\Gamma_{15,c}$	2.49	2.53	$L_{2',v}$	-9.64	-9.55
$\Gamma_{2',c}$	3.18	3.07	$L_{1,v}$	-7.06	-6.97
$\Gamma_{1,c}$	7.46	7.53	$L_{3,c}$	-1.16	-1.14
$\Gamma_{12,c}$	7.86	7.85	$L_{1,c}$	1.40	1.39
$X_{1,v}$	-7.84	-7.76	$L_{1,c}$	1.40	1.39
$X_{4,v}$	-2.82	-2.78			

\*Results in eV are obtained by a self-consistent Linear-Augmented-Plane-Wave method [4] using the Wigner exchange and correlation potential.

Clearly, however, the all-electron theories are not applicable in practice to complex systems such as a semiconductor surface, while the present pseudo-potential theory agrees well with the all-electron theories on simple systems (i.e., bulk semiconductors) and can be extended to complex systems by virtue of its simplicity.

An improved method [5] for obtaining first-principles pseudopotentials that reproduces not only the all-electron band structure but also yields remarkably accurate (~1%) electronic charge densities for semiconductors. Figure SS-1 shows the experimental and theoretical charge density of silicon. Again, the agreement is seen to be very good. (Recall that the only empirical input to the calculation is the atomic number of silicon!)

Hence, the first step of the effort provided an efficient and reliable method for describing the band structure and charge densities of semiconductors (i.e., one-electron properties) as accurate as that obtainable by state-of-the-art, all-electron methods. A simple analytical representations of those pseudopotentials for all atoms belonging to the first five rows in the periodic table has also been developed [6]. This will enable theoreticians to use our pseudopotentials conveniently for any element in the periodic table.

## 2.2 Development of Techniques for Solving the Electronic Structure Problem of Surfaces and Interfaces in the Pseudopotential Framework (A. Zunger)

Given the atomic pseudopotentials that reduce the problem of treating all the electrons in the system to a simpler problem involving only valence electrons, one needs to develop a technique for solving the Schrödinger wave equation within this pseudopotential formalism. The major problems here are:

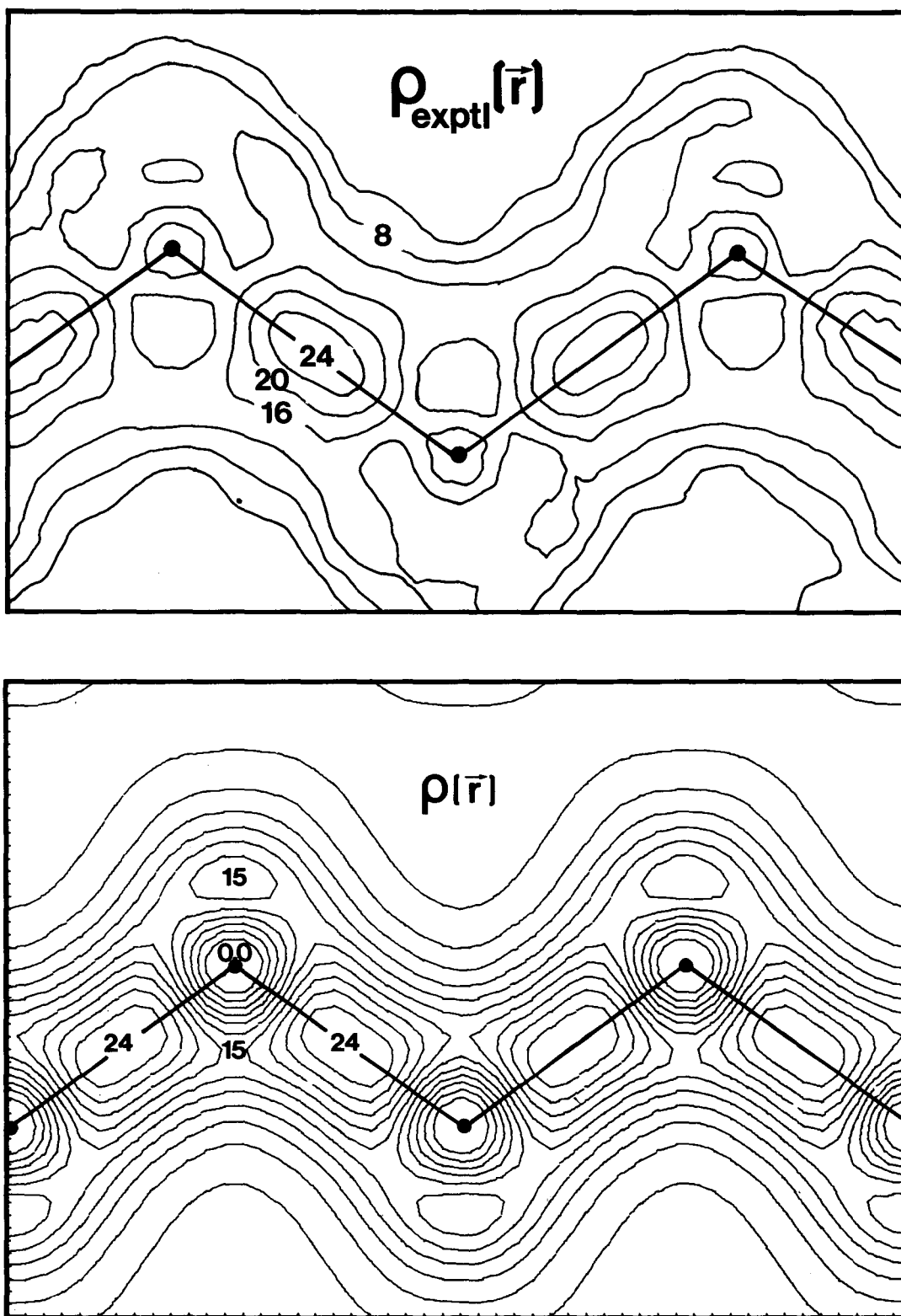


**Figure SS-1. Experimental (top) and Calculated (bottom) Valence Charge Density of Crystalline Silicon in the (110) Plane**  
(Units of electron/cell.)

- (1) As a surface or an interface lacks the translational periodicity of perfect bulk solids, the methods for solving the Schrödinger equation for the latter systems are inadequate for the former systems.
- (2) A reliable treatment of covalent and semipolar semiconductors requires a self-consistent solution for the Schrödinger equation (i.e., the total potential of the system depends on the wavefunctions being sought).
- (3) Accurate solutions require a variationally flexible basis set for expanding the wave functions.

Problem (1) is solved, following the previous studies, as well as those of others, by defining a "super cell" (rather than a primitive unit cell), which contains a contact between a semiconductor surface and vacuum or a contact between two different semiconductors. One repeats this super cell periodically over all space, thereby artificially restoring the translational symmetry. This allows the use of standard techniques for solving the Schrödinger equation. A different method for treating problem (1), the Green's function approach, is defined in Secs. 2.7 and 2.9. Problems (2) and (3) have been solved by developing a self-consistent mixed-basis (i.e., localized basis functions plus plane waves) representation. Using this method, a test on bulk Si was performed [7] which resulted in an accurate description of the band structure. Furthermore, using this novel method, the equilibrium lattice parameter of Si (calculated 5.44 Å, measured 5.43 Å) as well as the cohesive energy (within 1%) and the bulk modulus (within 5% from experiment) could be predicted from first principles [7] without resorting to any experimental input. This will allow the prediction of atomic rearrangements (relaxation) at surfaces and near defects in the future.

The second step of this effort, hence, allows one to solve reliably for the quantum mechanical electronic structure problem of semiconductors, predicting not only one-electron properties (first step), but also ground-state structural properties.

### 2.3 Many-Body Corrections to the Electronic Structure Problem [A. Zunger, J. Perdew (Tulane U., New Orleans)]

As stated in Secs. 2.2 and 2.3, this pseudopotential technique is able to predict one-electron properties (e.g., bandgaps) as accurately as the more complex all-electron theories do; the ground-state properties (e.g., cohesive energy, lattice constant) are in close agreement with experiment. Unfortunately, even the most sophisticated all-electron theories known today do not predict correctly the bandgap of semiconductors and insulators [5]. Consequently, any first-principles pseudopotential method suffers from the same limitations. This work sets out to develop simple many-body corrections to the presently known all-electron theories (viz., the Density Functional Formalism). This has been accomplished by the so-called "Self-Interaction Corrected Density Functional Approach" [8], a very significant and novel improvement over the current approaches to electronic structure of atoms, molecules, and solids. A more detailed explanation of this new theory is outside the scope of the present report. Details and various tests are presented, however, in Refs. [8] and [9]. This new approach has recently been extended to calculate atomic pseudopotentials, which include spin polarization

as well as the already mentioned many-body corrections [10]. This enables study of localized electronic states (e.g., deep defect levels), as well as the structure of magnetic impurities in semiconductors (viz., Sec. 2.7 in transition-metal impurities).

#### 2.4 Applications to the Electronic Structure of Surfaces: The Relaxed GaAs (110) Surface (A. Zunger)

As the first application to a complex semiconducting system, the methods developed in Secs. 2.1 and 2.3 have been used to study the electronic properties of the GaAs (110) surface [3]. This is the first calculation of any semiconductor surface using a first-principles, nonlocal pseudopotential approach. The main findings are the following.

- In contrast with previous theories as well as experiments done in the early 1970s, but in close agreement with modern angular resolved photo-emission studies, we find that the relaxed GaAs (110) surface shows no intrinsic gap surface states. Hence, the movement of atoms to different positions in the first surface layer eliminates all gap states. This result is significant to understanding Schottky barriers: in contrast to conventional thought, the Fermi energy pinning in GaAs cannot result from surface states (as suggested in 1947 by Bardeen).
- The wealth of predicted surface states (outside the gap) have been analyzed in detail, and compared with the recently available experimental results. Close agreement is found with experiments for the available data and predicts many new surface states that have not yet been observed experimentally [see Fig. SS-2, which gives a comparison of predicted and observed surface states of GaAs (110)].
- Important relations between relaxation of the atomic positions at the surface and the appearance of new surface states have been established. More details are given in Ref. [3].

#### 2.5 Application to the Electronic Structure of Interfaces: The Ge-GaAs Heterojunction (A. Zunger)

As a further application, these methods have been used to study the electronic properties of semiconductor interfaces. One is interested in predicting properties such as valence and conduction-band discontinuities, interface states, gap local density of states, charge densities due to the formation of new chemical bonds across the interface, etc. The Ge-GaAs (110) interface has been chosen for the first study. A large number of microscopic predictions on this interface have been deduced, including the energy and dispersion of interface resonant states, disruption of the electronic charge density at the interface, band discontinuities, etc. [11]. No detailed experimental information is available as yet to test the theoretical predictions. As a further application, we studied theoretically the GaAs-ZnSe (110) interface. Figure SS-3 illustrates a typical result, showing the electronic charge density across the interface, where a new Ga-Se bond has formed. Such results were instrumental in developing an educated intuition as to the chemistry taking place at semiconductor interfaces.

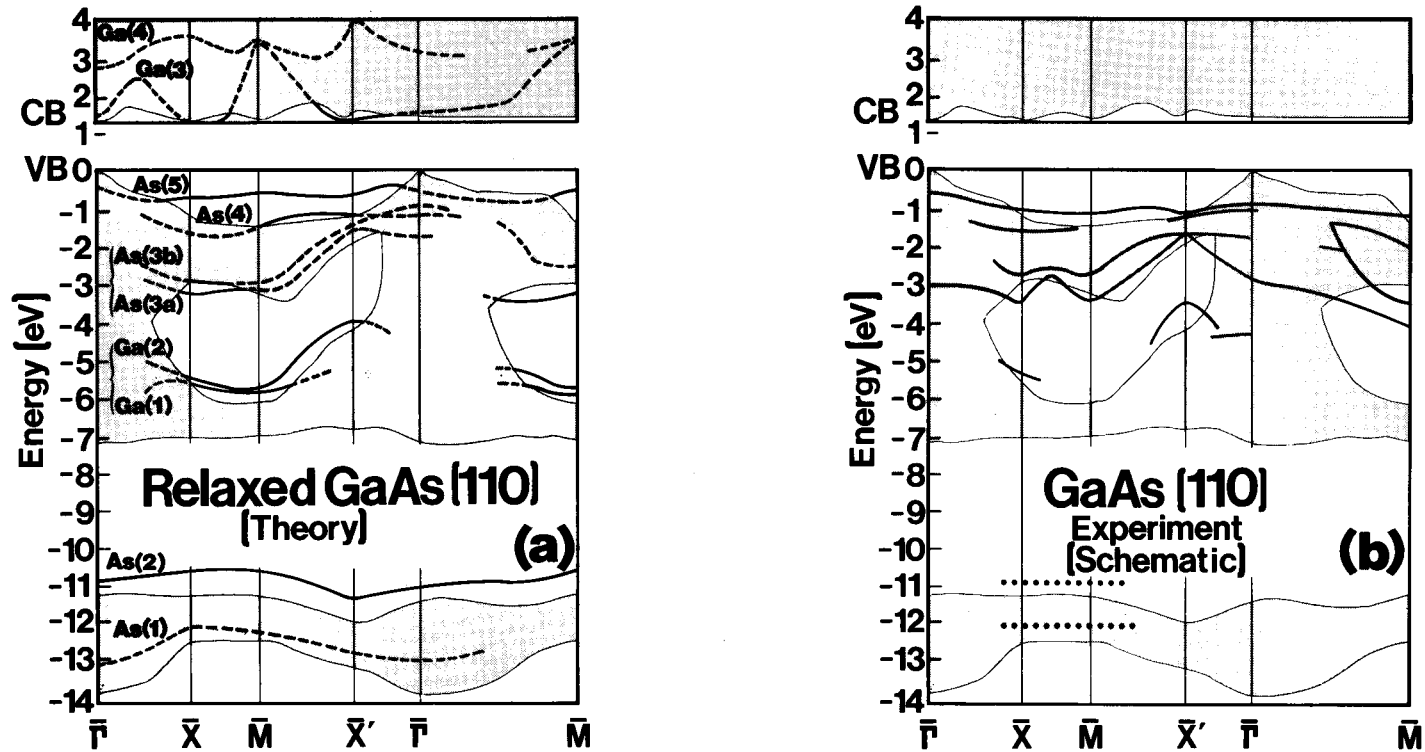


**Figure SS-2. Calculated (a) and Observed (b) Electronic States of the GaAs (110) Surface**  
 ( $\bar{V}\bar{B}$  and  $\bar{C}\bar{B}$  indicate valence and conduction band edges, respectively. Chemical symbols denote the character of each state. Dashed lines indicate weak resonance states. Dotted lines indicate experimentally uncertain states.)



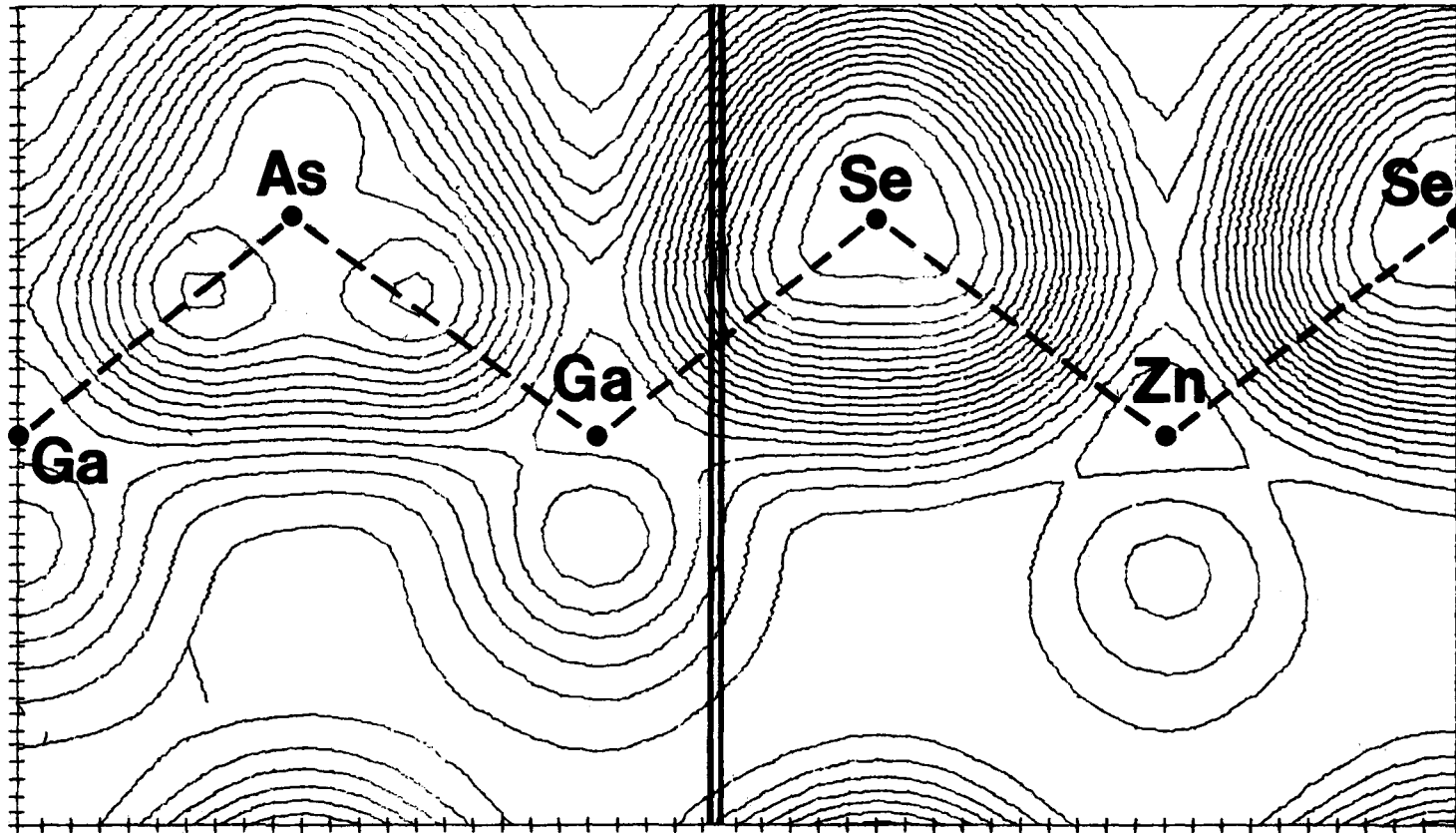


**Figure SS-3. Calculated Valence Electronic Charge Density of the GaAs-ZnSe (110) Interface**  
(The center vertical line denotes the interface position.)

## 2.6 Theoretical Systematization of Structural Properties of Binary Compounds (A. Zunger)

Thus far, the electronic properties of semiconductor systems has been discussed. The research effort described in the present section is concerned with structural properties.

The motivation for undertaking this research is the following: the number of binary AB-type compounds existing in nature is far larger than the number of AB-type compounds that have ever been tested for photovoltaic applications. As a matter of fact, of  $N$  different elements,  $N(N-1)/2$  possible AB-type compounds can be formed. Excluding compounds that are obviously uninteresting for solar energy conversion, this still leaves several hundred AB compounds, of which only about 10 to 20 have been studied for PV applications. Since an experimental straightforward trial-and-error attempt to select from a few hundred compounds those of potential PV interest is prohibitively time consuming, it would be desirable to have suitable theoretical guidelines. This, by itself, is an extremely ambitious effort, but of vital importance. As a first step in establishing such a comprehensive organization of binary compounds, an attempt will be made to develop a theory for predicting one of the most fundamental properties of solids--their crystal structure. The crystal structure of all known (565) binary compounds has been compiled from the experimental literature. Using the pseudopotential theory described in Sec. 2.1, one was able to develop a new electronegativity scale that, unlike the classical scales, is anisotropic (i.e., distinguishes between the affinity of s, p, and d electrons). With this scale, a simple theoretical criterion for predicting the stable crystal structure of AB compounds has been developed. This theory is remarkable in that, for the first time, it allowed the prediction of the stable structure of 565 compounds with an accuracy of 95% [12-14]. Such a theory ("the orbital radii method") may enable:

- the establishment of theoretical criteria for systematizing solids and, hence, be able to define certain subgroups with desired properties without having to resort to trial-and-error methods; and
- prediction of the stability and conformation of new chemical bonds formed at semiconductor interfaces and, hence, the possible patterns of relaxation at the interface.

This is a preliminary effort. In view of its remarkable success in predicting the structure of solids, it may be continued in the future to solve these problems.

## 2.7 Transition Metal Impurities in Semiconductors (U. Lindefelt; A. Zunger)

The efficiency of solar cells depends critically on the lifetime of electron-hole excitations. Deep impurities can either increase the lifetime of electron-hole excitations or decrease it, depending on the particular impurity and host material. To increase the efficiency of solar cells, therefore, it is important to obtain more insight into the physical mechanisms that determine the properties of deep impurities.

The current knowledge about the electronic structure of deep impurities in semiconductors is very limited, mainly due to the difficulties in setting up a general theory suitable for practical calculations. The main goal is therefore to:

- construct such a theory;
- apply it to various impurities, including transition metal impurities, in order to investigate trends through the periodic table; and
- incorporate the newly developed pseudopotential theory (Sec. 2.1) and many-body corrections (Sec. 2.3) to study these complicated localized defect states.

The major difficulties in treating theoretically localized defect states in semiconductors are:

- As the translational symmetry of the ideal crystal no longer exists, the conventional band structure methods are inadequate.
- Since there is a coexistence of localized electronic states (e.g., deep defect gap states) and itinerant electronic states (e.g., the host crystal bands) in similar energy domains, an adequate theory requires the incorporation of many-body correlation effects.
- Due to the introduction of a foreign atom into the semiconductor, electronic charge transfer with the host can take place. This requires a self-consistent solution of Schrödinger's equation.
- The existence of a defect normally induces lattice relaxation around the perturbed site. This effect of elastic strain is not known experimentally, but has to be included in any meaningful theory.

A novel first-principles theory to overcome these problems has been developed. Its salient features are:

- A Green's function method is used to efficiently circumvent the problem of lack of translational symmetry.
- A single-site basis set was developed to expand the impurity wavefunctions, leading to a flexible and efficient calculation of the energy level of the defect. This is illustrated in Fig. SS-4 (a and b), in which the energy of the gap state of a Si vacancy (Fig. SS-4a) or a substitutional Fe impurity in Si (Fig. SS-4b) is shown as a function of the number (N) of basis functions used. The rapid convergence is clearly seen.
- A new approach to obtaining self-consistency in the results (i.e., the potential depends on the wavefunctions which, in turn, are determined by the potential) was developed, based on a single-site Kubic harmonic expansion.
- The first-principles pseudopotentials (Sec. 2.1) and many-body correction scheme (Sec. 2.3) were implemented in the model.

For the first time, results have been obtained on the electronic structure of iron in silicon [15]. More applications to other transition metal impurities, including the study of the systematic variations in the gap states, are underway.

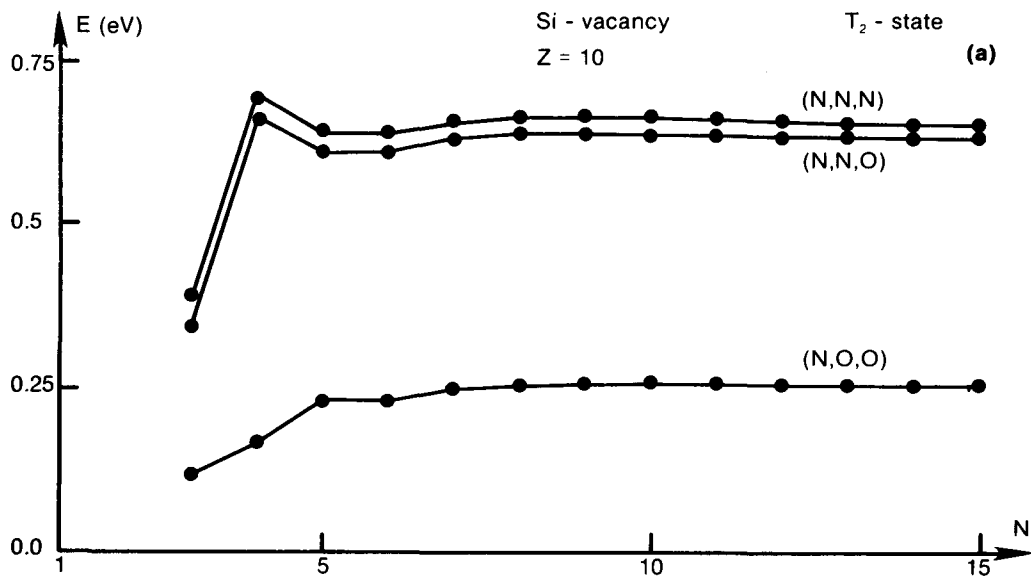


**Figure SS-4a. The Rate of Convergence for the Bound T<sub>2</sub> Level in the Si Gap for the Vacancy in Si** (The three integers in parentheses give the number of radial functions for the  $\ell = 1, 2,$  and  $3$  components, respectively.)

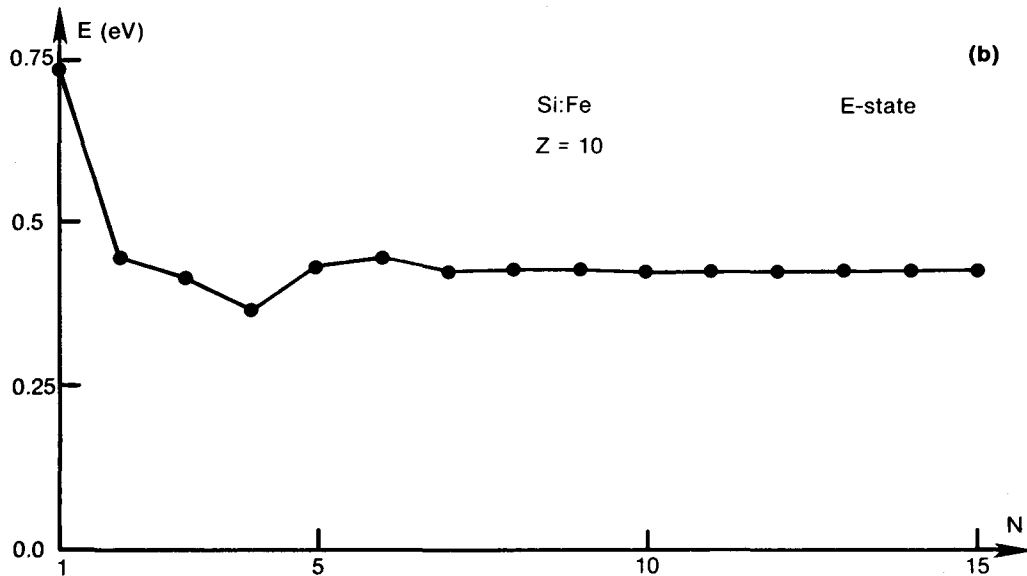


**Figure SS-4b. Rate of Convergence for the Bound E Level in the Si Gap for Substitutional Fe in Si**

## 2.8 Systematics of Energy Levels of Point Defects in Semiconductors (J. Dow, H. P. Hjalmarson)

While the approach described in the previous section is physically accurate and therefore complex, it was felt that at this stage one needs a complementary effort designed to give simple and approximate predictions for systematics of energy levels of various defects in semiconductors. This will then be used to identify potentially interesting systems to be treated by the more refined methods of Sec. 2.7.

Together with his student, J. Dow has developed a simplified theory of deep impurity levels lying within the forbidden bandgaps of semiconductors [16]. These impurity levels are known to be nonradiative recombination centers that limit device efficiencies. The theory has been applied to zinc blende semiconductors, and the first predictions of major chemical trends in deep-trap energies have been made. The physical nature of the deep impurity levels has been elucidated; somewhat surprisingly, the levels are not impurity-like states but host-like antibonding levels. This implies that it may be more difficult than previously anticipated to improve efficiencies of photovoltaic devices by altering the properties of these nonradiative centers. These ideas have been applied to amorphous Si, and estimates were made of the effects of H, F, Cl, and Na impurities. Again, all of these impurities are good candidates for improving amorphous Si device efficiencies, either because they move the vacancy deep trap out of the bandgap or because they replace the dangling bonds with a filled trap.

The theory is based on a non-self-consistent empirical tight-binding model, neglecting atomic rearrangement near the defect. This simple but general theory (1) provides a satisfactory definition of what constitutes a deep trap; (2) explains the major chemical trends in deep-trap energies, including their dependences on the host-energy bands and the impurities' atomic structures; (3) shows why data for deep-trap energies do not define a single smooth function of impurity atomic energy, even though clear trends with atomic energy are apparent; (4) explains why impurities whose atomic energies differ by ~10 eV produce trap energies differing by only a fraction of an electron volt; (5) predicts the derivatives of deep-trap energies with respect to host-alloy composition ( $x$ ) in alloys such as  $\text{GaAs}_{1-x}\text{P}_x$  and shows why these derivatives depend only weakly on the impurities; and (6) explains why in alloys the trap energies do not follow the nearby band edges as  $x$  varies but, instead, are often nearly linear functions of composition.

## 2.9 Theory of Schottky-Barrier Formation (R. Allen, A. Zunger)

This project is aimed at gaining a theoretical understanding of the factors affecting Schottky barriers at III-V semiconductors.

The old subject of Schottky-barrier formation has recently been placed in a new light as a result of remarkable set of experiments performed by Spicer and coworkers at Stanford [17]. The experiments demonstrate the following for the (110) surfaces of GaAs, GaSb, and InP:

- The Schottky-barrier height attains its final value after only a small fraction of a monolayer of metal atoms has been deposited on the semiconductor surface. Hence the physics and properties of Schottky barriers occurring in devices (i.e., a few-microns-thick metal layer) is already fully established when as little as a few-angstroms-thick metal overlayer is deposited.
- The barrier height is approximately the same for a wide range of metals and even for a nonmetal, such as oxygen, on a given semiconductor.

These remarkable findings, made possible by the advent of photoemission spectroscopy, basically indicate that the conventional models of Schottky barriers, from Bardeen and Schottky, are incomplete if not incorrect.

Since it is now known that GaAs does not have any intrinsic surface states that could cause this Schottky-barrier pinning (see Sec. 2.4), Spicer et al. have proposed a defect model in which the deposition of the metal induces defects in or near the semiconductor surface. The levels associated with these defects will then be identified with the positions of the surface Fermi energy (i.e., with the Schottky-barrier heights).

Still lacking is a fundamental understanding of what kinds of defects are involved and how defects can give rise to the particular levels observed experimentally. There is also the question of why the pinning behavior seems to disappear abruptly above a certain critical ionicity. This is an old question that now needs to be addressed in a new way.

Theoretical studies of defects at surfaces are more difficult than studies of either intrinsic surface properties or properties of defects in the bulk. Also, a large number of host and defect combinations should be examined, rather than studying a particular system in great detail. For these reasons, it is appropriate to use the tight-binding approximation, at least in the initial calculations. As is well known, the empirical tight-binding model is a useful tool for estimating chemical trends.

The calculations reported here [18] involve three steps:

- Calculate the bulk Green's function  $G_0$ .
- Use Dyson's equation,  $G = G_0 + G_0 V G$ , to calculate the surface Green's function  $G$ . Here  $V$  is a matrix that is associated with: (1) the cutting of bonds to form a pair of free surfaces (i.e., the cleaving of a perfect crystal) and (2) the relaxation of the anions and cations at each surface.
- Find the defect levels  $\epsilon$  by finding the zeroes of the Fredholm determinant,  $\det [1 - G(\epsilon) V_d]$ , where  $V_d$  is the perturbation due to the defect.

During the period being reported here, a computer program was developed to perform all of the preceding steps. The program evaluates the Fermi energy-pinning level due to various assumed defects at the surface of a semiconductor. The simplicity of this approximate method of calculation allows one to treat a large variety of defects and impurities (vacancy, antisite defects, impurities, such as Al, Ga, In, As, Sb, B, Zn, P, etc.), as well as different

geometries (impurities on the surface or a few layers below the surface). Preliminary results [18] obtained on the systematics of Schottky-barrier heights in GaAs with different metal covering tend to support the hypothesis of Spicer et al., that barrier heights are, in fact, determined by atomic defects rather than by equalizing the Fermi energy of the metal and the semiconductor.

#### 2.10 Computer Modeling of the Electronic Structure of Defects at Heterojunctions (R. Allen, J. Dow, H. P. Hjalmarson, A. Zunger)

The purpose of this project is to obtain some fundamental understanding of the nature of heterojunctions and defects near heterojunctions.

The calculations during the period covered by this report were for ideal (110) interfaces of semiconductors having the zinc blende structure (e.g., GaAs/AlAs and GaAs/ZnSe) and for point defects near such interfaces. The calculations were performed with a new computer program, GINTER, which was developed during the period covered by this report. They are the first calculations employing a new technique for theoretical studies of interfaces.

The following information about the electronic properties of heterojunctions is emerging from these calculations:

- the nature (and existence) of intrinsic interface states;
- the change in the electronic structure near the interface, as revealed in the local density of states;
- the change in defect levels near an interface (e.g., when does a deep level become shallow or vice versa);
- the wavefunctions associated with defect states and the change in the electronic structure around a defect when it is near an interface; and
- the effect of the band-edge discontinuity on both interface states and defect levels.

For example, we found that defect levels on the GaAs side are only slightly perturbed from their bulk values at the GaAs/AlAs interface, but they are dramatically altered at the GaAs/ZnSe interface. At this strong interface, the  $A_1$  (or s-like) level undergoes a large shift from its bulk value and the three  $T_2$  (or p-like) levels, which are degenerate in the bulk, become highly nondegenerate at the interface.

#### 2.11 Metal-Insulator Transition in Highly Doped Semiconductors (H. P. D. Lanyon, A. Zunger)

The understanding of the electrical and transport properties of highly doped semiconductors has traditionally been of great interest for many device applications. The basic phenomenon encountered is that at low doping of Si, Ge, or GaAs with impurities, such as B, P, As, Sb, Se, etc., one observes the formation of shallow levels (e.g., within 5 meV to 60 meV from the band edges), leading to a characteristic, temperature-activated conductivity and free-

carrier mobility. At a high enough doping level, on the other hand, an unactivated free-carrier formation is observed, much like metallic systems. The critical free-carrier density,  $n_c$ , at which such an insulator-to-metal behavior occurs has been the subject of many experimental and theoretical studies. Many models have been previously suggested to explain the regularities in  $n_c$  in different host semiconductors and for various dopants. These include effects such as disorder, band tailing, impurity-band broadening, Coulomb screening, many-body effects, etc.

The object of the present study was to offer a simple model that explains: (1) the temperature dependence of free carriers at densities below  $n_c$ , in different semiconductors; and (2) the magnitude of  $n_c$  at which the transition occurs.

The model concentrates on the reduction in impurity activation energy  $E_i$  due to the Coulomb screening of positive donor states by free carriers. This model provides the actual activation energy  $E_i(T)$  in terms of the activation energy at dilution  $E_i^0$  and the reduction energy  $\Delta E(T,n)$ , as  $E_i(T) = E_i^0 - \Delta E(T,n)$ .

The major findings are:

- The model  $E_i(T) = E_i^0 - \Delta E(T,n)$  predicts the correct temperature dependence of free-carrier density  $n(T)$  in a simple but accurate way. This can be used directly in device modeling programs.
- The critical density  $n_c$  at which the activation energy vanishes [ $E_i(T) = 0$ ], or at which the carrier density becomes temperature independent:  $dn(T)/dt = 0$ , is sought. It is found that the  $n_c$  values are about a factor of 3 smaller than the observed values, indicating that a band broadening of about 14 meV (for P in Si) is probably taking place near the transition.
- Applied to study valence-to-conduction bandgap narrowing as a function of doping, the same model predicts remarkably accurate results. It is being used presently as a predictive model in device modeling programs with very good results.
- This model can be used reliably to deduce the activation energy from Hall effect data at infinite dilution  $E_i^0$ . We have applied it to previously published data and deduced corrected values for  $E_i^0$ .
- Recently the model has been applied successfully to analyze the GaAs laser data available in the literature.

The model and detailed applications are being prepared for publication in Physical Review [19].

### 3.0 FUTURE DIRECTIONS

New theoretical methods have been established to treat the problems outlined in the introduction. No further major investment in this direction is therefore foreseen. In the presently reported period, the efforts have been



broadened, both on development of new techniques and on applying them to a diverse range of problems with the intention of: (1) identifying promising directions and (2) establishing the first theory on a number of photovoltaics-related phenomena. A focusing of the efforts in the future on a number of selected problems will be undertaken.

The major planned objectives are:

- The study of transition metal defects and other interesting deep defects in semiconductors will be expanded (using the methods described in Secs. 2.7 and 2.9) in an attempt to gain detailed information on the electronic and transport properties, as well as knowledge of systematic trends in these systems.
- The presently developed theoretical methods, as well as the new approach being developed by P. Bendt and A. Zunger to study atomic relaxation effects will be implemented. The implementation may include hydrogen and other impurities in amorphous silicon, as well as surface relaxation effects in semiconductors and their effects on Schottky barriers.

In general, the efforts will be concentrated on problems that are unique and unusually interesting and important, so as to compete effectively with the much larger solid state theory groups in this country. Besides these planned activities, it is likely that work on unexpected theoretical problems that may arise in the course of the experimental work in the Photovoltaics Research Branch will continue.

The reader will notice that the projects defined in Sec. 2.0 are extremely ambitious, involving not only complex systems (which were not treated previously by accurate quantum mechanical methods) but also new methods and ideas. Thus, success is not guaranteed. The benefit that may accrue from the unorthodox; innovative approaches is potentially great.

#### 4.0 REFERENCES

1. Zunger, A.; Cohen, M. L. "A First-Principles Nonlocal Pseudopotential Approach to the Density-Functional Formalism. I. Development and Applications to Atoms." Phys. Rev. B. Vol. 18: p. 5449 (1978).
2. Zunger, A.; Cohen, M. L. "A First-Principles Nonlocal Pseudopotential Approach in the Density-Functional Formalism. II. Applications to Electronic and Structural Properties of Solids." Phys. Rev. B. Vol. 20: p. 4082 (1979).
3. Zunger, A. "A Nonlocal Pseudopotential Calculation of the Relaxed GaAs (110) Surface." Phys. Rev. B. (in press) (1980).
4. Hamann, D. R.; Zunger, A. (to be published).
5. Zunger, A. "Contemporary Pseudopotentials: Simple Reliability Criteria." J. Vac. Sci. Technol. Vol. 16: p. 1337 (1979).

6. Lam, P.; Cohen, M. L.; Zunger, A. "Analytical Representation for First-Principles Pseudopotentials." Phys. Rev. B. (in press) (1980).
7. Zunger, A. "Ground State Properties of Crystalline Si in a Density Functional Pseudopotential Approach." Phys. Rev. B. (in press) (1980).
8. Zunger, A.; Perdew, J. P.; Oliver, G. L. "A Self-Interaction Corrected Approach to Many-Electron Systems: Beyond the Local Spin Density Approximation." Solid-State Commun. (34, 933) (1980).
9. Perdew, J. P., Zunger, A.; "Self-Interaction Corrections To Density Functional Approximations For Many-Electron Systems." In preparation for Phys. Rev. B.
10. Zunger, A. "Spin-Dependent Correlated Atomic Pseudopotentials." Phys. Rev. B. (in press) (1980).
11. Zunger, A. "Electronic Structure Calculation for the Ge-GaAs (110) Interface." (to be published).
12. Zunger, A. "Structural Stability of 495 Binary Compounds." Phys. Rev. Lett. Vol. 44: p. 582 (1980).
13. Zunger, A. "A Pseudopotential Viewpoint on the Electronic and Structural Properties of Crystals," to appear in Structure and Bondings in Crystals, M. O'Keefe and A. Navrotsky, editors. Academic Press, N.Y. (1980).
14. Zunger, A. "Pseudopotential Orbital Radii and the Structure of Crystals." Phys. Rev. B. (In Press).
15. Lindefelt, U.; Zunger, A. "Electronic Structure of Transition Metal Impurities in Semiconductors." (In preparation).
16. Hjalmarson, H. P.; Vogl, P.; Wolford, D. J.; Dow, J. D. "Theory of Substitutional Deep Traps in Covalent Semiconductors." Phys. Rev. Lett. Vol. 44: p. 810 (1980).
17. Spicer, W. E.; Lindau, I.; Skeath, P.; Su, C. T.; Chye, P. Phys. Rev. Lett. Vol. 44: p. 420 (1980).
18. Allen, R.; Zunger, A. "Theory of Schottky Barriers on III-V Semiconductors." In preparation for Phys. Rev. B. Also see Bull. Am. Phys. Soc. Vol. 75: p. 194 (1980).
19. Lanyon, H. P. D.; Zunger, A. "Metal-Insulator Transition and Bandgap Narrowing in Heavily Doped Semiconductors--Simple Predictions of the Coulomb Screening Model." In preparation for Phys. Rev. B.

**SERI** 



## CASCADE SOLAR CELL

Investigators: Pierre Gibart (Sabbatical),  
Russell E. Hayes (Consultant),  
Michael Kowalchik and Sigurd Wagner

## 1.0 INTRODUCTION

The intrinsic efficiency limits of single-crystal solar cells, i.e., 21% for Si, 25% for GaAs at AM1, have almost been reached. These limits arise from the finite lifetimes of minority carriers and from the bandgap of the semiconductor. Improvement of the conversion efficiency can be achieved by concentration and spectral splitting.

In a cascade solar cell, two cells with different bandgaps are connected in series (Fig. CS-1). Each cell responds to a different range of photon energy. Computer modeling gives the optimum bandgaps to obtain the highest efficiency. For two cells, the calculated optimum gaps are 1.6 eV and 0.95 eV respectively [1-5].

However, the design of a cascade solar cell is strictly limited by severe constraints:

- The different cells are stacked together on the same substrate by epitaxial growth; all different parts of the monolithic structure should be lattice-matched.
- The elementary cells are connected together by a tunnel junction. To avoid generation of a photovoltage across the tunnel diode, its bandgap must be higher than that of the top cell. The tunnel junction must be as thin as possible to reduce the voltage drop across the junction.
- Most important, the tunnel diode must be stable at the temperature of the epitaxial growth of the top layer. In an operating cascade solar cell, typically 1000 suns, the tunnel junction must be stable in time under a peak current density of 30-40 A/cm<sup>2</sup>.
- In a two-cell monolithic structure (Fig. CS-1), the terminal current passes through each of the three junctions. For maximum efficiency, the short circuit current in the top and bottom cells must be the same.

Epitaxial Growth of Ga<sub>1-x</sub>Al<sub>x</sub>As Layers by Liquid Phase Epitaxy (LPE)

Epitaxial layers of Ga<sub>1-x</sub>Al<sub>x</sub>As were grown on 100% GaAs substrates by LPE using the sliding boat method. Growth occurs at 780°C or 850°C. The composition of the melt was determined from the thermodynamic data of the ternary Ga-Al-As [8].

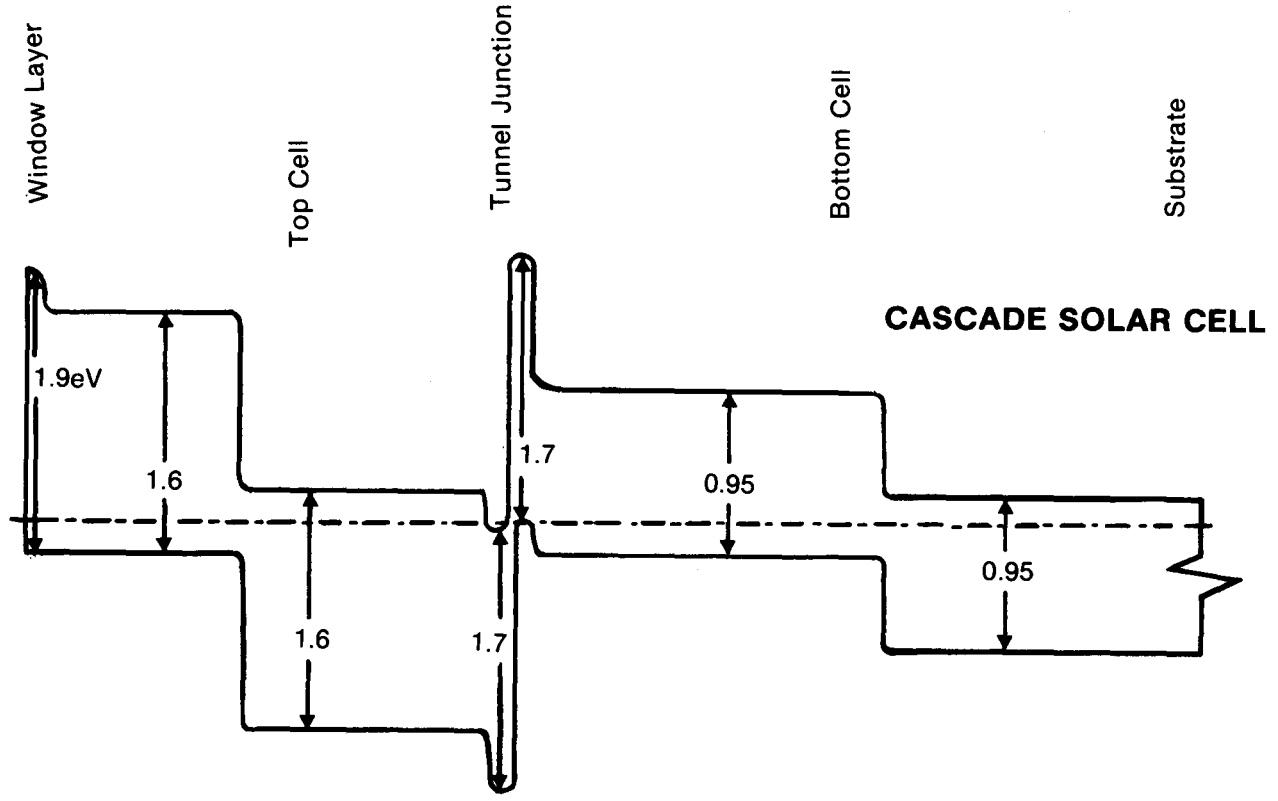


**Figure CS-1. Schematic Cascade Solar Cell.** (The two cells are connected by  $p^+/n^+$  tunnel diode.)

## 2.0 DETERMINATION OF THE COMPOSITION OF THE LAYER BY PHOTOLUMINESCENCE AND AUGER SPECTROSCOPY

The purpose of this work was to determine the energy bandgap, atomic composition, and a qualitative measurement of the overall quality of the  $\text{Ga}_{1-x}\text{Al}_x\text{As}$  being grown by LPE for high-efficiency solar cell applications. The luminescence results have been correlated with Auger spectroscopy composition measurements and recent results appearing in the literature.

### 2.1 Experimental Technique and Results

Luminescence results were obtained with a standard photoluminescence system consisting of a filtered mercury arc lamp source, a  $0.65\text{-}\mu$  monochromator, and an S-1 cathode photomultiplier using a lock-in amplifier detection system. The sample was cooled to 75 K.

A series of measurements was carried out for LPE samples grown from melts having the compositions shown in Table CS-1. These layers, which were not intentionally doped, had free carrier concentrations of about  $10^{16}\text{ cm}^{-3}$ . Figure CS-2 shows a plot of the photoluminescence peak energy as a function of the atomic composition parameter  $x$ . The value of  $x$  was determined by Auger spectroscopy in the SERI surface analysis laboratory (P. Ireland). Also shown in Fig. CS-2 are the locations of the several conduction band minima, as determined from the empirical expressions given by Lee et al. [6].

### 2.2 Discussion of Results

The photoluminescence results described here are typical for LPE material of good quality; that is, the luminescence indicates that there is not a high density of nonradiative recombination centers or deep energy levels in the epitaxially grown material.

The luminescence peak as a function of Al content shown in Fig. CS-2 indicates that the bandgap and composition measurements are in excellent agreement with those calculated from empirically determined parameters given by Lee et al. [6]. There is a slight disagreement in the literature about the exact placement of the  $\Gamma$ -minimum [7,8]. However, the excellent agreement shown in Fig. CS-2 indicates that our bandgap-composition measurements correlate well with results of others.

Calibration of  $\text{Ga}_{1-x}\text{Al}_x\text{As}$  for compositions with indirect bandgap was made by Auger spectroscopy only. The agreement with the thermodynamic data of the ternary Ga-Al-As is good.

## 3.0 ELECTRONIC STRUCTURE OF $\text{Ga}_{1-x}\text{Al}_x\text{As}$

Although not much is known about the electronic structure of  $\text{Ga}_{1-x}\text{Al}_x\text{As}$ , knowledge of the different bands and of the impurity levels in  $\text{Ga}_{1-x}\text{Al}_x\text{As}$  is of fundamental importance for the definition of tunnel diodes. Very recent papers have provided new information on the electronic structure of  $\text{Ga}_{1-x}\text{Al}_x\text{As}$  [7,9].

Table CS-1:  $\text{Ga}_{1-x}\text{Al}_x\text{As}$ -Te DOPING: LPE EXPERIMENTS AT 780°C

Te in melt (atomic concentration)	GaAs (electrons/cm <sup>3</sup> )	$\text{Ga}_{0.9}\text{Al}_{0.1}\text{As}$ (electrons/cm <sup>3</sup> )	$\text{Ga}_{0.8}\text{Al}_{0.2}\text{As}$ (electrons/cm <sup>3</sup> )
$10^{-4}$	$4-5 \times 10^{18}$ $\mu = 1450^a$	$3 \times 10^{18}$ $\mu \approx 950$	$4 \times 10^{18}$ $\mu = 720$
$10^{-3}$	$10^{19}$ $\mu = 1400$	$5 \times 10^{18}$ $\mu = 920$	$10^{19}$ $\mu = 690$
$10^{-2}$	$1.3 \times 10^{19}$ $\mu = 1350$	$1.2 \times 10^{19}$ $\mu = 850$	$1.7 \times 10^{19}$ $\mu = 870$

<sup>a</sup> $\mu$  is expressed in cm<sup>2</sup>/V s.

Table CS-2. Be DOPING: LPE EXPERIMENTS AT 780°C

Be in melt (atomic concentration)	GaAs (electrons/cm <sup>3</sup> )	$\text{Ga}_{0.9}\text{Al}_{0.1}\text{As}$ (electrons/cm <sup>3</sup> )	$\text{Ga}_{0.8}\text{Al}_{0.2}\text{As}$ (electrons/cm <sup>3</sup> )
$4 \times 10^{-4}$		$p = 4 \times 10^{18}$ $\mu = 40^a$	$p = 2 \times 10^{19}$ $\mu = 67$
$8 \times 10^{-4}$	$p = 4.3 \times 10^{19}$ $\mu = 75$	$p = 4 \times 10^{19}$ $\mu = 67$	$p = 2.5 \times 10^{19}$ $\mu = 77$
$1.1 \times 10^{-3}$		$p = 5-6 \times 10^{19}$ $\mu = 77$	$p = 10^{20}$ $\mu = 35$

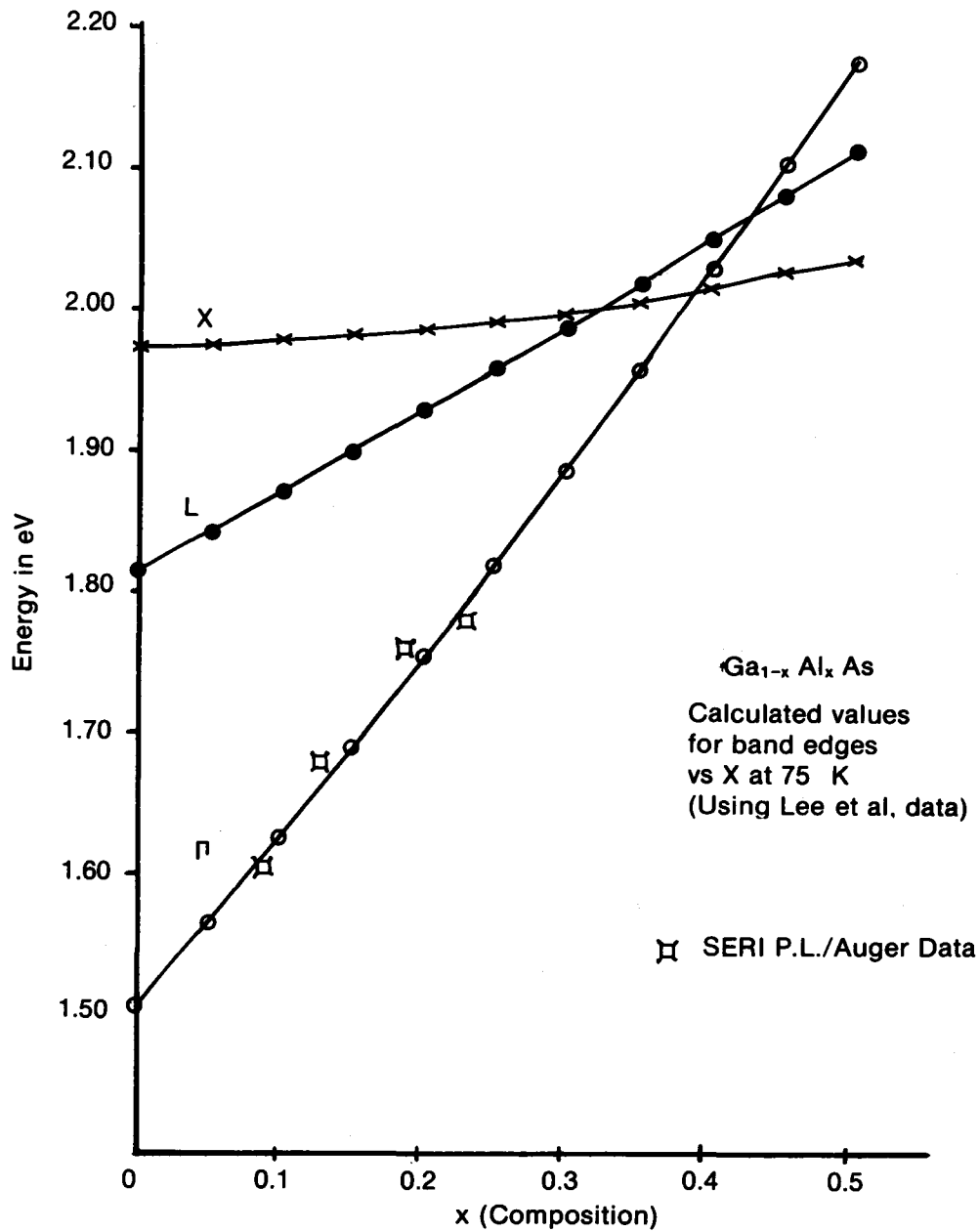
<sup>a</sup> $\mu$  is expressed in cm<sup>2</sup>/V s.

Table CS-3. Mg DOPING: LPE EXPERIMENTS AT 780°C<sup>a</sup>

Mg in melt (atomic concentration)	GaAs (electrons/cm <sup>3</sup> )	$\text{Ga}_{0.9}\text{Al}_{0.1}\text{As}$ (electrons/cm <sup>3</sup> )	$\text{Ga}_{0.8}\text{Al}_{0.2}\text{As}$ (electrons/cm <sup>3</sup> )
$10^{-3}$	$p = 2.8 \times 10^{18}$ $\mu = 1450^b$	$p = 4 \times 10^{18}$ $\mu = 56$	$p = 2.3 \times 10^{18}$ $\mu = 52$
$5 \times 10^{-3}$		$p = 4 \times 10^{18}$ $\mu = 100$	$p = 2.8 \times 10^{18}$ $\mu = 116$
$8 \times 10^{-3}$		$p = 7 \times 10^{18}$ $\mu = 85$	

<sup>a</sup>Other experiments at 850°C or with more Mg in the melt are not reported. Results with  $10^{-3}$  Mg in melt will be checked.

<sup>b</sup> $\mu$  is expressed in cm<sup>2</sup>/V s.



**Figure CS-2. The 75 K Photoluminescence Peak.** (Composition data obtained on SERI LPE samples and the conduction band edge values calculated from parameters given by Lee et al. [6]. x denotes atomic fraction of Al.)



Figure CS-3 gives the relative position of the  $\Gamma$ , X, and L minima in  $\text{Ga}_{1-x}\text{Al}_x\text{As}$  as a function of  $x$ . The crossover occurs at  $x = 0.37$ . The donor levels attached to the different conduction band minima are shown by a dashed line. The donor levels attached to  $\Gamma$ , L, and X bands have different ionization energies. For Sn,  $E_{d\Gamma} = 5$  meV,  $E_{dL} = 140$  meV, and  $E_{dX} = 101$  meV [9]. ( $E_{d\Gamma}$ ,  $E_{dL}$ , and  $E_{dX}$  are positions of the donor level.) For Te, the values are slightly different. Our experimental results agree with published data [10].

From a practical point of view, degenerate n-type sample can be obtained only for  $n < 0.23$ .

#### 4.0 DESIGN OF A TUNNEL DIODE IN $\text{Ga}_{1-x}\text{Al}_x\text{As}$

##### 4.1 Degeneracy in $\text{Ga}_{1-x}\text{Al}_x\text{As}$

To obtain a tunnel diode, the semiconductor must be heavily doped to create degeneracy in the valence and conduction bands on the two sides of the function. Impurity-assisted tunneling has been reported for  $p = 1.3 \times 10^{19} \text{ cm}^{-3}$  in GaAs [11].

Degeneracy concentration was calculated using the most recent reliable values of the effective masses in  $\text{Ga}_{1-x}\text{Al}_x\text{As}$ [9]. Degeneracy occurs when the Fermi level merges into the conduction (or valence) band for electrons:

$$m_{\Gamma}^* = (0.067 \text{ to } 0.083 \text{ n}) m_0$$

$$m_X^* = (0.85 - 0.07 \text{ n}) m_0$$

$$m_{1h}^* = 0.12 m_0$$

$$m_{hh}^* = 0.62 m_0$$

$$n = \frac{2}{\sqrt{\pi}} N_c F_{1/2} \frac{E_f - E_c}{kT} \quad \text{with } E_f - E_c = 0$$

$$p = \frac{2}{\sqrt{\pi}} N_v F_{1/2} \frac{E_v - E_f}{kT} \quad \text{with } E_v - E_f = 0$$

where

$F_{1/2}$  = the Fermi-Dirac integral; and

$$N_c = 2 \left( \frac{2\pi m^* kT}{h^2} \right)^{3/2}$$

$$N_v = \left( \frac{2\pi M_{dh} kT}{h^2} \right)^{3/2},$$

where  $M_{dh} = (M_{1h}^{*3/2} + M_{hh}^{*3/2})^{2/3}$ .

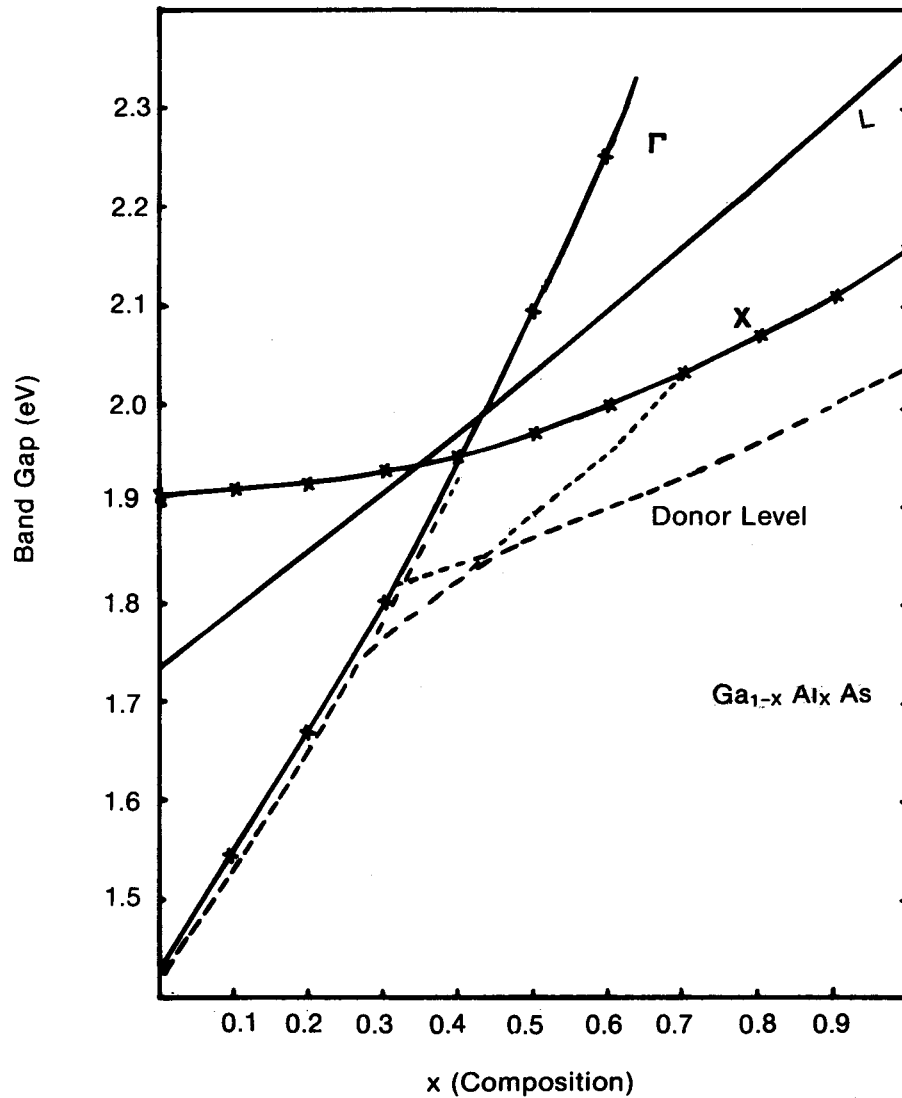


**Figure CS-3. The Conduction Band Edge Values at 300 K**  
(From Lee et al. [6]; donor levels attached to the different minima are shown by a dashed line. x denotes atomic fraction of Al.)



At 300 K  $n = 3 \times 10^{17} \text{ cm}^{-3}$  for GaAs  
 $n = 4 \times 10^{17} \text{ cm}^{-3}$  for  $\text{Ga}_{0.8}\text{Al}_{0.2}\text{As}$   
 $n = 1.2 \times 10^{19} \text{ cm}^{-3}$  for  $\text{Ga}_{0.5}\text{Al}_{0.5}\text{As}$   
 $p = 9 \times 10^{18} \text{ cm}^{-3}$  for all compositions.

#### 4.2 Tunnel Diodes

The tunnel diode connecting two solar cells is realized by making a  $p^+/n^+$  junction; both sides of the junction must be doped to the degeneracy. Furthermore, the junction should be very abrupt. Tunneling mechanisms are reviewed in basic papers [11,12,13]. In a typical cascade solar cell, the tunnel diode is working under forward bias at a current density lower than the peak current  $I_p$ . This peak current is proportional to  $1/w \exp(-k_1 w)$ , where  $w$  is the junction depth. This means that  $w$  must be as small as possible. (According to Ref. 1,  $w$  is about equal to 100 Å). Tunnel diodes were grown by LPE [14], CVD-MO [15], and MBE [16,17]. The MBE method, with the capability of growing very abrupt heterojunctions, gives the best results. To avoid excessive diffusion of the doping elements, the growth process must occur at the lowest possible temperature. In the present work, tunnel diodes were grown by LPE in order to study the degradation process of these diodes with permanent working conditions of 30-40 A/cm<sup>2</sup>.

#### 5.0 HIGH DOPING CONCENTRATION IN $\text{Ga}_{1-x}\text{Al}_x\text{As}$

##### 5.1 Selection of n- and p-Type Dopants

The dopants were chosen to obtain the highest possible doping level (up to degeneracy), the lowest diffusion coefficient (to avoid degradation of the tunnel diode during the epitaxial growth of the bottom cell), and to be able to grow a very abrupt junction without interdiffusion of n and p dopants.

##### 5.2 n-Type Doping

The diffusion coefficient of Te in GaAs is  $10^{-13} \text{ cm}^2/\text{s}$  at 1000°C (other n-dopants: S;  $10^{-12}$ ; Se;  $10^{-13}$ ; Sn;  $7 \times 10^{-10}$ ). The highest doping levels were reported for Te.

Data for Te doping of  $\text{Ga}_{1-x}\text{Al}_x\text{As}$  are reported in Table CS-1. Results for pure GaAs ( $n$ ,  $\mu$ ) are consistent with published data [18]. These results show that degeneracy is easily reached by using Te for n-type doping. For  $x \leq 0.2$ , Te becomes a deep donor ( $E_d = 0.187 \text{ eV}$ ).

### 5.3 p-Type Doping

The p-type dopants were chosen with lower diffusion coefficients. Be and Mg were reported to have low diffusion coefficients.

$$D(\text{Zn}) = 3.2 \times 10^{-8} \text{ cm}^2/\text{s at } 900^\circ\text{C}$$

$$D(\text{Be}) = 3.7 \times 10^{-10} \text{ cm}^2/\text{s at } 900^\circ\text{C [19]}$$

$$D(\text{Be}) = 1 \times 10^{-13} \text{ cm}^2/\text{s at } 900^\circ\text{C [20]}$$

$$D(\text{Mg}) = 1.3 \times 10^{-12} \text{ cm}^2/\text{s at } 900^\circ\text{C}$$

Two significantly different values were reported for the diffusion coefficient of Be in GaAs [19,20].

Experiments were carried out (Sec. 5.4) to reevaluate the diffusion coefficient of Mg and Be in  $\text{Ga}_{1-x}\text{Al}_x\text{As}$  ( $x = 0, 0.1, 0.2$ ). Mg and Be p-type samples were grown by LPE at  $780^\circ\text{C}$  or  $850^\circ\text{C}$ . The results are summarized in Tables CS-2 and CS-3. From these results, it appears that Mg can hardly lead to p-type degenerated samples. Furthermore, Mg-doped samples show inclusion of  $\text{Mg}_3\text{As}_2$  at the surface of the epilayers. Further epilayers cannot be grown without introducing high defect densities.

In order to recheck the diffusion coefficients of Mg and Be in  $\text{Ga}_{1-x}\text{Al}_x\text{As}$ , the structure shown in Fig. CS-4 was grown by LPE. A highly doped Be (or Mg) layer is intercalated between two undoped layers. The Be concentration is determined by secondary-ion mass spectroscopy (SIMS). When the three-layer structure is annealed in a quartz ampoule under  $\text{As}_2$  atmosphere at  $850^\circ\text{--}900^\circ\text{C}$  for 1/2 hour and the Be concentration profile is measured afterwards, D is deduced from this profile.

## 6.0 FUTURE DEVELOPMENTS

### 6.1 Diffusion Experiments

Further experiments are planned (SIMS, electrical profiling) to obtain reliable data for the diffusion coefficient of Be in GaAs,  $\text{Ga}_{0.9}\text{Al}_{0.1}\text{As}$ , and  $\text{Ga}_{0.8}\text{Al}_{0.2}\text{As}$ .

### 6.2 Test of the Tunnel Diodes

The first  $p^+/n^+$  diodes were grown by LPE using the sliding method on a Te-doped substrate. Typical thickness of the layers was  $1 \mu\text{m}$ . Thin melt, which gives more abrupt profiles, will be used in future tests. Degradation of tunnel diodes will be tested on equipment designed by P. Lanyon at SERI.

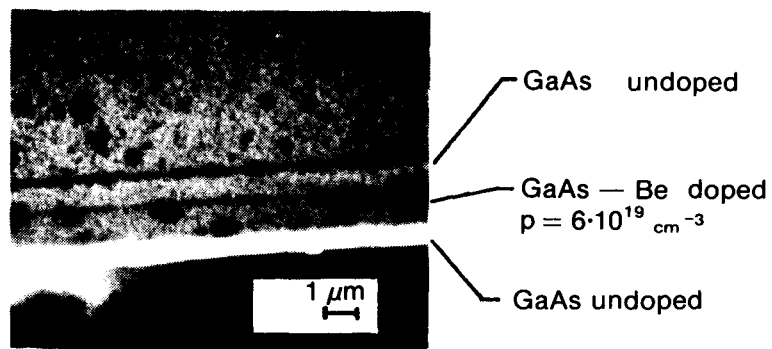


**Figure CS-4. Typical Multilayered Structure Grown by LPE for Diffusion Experiments**

### 6.3 Te Doping in GaAs

Further studies of the Te doping are planned to obtain fundamental information about the nature of Te in GaAs. For concentration of Te in the melt ( $> 10^{-2}$ ) microprecipitates of  $\text{Ga}_2\text{Te}_3$  were reported.

Nuclear gamma resonance (NGR) on  $\text{Te}^{125}$  could give pertinent information about the nature of the chemical bond and local symmetry of each kind of Te atom. In other words, NGR on  $\text{Te}^{125}$  can be distinguished from  $\text{Te}_{\text{As}}$  from  $\text{Te}_{\text{As}}^{\text{V Ga}}$  and from microprecipitates of  $\text{Ga}_2\text{Te}_3$ . (The donor level of Te results from Te in the arsenic site. But Te-doped GaAs are compensated, because a significant amount of Te form complexes with Ga vacancies to give acceptor states).

Thick layers ( $\approx 300 \mu\text{m}$ ) of  $\text{Te}^{125}$ -doped GaAs were grown by LPE to be analyzed by  $\text{Te}^{125}$  NGR (at the School of Mines, Golden, Colorado, by D. Williamson).

### 7.0 REFERENCES

1. Fraas, L. M.; Knechtli, R. C. 13th IEEE Photovoltaic Specialists Conference. p. 886 (1979).
2. Lamorte, M. F.; D. Abbot. 13th IEEE Specialists Conference. p. 874 (1979). RTI Novel Concentrator Photovoltaic Converter System Development. Final Report 11979. Lamorte, M. F., U.S. Patent 4,179,702 (1979).
3. Moon, R. L. et al. 13th IEEE Specialists Conference. p. 859 (1979).
4. Bennet, A.; Olsey, L. C. 13th IEEE Specialists Conference. p. 868 (1979).
5. Panish, M.; Illegemens, M. In Progress in Solid State Chemistry, Reiss and McCaldin, editors. Pergamon (1972).
6. Lee, H. J. et al. Phys. Rev. B. Vol. 21 (1980).
7. Monermar, B. J. Appl. Phys. Vol. 47 (1976).
8. Kaneko, K. "Electrical Properties of  $n\text{-Al}_x\text{Ga}_{1-x}\text{As}$ , Gallium Arsenide and Related Compounds." Inc. Phys. Conf. Ser. No. 33a. pp. 216 (1977).
9. Lifshite, N. et al. Phys. Rev. B. Vol. 21: p. 670 (1980).
10. Spring Thorpe, A. J.; King, F. D.; Becke, A.; J. Electronic Mat. Vol. 4: p. 101 (1975).
11. Andrews, A. M. et al. Phys. Rev. B. Vol. 5: p. 2273 (1972).
12. Sze, S. M. Physics of Semiconductor Devices. Willey-Interscience: p. 150 (1969).
13. Kane, E. O. J. Appl. Phys. Vol. 32: p. 83 (1961).
14. Bedair, S. M. J. Appl. Phys. Vol. 50: p. 7267 (1979).

15. Dupuis, R. D. et al. 14th IEEE Photovoltaic Specialists Conference (1980).
16. Zehr, S. W.; Muller, D. L.; Harris, J. S., Jr. (to be published).
17. Ilegems, M.; Schwartz, B.; Koszi, L. A.; Miller, R. C. Appl. Phys. Lett. Vol. 33: p. 629 (1978).
18. Goodwin, A. R.; Dobson, C. D.; Franks, J. Inst. Phys. Conf. Ser. Vol. 7: p. 36 (1968).
19. Poltaratskii, E. A.; Stuchechnikov, V. M. Soviet Phys. Solid State. Vol. 8: p. 770 (1966).
20. McLarge, W. V. et al. Appl. Phys. Lett. Vol. 32: p. 129 (1978).

PHOTOVOLTAIC PROPERTIES OF Si-V<sub>2</sub>O<sub>5</sub> AND  
GaAs-V<sub>2</sub>O<sub>5</sub> HETEROSTRUCTURES

Investigators: J. Gobrecht, K. Chewey, and S. Wagner

## 1.0 INTRODUCTION

The aim of this work is to investigate the photovoltaic properties of heterojunctions between vanadium pentoxide (V<sub>2</sub>O<sub>5</sub>) and silicon or gallium-arsenide. Only a few results have been reported in Si/V<sub>2</sub>O<sub>5</sub> [1,2]; the experiments have employed evaporated V<sub>2</sub>O<sub>5</sub> films, which suffer from an undesirably high resistivity. Nothing has been reported on GaAs/V<sub>2</sub>O<sub>5</sub> so far. The work is concentrated on making structures with high-conductivity V<sub>2</sub>O<sub>5</sub> films, to avoid high-cost production processes.

The results reported here are very preliminary, because the experiments started in the beginning of February 1980.

## 2.0 RESULTS

V<sub>2</sub>O<sub>5</sub> forms good rectifying junctions with both p- and n-type silicon. This was confirmed especially after a new coating process was developed for the Si-wafers: V<sub>2</sub>O<sub>5</sub> is applied from acidic solutions, which leads to very thin and homogeneous coating. Open-circuit voltages greater than 300 mV were obtained with these structures; however, short-circuit currents and fill factors are very small due to the formation of a SiO<sub>2</sub> layer at the interface during the necessary annealing process. High photoresponse was observed only under reverse bias greater than 0.5 V at p-Si/V<sub>2</sub>O<sub>5</sub> devices. At n-type Si devices, less bias was needed; however, the fill factor and the short-circuit current remained poor. Very recently, it was found that these values could be improved significantly by doping the interface oxide. Research on this subject still is going on, but the results are much better than previous data in the literature [1,2].

There is no evidence of diffusion of vanadium into the silicon, which would deteriorate the photovoltaic properties of the junction. This was proved by Auger experiments (P. J. Ireland) and carrier-lifetime measurements. The adhesion of V<sub>2</sub>O<sub>5</sub> films on silicon was generally very good. Transmission and absorption spectra of V<sub>2</sub>O<sub>5</sub> films deposited on quartz and glass substrates confirmed the values for the bandgap known from the literature, namely between 2.1 eV and 2.5 eV (Gary Cheek). On selected samples, capacity voltage dependencies were taken that basically confirm the values given by Winn et al. [1], although several anomalies were detected. The results are still being evaluated (R. Nottenburg).

Very few results can be reported on the GaAs/V<sub>2</sub>O<sub>5</sub> structures so far, mainly because the adhesion of the V<sub>2</sub>O<sub>5</sub> films to the GaAs is relatively poor. In samples which showed better adhesion on p-type and on n-type substrates, the



I-V curves showed a nearly ohmic behavior of the junction. However, these results are very preliminary as well, and the experiments are continuing.

A second project was started in parallel, which is mentioned here very briefly: the fabrication and investigation of Ge/GaAs heterostructures made by epitaxial alloying. For this, a special "low-heat-capacity" alloying apparatus has been set up that allows heating the sample sandwich to about 900°C in 5 s or cooling it in approximately the same time. In the experiments, heterostructures that had been proposed earlier by Rediker et al. [3] were produced by this procedure. The behavior of the n-Ge/n-GaAs interface was ohmic, contrary to the rectifying properties observed at this interface by Anderson [4]. Work is continuing to improve the electrical characteristics of this interface.

### 3.0 DISCUSSION

Because of the very preliminary nature of the results, they cannot be discussed at this time. A paper reporting the complete results on the Si/V<sub>2</sub>O<sub>5</sub> structure, including discussion, will be completed during the summer.

### 4.0 REFERENCES

1. Winn, O. H.; Franz, S. L.; Anderson, R. L. J. Appl. Phys. Vol. 50: p. 3758 (1979).
2. Siili, A. Kurmashev, D.; Michailovib, L.; Hevesi, I. Acta. Phys. Chem. Vol. 22: p. 45 (1976).
3. Rediker, R. H.; Stopek, S.; Ward, J. H. R. Solid State Electron. Vol. 7: p. 621 (1964).
4. Anderson, R. L. Solid State Electron. Vol. 5: p. 341 (1962).

GROWTH OF GaAs AND RELATED COMPOUNDS BY METAL-ORGANIC  
CHEMICAL VAPOR DEPOSITION

Investigators: A. E. Blakeslee, R. G. Axton

## 1.0 INTRODUCTION

Although silicon is the workhorse material of the solar industry, many compound semiconductors are capable of yielding higher efficiency solar cells than silicon, principally because their larger bandgaps lead to higher open-circuit voltages. Chief among these materials are GaAs and InP, with room temperature bandgaps of 1.43 eV and 1.34 eV, respectively. These compounds, unfortunately, are considerably scarcer and more expensive than silicon, so their higher efficiencies can be profitably utilized only in applications in which the cost of cell material is a secondary consideration, namely, for remote locations and for concentrator systems. Another useful characteristic of III-IV materials is that many of them may be combined with one another to form ternary or quaternary alloys with specially tailored properties, including the bandgap and the lattice constant. These alloys are useful for constructing "tandem" solar cells, where one cell is in a series optical path with another cell having a different bandgap, and the two cells together utilize a larger fraction of the solar spectrum than any single cell can do alone.

The ternary compound  $Ga_{1-x}Al_xAs$  plays an important role in solar cell technology. Woodall and Hovel [1] used this material as a capping layer (window) to reduce surface recombination on GaAs p-n junction solar cells and in doing so created a breakthrough in the search for higher efficiency cells. Their structures were produced by the process known as liquid phase epitaxy (LPE), and their first reported result of 15% AM1 efficiency has since been upgraded to 22% [2]. Similar results have been obtained more recently by Dupuis et al. [3] and by Nelson et al. [4] using a different crystal growth technique--that of chemical vapor deposition (CVD). In addition,  $Ga_{1-x}Al_xAs$  is an important component of several current tandem solar cell schemes.

The CVD technique is generally regarded as more flexible, more universally applicable, capable of tighter process control, and potentially less expensive than the LPE process. Hence, it is more likely to be used in possible future large-scale manufacturing efforts. However, at the present time, it suffers from at least one major disadvantage: for Al-bearing crystals, the electronic properties are extremely sensitive to contamination by traces of oxygen. This is obviated in LPE by the gettering action of the Ga melt inherent in the method. In CVD there is no such gettering, and this necessitates a degree of leak-tightness in the apparatus several orders of magnitude more stringent than has hitherto been practiced in the growth of other III-V compounds.

In view of the importance of III-V compounds and alloys to several of the key issues in current photovoltaic research and development, a study of both the LPE and the CVD methods has been initiated. A crystal growth laboratory has been set up that incorporates both techniques; this report summarizes the progress made to date in the CVD area.

## 2.0 APPARATUS DESIGN AND CONSTRUCTION

A CVD system was designed, built, and put into operation in the latter half of CY79. The particular system chosen was the MOCVD (metal-organic chemical vapor deposition) system, in which most of the source materials for the compounds grown, as well as for the dopants, are in the form of vaporizable organometallic liquids. MOCVD was pioneered in 1969 by Manasevit and Simpson [5], improved in 1971 by Blakeslee and Bischoff [6], and finally, perfected to the point of demonstrating electronic quality  $\text{Ga}_{1-x}\text{Al}_x\text{As}$  in 1977 by Dupuis et al. [3]. It is mainly this capability for producing high-quality  $\text{Ga}_{1-x}\text{Al}_x\text{As}$ , which is not possible with the more conventional chloride transport vapor phase epitaxy (VPE) process, that has caused MOCVD's recent surge of popularity for growing III-V semiconductor crystals. Other advantages are that MOCVD provides a wider range of possible compounds and yields better compositional control than does chloride VPE.

MOCVD technology has been described extensively in the literature, and the design of all systems in current use is quite standard. The system at SERI is no exception, and it will be necessary for this report to point out only its salient features. A schematic of the system is presented in Fig. GO-1, and a photograph of the completed installation is shown in Fig. GO-2. The abbreviations used in the schematic are: TMG = trimethyl gallium; TMA = trimethyl aluminum;  $\text{AsH}_3$  = arsine gas; DET = diethyl telluride; DMZ = dimethyl zinc; and HCl = hydrogen chloride gas. TMG, TMA, and  $\text{AsH}_3$  are primary sources; DET and DMZ are n- and p-type dopants, respectively; and HCl is used to hot etch the reactor and susceptor after a run in order to clean the system.

The hydrogen purifier is of the palladium-silver alloy diffusion type. All gas lines are of 316 stainless steel tubing, joined with Swagelok fittings. The flowmeters are of the rotameter type and, depending upon the bore size and float chosen, are interchangeable to cover five different ranges of gas flow. They are connected to the system with Cajon Ultra-Torr fittings. The valves shown in Fig. GO-1 as x's enclosed in circles are, except for the four built into the TMG and TMA cylinders, Nupro bellows-seal shutoff valves. The x's enclosed in squares denote Nupro bellows metering valves for controlling gas flows.

The reactor vessel (not shown in Fig. GO-1) is a vertical, unjacketed, fused quartz tube, which is fed from the reactor manifold. The susceptor is of SiC-coated graphite. Also not shown is a vent manifold that receives a constant purge of hydrogen in addition to venting the gases in the other lines (indicated by arrows) when they are not connected to the reactor.

As can be seen in the photograph (Fig. GO-2), the equipment is housed in a vented enclosure for considerations of safety. The white cabinet at the extreme left contains the cylinders of noxious gases and is also vented. The 10-kW-input, 5-kW-output RF generator is mounted on its own self-contained cooling water supply. The power to the graphite susceptor is regulated by a Eurotherm controller governed by a signal from a Pt/Pt, 10% Rh thermocouple mounted in a well in the susceptor. The refrigerating bath for maintaining the TMG at 0°C and the stainless steel cylinder containing TMA are also visible in the photograph.

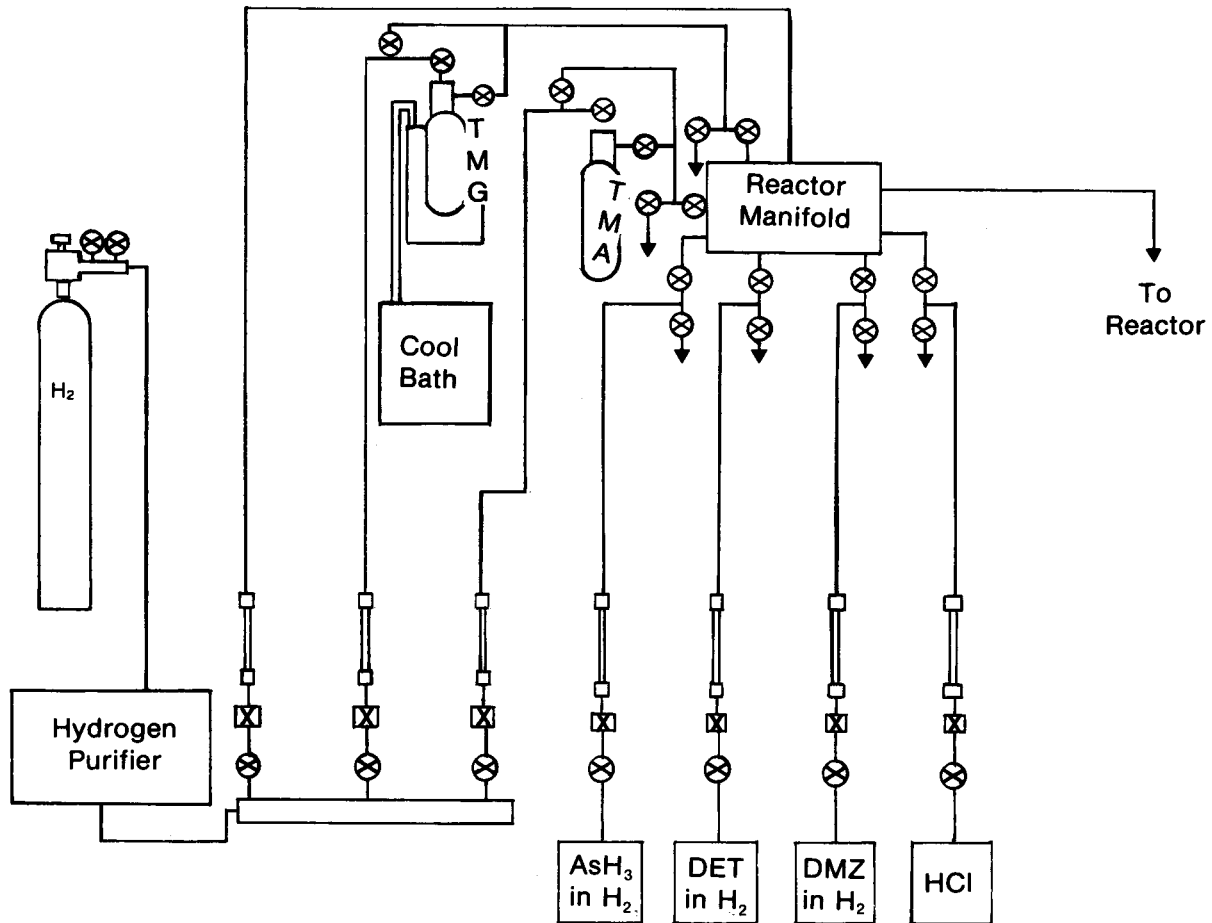
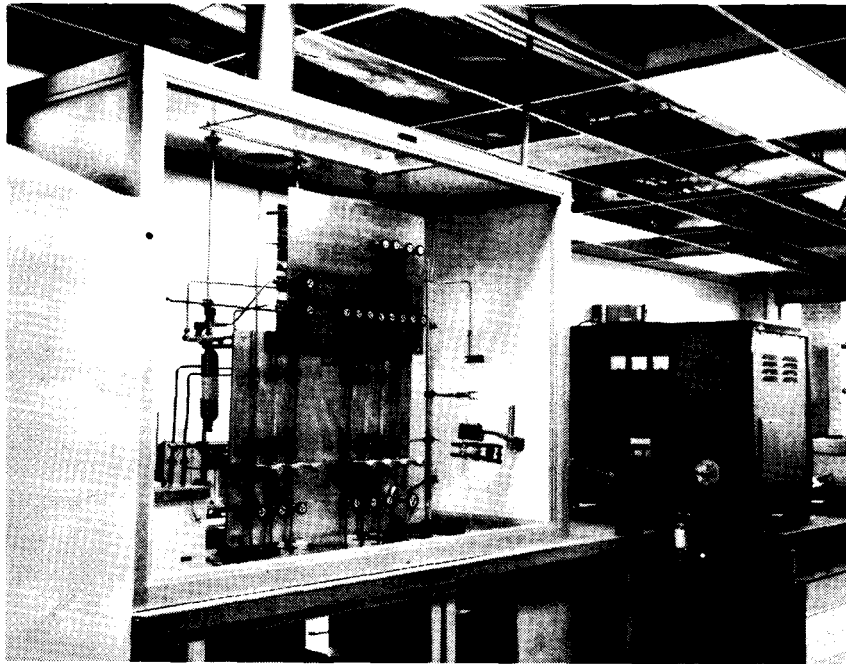


Figure GO-1. Schematic of Metal-Organic Chemical Vapor Deposition (MOCVD) Apparatus



**Figure GO-2. MOCVD Apparatus in the High-Efficiency Cell Laboratory**

### 3.0 EXPERIMENTAL RESULTS

After completion of the apparatus construction, a leak check was performed with an He leak tester. Five small leaks were found that contributed a total leak rate of approximately  $1.3 \times 10^{-6}$  standard  $\text{cm}^3$  of He per second. Assuming that the He pressure in the vicinity of the leaks was approximately equal to that of  $\text{O}_2$  in the air, and that  $\text{O}_2$  leaks into the system about one-fifth as fast as He, this translates to a leak of  $2.6 \times 10^{-7}$   $\text{cm}^3$   $\text{O}_2/\text{s}$ . If this  $\text{O}_2$  leaks into a stream of pure  $\text{H}_2$  carrier gas flowing at 2000  $\text{cm}^3/\text{min}$ , the concentration of  $\text{O}_2$  in the system is 8 ppb. Experimental evidence to be described later strongly suggests that either this low concentration is still too high for growth of good quality  $\text{Ga}_{1-x}\text{Al}_x\text{As}$  or other undetected sources of  $\text{O}_2$  contamination exist.

The system was put into operation and 14 growth runs were made, 4 for GaAs and 10 for  $\text{Ga}_{1-x}\text{Al}_x\text{As}$ . The resulting films were characterized to varying degrees by metallurgical, optical, and electrical techniques. Although intentional doping was usually not performed, a p-n junction was fabricated in one GaAs run by doping first with DET and then with DMZ. After etching a mesa and applying crude contacts, a photocurrent of a few microamperes was observed. No further work was done to optimize this crude structure. Additionally, a few heterostructures of GaAs on Ge and sapphire were grown to support other projects.

A flux of about 1  $\text{cm}^3/\text{min}$  TMG was used for all runs. The As/Ga ratio in the vapor ranged from 2 to 13. All runs but two were carried out at 700°C. It was determined that essentially all the TMG incident on a substrate surface was captured as GaAs. This process could, therefore, conserve Ga very efficiently if one could arrange to cover the full area of gas impingement with substrates. On the other hand, the high As/Ga ratios necessary for good  $\text{Ga}_{1-x}\text{Al}_x\text{As}$  growth are wasteful, but presumably a high degree of As recycling could be employed.

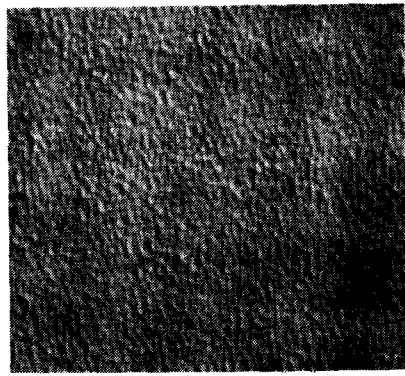
A topic-by-topic summary of the important results of the film characterizations follows.

#### 3.1 Growth Rate

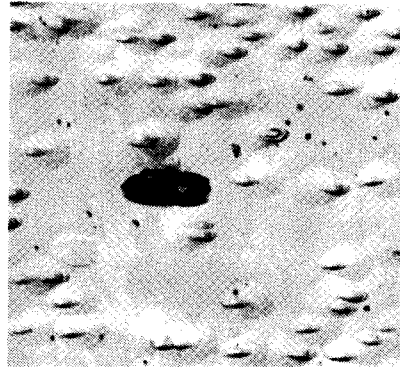
The growth rate is adequate for rapid growth of layers, thus reducing the time of high-temperature processing and minimizing interlayer diffusion. A typical rate for the fluxes quoted was 0.25  $\mu\text{m}/\text{min}$ , subject to perhaps  $\pm 50\%$  variation because of density gradients caused by convection and wall deposition in the reactor. This variation can be greatly reduced by rotating the susceptor.

#### 3.2 Surface Morphology

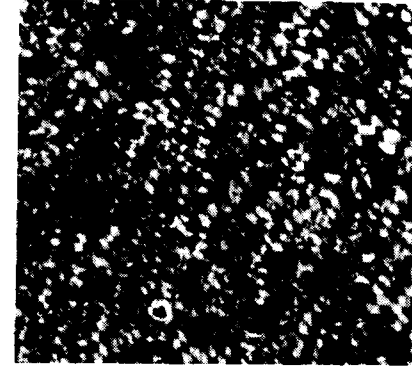
The appearance of the wafer surfaces varies from very smooth to very coarse, depending to some extent on how well the substrates were cleaned. A more general correlation, however, was that roughness increased as the Al content increased and the overpressure of As decreased. Some micrographs of typical layer surfaces and the corresponding cleavage faces are shown in Fig. G0-3.



a



b



c

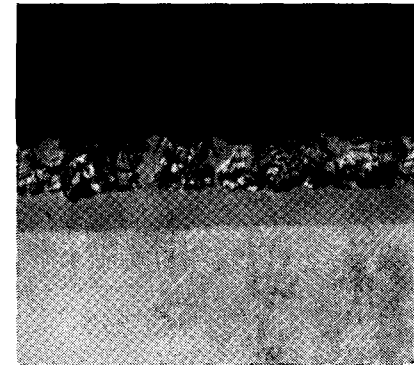
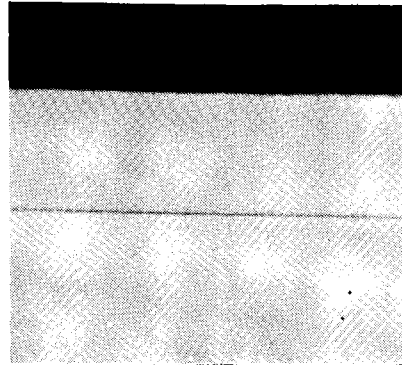
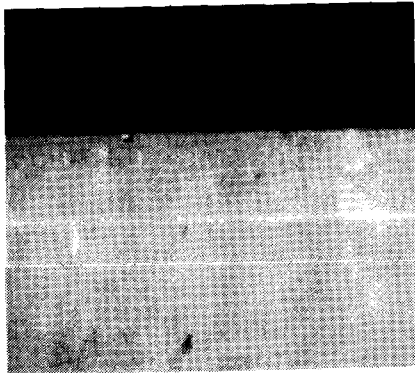


**Figure GO-3. Top Row, Surface Morphology under Nomarski Interference Contrast, All 200X; Bottom Row, View of Cleaved Epitaxial Layer, (a) and (b) 1000X, (c) 500X**

[Composition. (a) GaAs, (b)  $\text{Ga}_{0.9}\text{Al}_{0.1}\text{As}$ , (c)  $\text{Ga}_{0.5}\text{Al}_{0.5}\text{As}$ . Note that layer (c) turned partly polycrystalline midway through the growth.]

The connection between low As pressure and roughness is thought to be that formation of  $\text{Al}_4\text{C}_3$  is favored as compared to the desired AlAs when the As pressure is low. Indeed, in several instances where rough or even somewhat polycrystalline growth was observed, black carbon deposits were seen in the reactor after HCl vapor cleaning, and in one instance Auger spectroscopy detected a high concentration of carbon in the grown layer. Usually, however, the carbon content was insufficient to be detected by either Auger or SIMS, yet presumably large enough at minute points to nucleate faceted or even polycrystalline growth. An interesting illustration of this is shown in Fig. GO-4, where an epitaxial layer was cleaved through a polycrystalline nugget, one of many that were distributed over the sample surface. It is probable that trace amounts of C and O or both initiated the development of the nuggets and the surface facets as well; yet neither of these elements could be identified in the nuggets or the adjacent "good" material, nor could any difference in composition be detected between the two regions.

### 3.3 Compositional Control

As mentioned earlier, control of the composition in a solid ternary (i.e., control of the value of  $x$  in a compound such as  $\text{Ga}_{1-x}\text{Al}_x\text{As}$ ) is much easier to achieve in MOCVD than in LPE or VPE. For the latter two methods, the ratio of the concentrations of two elements such as Al and Ga in the fluid source (gas or liquid) may be a factor of several different from the corresponding ratio in the solid. In MOCVD, these ratios are virtually identical. Thus to produce a desired  $x$  in the solid, one merely has to adjust the proportion of vapor sources to the same value. This high degree of control was demonstrated repeatedly with the present MOCVD system. For example, on the basis of published vapor pressures and using calibrated flowmeters, in one run the Ga/Al ratio in the gas was 68/32; the composition of the solid was  $\text{Ga}_{0.66}\text{Al}_{0.34}\text{As}$ .

### 3.4 Electrical Properties

Hall and resistivity measurements were accurate and meaningful for GaAs; they were less so for  $\text{Ga}_{1-x}\text{Al}_x\text{As}$ . A typical undoped GaAs layer contained  $5.2 \times 10^{16}$  electrons/cm<sup>3</sup> and exhibited a room temperature mobility of 2700. Due to problems with bad contacts and/or inhomogeneous layers, the interpretation of the Hall coefficient data for  $\text{Ga}_{1-x}\text{Al}_x\text{As}$  layers was sometimes suspect and in conflict with other data. Specifically, some samples showed an n-type Hall signal when thermal probe tests indicated they were p-type. In the system certain accessory information, such as the observation of deposits of carbon, which is an acceptor atom in GaAs were more consistent with p-type material. Furthermore, the Hall mobilities of these questionable samples were very small, more characteristic of the p-type layers than of n-type. Another problem arose when the As overpressure was high enough to prevent the apparent carbon (acceptor) incorporation: the layers, unless heavily n-doped, became semiinsulating. This is a familiar problem in the growth of  $\text{Ga}_{1-x}\text{Al}_x\text{As}$  by MOCVD [6]. Its cause has been shown to be the incorporation of trace amounts of  $\text{O}_2$  in the crystals along with the Al [7,8], hence the preoccupation with elimination of atmospheric leaks discussed earlier in this report.





**Figure GO-4.  $\text{Ga}_{1-x}\text{Al}_x\text{As}$  Epitaxial Layer Containing Polycrystalline Nugget, 100X**

### 3.5 Photoluminescence

Photoluminescence at 77 K is a standard technique for assessing the quality of  $\text{Ga}_{1-x}\text{Al}_x\text{As}$ . LPE-grown  $\text{Ga}_{1-x}\text{Al}_x\text{As}$  is usually free of  $\text{O}_2$  and luminesces strongly. CVD material will luminesce with comparable efficiency if  $\text{O}_2$  incorporation is prevented [7]. None of the Al-bearing samples grown in this study exhibited band-edge photoluminescence at 77 K, even when the Al mole fraction (x) was only 0.07, nor did heat treatment in an  $\text{AsH}_3$  atmosphere improve the situation. Sharp band-edge photoluminescence was exhibited, however, by a GaAs layer which contained no Al.

### 4.0 CONCLUSIONS AND FUTURE DIRECTIONS

The status of the present MOCVD system midway through FY80 is, briefly, as follows. The system is stable and easy to operate and is capable of producing doped epitaxial or polycrystalline GaAs layers for solar cell research. It can also easily be adapted to grow layers of Si or II-VI compounds. The system is not now capable of serving its primary intended function--production of electronic-grade layers of  $\text{Ga}_{1-x}\text{Al}_x\text{As}$ --and meaningful device research with that material is not yet possible. One problem that was uncovered, the tendency to form carbon deposits accompanied by structural defects and acceptor incorporation, appears to be under satisfactory control by using a sufficient excess of  $\text{AsH}_3$ . The more serious problem of  $\text{O}_2$  deep-level formation, leading to high resistivity and nonradiative recombination, must be solved before the system can be really useful.

### 5.0 REFERENCES

1. Woodall, J. M.; Hovel, H. J. Appl. Phys. Lett. Vol. 21: p. 379 (1972).
2. Woodall, J. M.; Hovel, H. J. Appl. Phys. Lett. Vol. 30: p. 492 (1977).
3. Dupuis, R. D.; Dapkus, P. D.; Yingling, R. D.; Moudy, L. A. Appl. Phys. Lett. Vol. 31: p. 201 (1977).
4. Nelson, N. J.; Johnson, K. K.; Moon, R. L.; Vander Plas, H. A.; James, L. W. Appl. Phys. Lett. Vol. 33: p. 26 (1978).
5. Manasevit, H. M.; Simpson, W. I. J. Electrochem. Soc. Vol. 116: p. 1725 (1969).
6. Blakeslee, A. E.; Bischoff, B. K. Electrochem. Soc. Meeting. Cleveland, Ohio, October 3-7, 1971, Abstract 181.
7. Stringfellow, G. B.; Hall, H. T., Jr. J. Electron. Mater. Vol. 8: p. 201 (1979).
8. Casey, H. C., Jr.; Cho, A. Y.; Nicollian, E. H. Appl. Phys. Lett. Vol. 32: p. 678 (1978).

## THIN-FILM CELLS

Investigators: R. C. Kerns, J. Abelson

## 1.0 INTRODUCTION

Research in thin-film cells is concentrated on the study of amorphous silicon. Interest in amorphous silicon has increased since the work of Spear et al. [1] showed that it could be electronically doped by appropriate impurity atoms. In 1976, Carlson and Wronski [2] reported amorphous silicon Schottky-barrier solar cells with 4.5% AM1 efficiencies. Recently, it has been reported that efficiencies of 5.7% for p-i-n amorphous silicon solar cells can be obtained [3].

The aim of the thin-film cell effort in our laboratories is to modify amorphous silicon in ways that will lead to improved photovoltaic materials by alloying, doping, and altering the chemical bonding in the solid state. The experimental parameters normally available for pursuing this aim generally affect the system in broad and nonspecific ways (e.g., substrate temperature, system pressure, etc.). The most direct technique for modifying the material is to change the chemistry of the plasma discharge from which the solid material is deposited. It is also important to understand the physics and physical chemistry of the plasma processes leading to deposition. This program includes efforts in these latter areas as well as efforts to evaluate the material properties of the films and to produce solar cells from the materials.

## 2.0 PROGRESS

Efforts in the past reporting period have focused on building an experimental laboratory capability. Principally, this involved design and construction of the amorphous silicon deposition facility shown in Fig. TC-1, evaluation and purchase of supporting instrumentation, and preparations for an electron spin resonance (ESR) spectrometer system.

2.1 Amorphous Silicon Deposition Apparatus

The amorphous silicon deposition facility uses an RF capacitively coupled glow discharge cell similar to that described by Knights et al. [4]. This cell is mounted inside a large vacuum chamber equipped with four optical windows, one of which is occupied by a quadrupole mass spectrometer. Gas flow to the vacuum chamber is provided by an electronic flow control system. Chamber pressure is controlled independent of the gas flow by an electronically controlled throttling valve at the inlet of the Roots pumping system. A separate, baffled, LN<sub>2</sub> trapped diffusion pumping system is provided for clean system pumpdown.

The electronic flow control system accommodates as many as 11 gases multiplexed into four groups. Each group has its own electronic flow controller with capabilities appropriate for the gases in that group. Thus, one gas in each group may be selected for mixing into the gas flow stream that eventually

TC-2

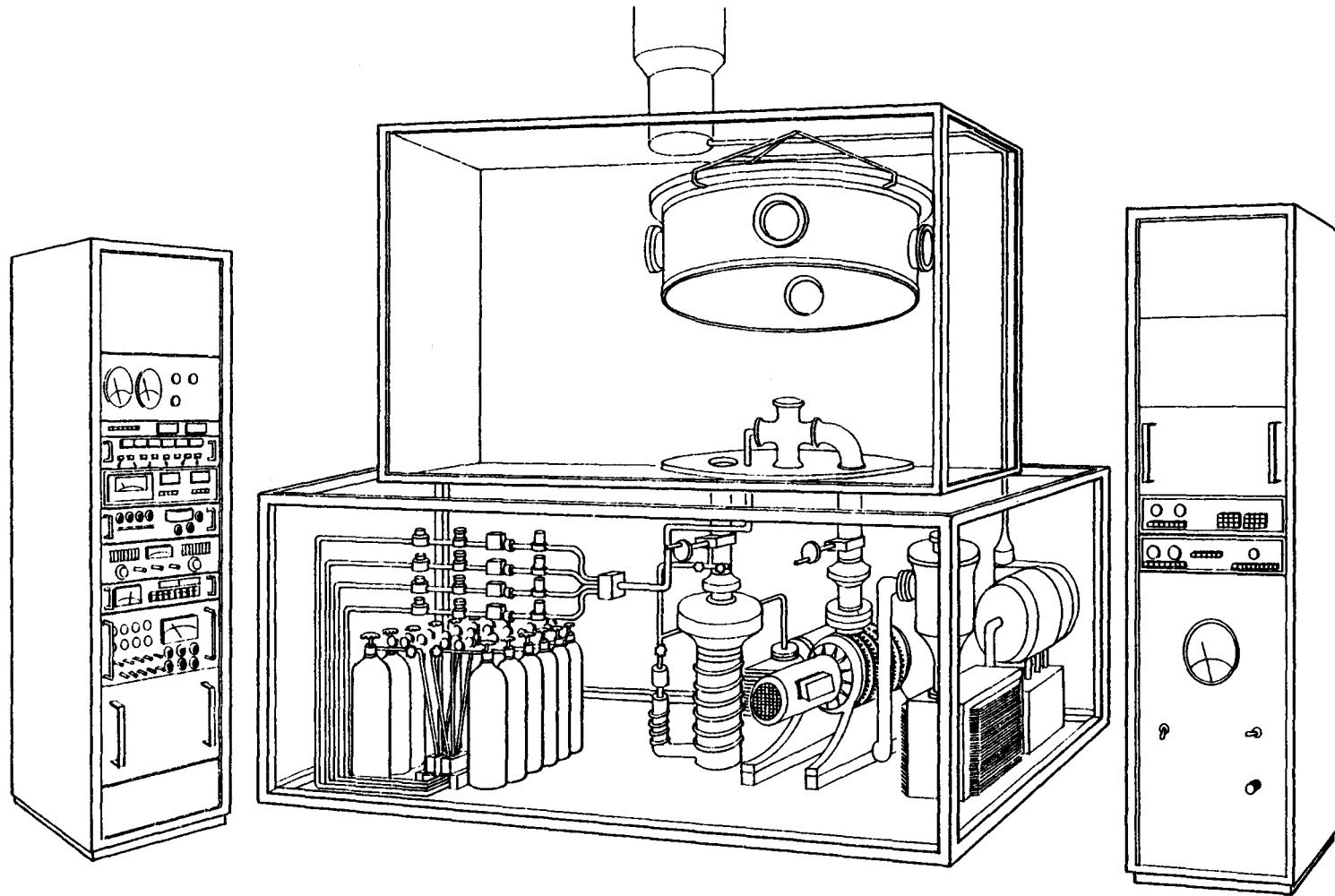


**Figure TC-1. Deposition Apparatus for Preparing Thin Films of Amorphous Materials from Plasma Discharges**

enters the chambers. The regulators for each gas bottle are equipped with cross-purge assemblies for inert gas and vacuum purging, thus avoiding contamination due to changing gas bottles.

The Roots pumping system provides high pumping capacities at the moderate vacuums used in plasma work. At the same time it can pump in a dirty or corrosive environment. A dust filter is provided between the Roots blower and its backing pump. The backing pump is ballasted with  $N_2$  to prevent buildup of silanes or other gases in the pump.

Assembly of the apparatus took place in stages involving careful cleaning of critical components to electronic-grade cleanliness, assembly of all components, and exceedingly thorough and careful leak testing of the entire system. Once assembled, all systems were tested to verify their operation according to design specifications. These systems included: (1) the gas supply handling system; (2) the vacuum purge system; (3) the inert gas purge system; (4) the flow measurement and control system; (5) the diffusion pumping system; (6) the Roots blower pumping system; (7) the vacuum chamber; (8) the chamber pressure control throttle valve; (9) the quadrupole mass spectrometer; and (10) the RF matching unit. All these systems are functioning properly.

The system is unique in several ways. It is all stainless steel construction with minimal inert O-rings. This allows wide flexibility in using gases of interest, including corrosive ones. The large vacuum chamber allows a wide variety of experiments to be set up, including various electrode geometries and some sample processing in vacuo. The entire system is designed for automation using a laboratory microcomputer system, which is on order. The system will be completely contained in an exhausted enclosure for safety. Unused reactant gases will be safely disposed of within the enclosure.

## 2.2 Electron Spin Resonance System

The electron spin resonance (ESR) system is a Varian E-109 ESR spectrometer. This system uses a 9 in. electromagnet on a rotating base and an 8 kW dc power supply. The microwave field is supplied by a rectangular Q band klystron (9.1 GHz to 9.3 GHz) coupled to the rectangular sample cavity by a section of waveguide. The system is controlled from a console supplied with the instrument.

For cooling the magnet, power supply, and klystron, an 8 kW water-to-water heat exchanger has been added. This allows very close temperature control ( $0.1^\circ\text{C}$ ) of the magnet despite building chilled water temperature fluctuations. It also assures clean cooling water free of particulates or algae, which have been problems in the past. For time-resolved studies, data manipulation, and spectrum simulation, a Nicolet ESR data system has been added. This system consists of an interface to the Varian spectrometer, a microprocessor designed for such applications, an oscilloscope for observing the signal, software, and mass storage. For hard-copy output, the system uses the X-Y plotter in the Varian console. This data system will also be used for ENDOR experiments when that capability is added.

### 2.3 Results

On 10 April 1980 the first amorphous silicon films were produced, though the deposition apparatus is not yet complete. The films are uniform, highly absorbing, black to dark brown in color, about 1- $\mu\text{m}$  to 2- $\mu\text{m}$  thick, and were prepared under ambient temperature conditions (i.e., no temperature control on the substrates). Detailed characterization of the films will be done after substrate temperature control is provided. Defect centers in amorphous silicon have been studied using electron spin resonance (ESR) and electron nuclear double resonance (ENDOR). This work was done at Xerox Palo Alto Research Center in collaboration with the researchers there. The results are preliminary, but ENDOR signals have been observed from both  $^1\text{H}$  and  $^{29}\text{Si}$  in samples with high defect densities ( $\sim 10^{18}$  spins/cm<sup>3</sup>). This work will be pursued further when the ESR/ENDOR system is operational.

### 3.0 FUTURE DIRECTIONS

In the future, we expect to continue to develop the capabilities of the deposition apparatus and begin the experimental programs on amorphous silicon. The ESR spectrometer system will be installed, tested, and used for material characterization. Experimental capability for photoconductivity and luminescence will be added. Development of plasma probes will begin in collaboration with Dr. Earl Mosburg, formerly of the Joint Institute for Laboratory Astrophysics, who is an expert in plasma instrumentation. Capabilities to be added to the deposition facility will include: substrate temperature control, waste gas disposal and monitoring, residual gas analysis, and emission spectroscopy.

Experiments are planned to: (1) determine the optimum equipment parameters for production of photovoltaic quality amorphous silicon thin films; (2) study the IR spectra of appropriately prepared samples; (3) determine optical band-gaps using optical absorption spectroscopy; (4) determine film compositions and chemical bonding using surface analysis techniques, such as SIMS, Auger, and ESCA; and (5) study minority carrier lifetimes.

The construction of solar cells will be considered after the determination of the optimum operational parameters of the deposition apparatus and when films of photovoltaic quality have been prepared as determined by spin density and photoconductivity. Because these requirements entail a great deal of work, solar cell preparation will probably occur late in the next reporting period or later.

### 4.0 REFERENCES

1. Spear, W. E.; LeComber, P. G. Solid State Commun. Vol. 17: p. 1193 (1975).
2. Carlson, D. E.; Wronski, C. R. Appl. Phys. Lett. Vol. 28: p. 671 (1976).
3. Carlson, D. E. SERI/DOE Amorphous Silicon/Materials Subcontractor's Review Meeting. Washington, D.C. April 22-25, 1980.

4. Knights, J. C. AIP Conference Proceedings No. 31. New York. p. 296  
(1976).

## SILICON PURIFICATION

Investigators: J. Olson, S. Lowe

## 1.0 INTRODUCTION

Silicon material accounts for approximately 15% to 20% of the total cost of a silicon solar cell [1]. This material is presently produced to the rigid specifications (total impurity content, less than 1 ppb) of the semiconductor industry by a costly and energy-intensive process developed 15 years ago [2]. When converted into thin, single-crystal wafers and suitably processed, this semiconductor-grade silicon will consistently yield solar cells with an AM1 efficiency close to 15% [3]. It is generally assumed, however, that economically favorable tradeoffs can be made between purity, crystallinity, and efficiency of the solar cell. For example, it has been shown that semiconductor-grade, polycrystalline silicon (with grain size of 1 mm to 5 mm) can yield solar cells with efficiencies of 10% to 14% [3,4,5]. Similarly, a less pure, or "solar grade" silicon (which has not yet been defined) should yield only slightly reduced solar cell efficiencies, and at the same time, cost significantly less than semiconductor-grade silicon at a present market cost of \$60/kg to \$80/kg. Hence, the major goal of this silicon purification project is to develop an inexpensive process that yields a material of sufficient purity and adequate solar cell performance.

The particular process being studied in SERI's laboratory is a molten salt electrochemical technique for extracting silicon from high-purity, natural quartzite. The novel contribution to previous (albeit limited) work in this area is the incorporation of a molten tin cathode that:

- does not introduce shallow doping levels in deep-level recombination centers;
- acts as an effective sink for codeposited impurities;
- precludes the formation of dendritic or powdery deposits; and
- facilitates recrystallization of the deposited (material).

The remainder of this report will develop the argument for the molten salt electrochemical production of solar-grade silicon, give a brief overview of previous work, present the results obtained to date, and enumerate areas for further studies.

## 2.0 BACKGROUND

The basic concept of an electrochemical cell is shown in Fig. SP-1a. A silicon compound,  $\text{SiO}_2$ , is dissolved in a molten fluoride. A dc bias greater than 1.1 V will drive the cell reaction,  $\text{O}^{2-}$  being oxidized at the positive anodic electrode and  $\text{Si}^{4+}$  being reduced to Si at the negative or cathodic electrode.



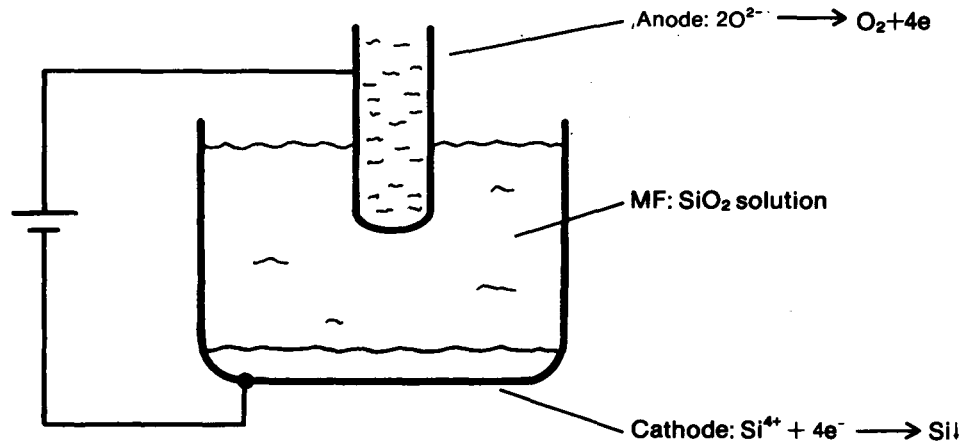


Figure SP-1a. Electrowinning of Silicon

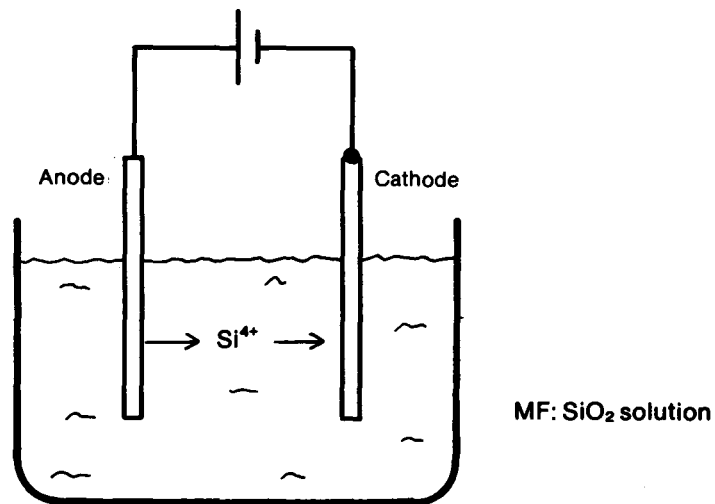


Figure SP-1b. Electrorefining of Silicon

The advantages of this technique are many. The pyrometallurgical process for the reduction of  $\text{SiO}_2$  requires temperatures in excess of  $1800^\circ\text{C}$  [6]. Commercial molten salt electrowinning processes operate at temperatures less than  $1000^\circ\text{C}$  [7]. Problems of materials compatibility are mitigated, and contamination of the product by side reactions is reduced.

The decomposition potential for a given species in solution is fairly unique. Table SP-1 contains a list of a number of oxides and their standard potentials computed from their free energies of formation using the equation

$$E^0 = -\Delta G / nF,$$

where  $F = 96,500$  coul. and  $n$  is the number of electrons involved in the cell reaction.  $\Delta G$  is the standard free energy for the cell reaction and  $E^0$  is the standard potential. Note that if C (graphite, carbon) is involved in the cell reaction, the free energy and hence the standard potential is reduced. For a cell operating at a potential  $\phi$ , any species in solution  $\phi < E_i^0$  will be reduced at the cathode. Any species for which  $E_i^0 > \phi$  will remain in solution. Hence, electrochemical reduction is a chemically selective process. On the other hand, a pyrometallurgical process is essentially nonselective. Hence, one expects to obtain a product of higher purity from an electrochemical process.

Electrochemical processing is versatile; it can operate in any one of three modes--electrowinning (electroreduction), electrorefining, or electrocrystallization. Figure SP-1b illustrates the refining mode of operation. The anode is the material to be refined. Impurities that are more noble than Si remain at the anode. Less noble impurities go into solution, but are not discharged at the cathode. In general, this process can be combined with the electrocrystallization technique.

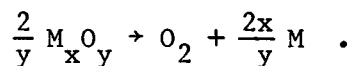
For example, using a molten salt technique, aluminum is refined to a purity of 99.99<sup>+</sup>%. The cell operates at  $950^\circ\text{C}$ , the cathode is molten aluminum, and the anode is an aluminum alloy with 30 wt % copper. The cost of this high-purity aluminum is \$3/kg.

Although the idea of electrowinning Si from  $\text{SiO}_2$  via molten salt is not new, it has received only cursory attention. Silicon was first electrowon from a solution of  $\text{Na}_3\text{AlF}_6:\text{NaCl}:\text{SiO}_2$  by Minet in 1891 [8]. Fortunatov [9], some 45 years later, extracted Si from a molten solution of  $\text{NaHCO}_3:\text{Al}_2\text{O}_3:\text{SiO}_2$  and Doderio [10], by a secondary reaction, extracted Si from  $\text{M}_2\text{O}:\text{SiO}_2$ , where  $\text{M} = \text{K}, \text{Na}$ . In 1958, a series of papers by Monnier et al. [11-13] produced a renewed interest in the molten salt electrochemistry of silicon. Of significant importance was the first demonstration of a molten salt electrorefining process for silicon [13]. The anode was a Cu-Si alloy (16.5 w/o Si), the electrolyte was  $\text{Na}_3\text{AlF}_6$  (cryolite), and the cathodic product was 99.99% pure Si. More recently, Grjotheim et al. [14-17] have correlated the decomposition voltage for  $\text{SiO}_2$  with its free energy formation. Cohen and Huggins [18], using a configuration similar to electrorefining, were able to obtain homoepitaxial deposition of single-crystal silicon. Frazer and Welch [19] made the first attempt to determine the mechanism of the cathodic reaction in a cryolite-silicon deposition system. Their results indicated that the reduction mechanism involves a slow predissociation of an

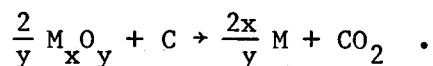
Table SP-1. STANDARD ELECTRODE POTENTIALS AT 1300 K (Calculated from Data Contained in "Free Energy of Formation of Binary Compounds," T. B. Reed, MIT Press, 1971.)

	$E_i^0(\text{v})^a$	$E_c^0(\text{v})^b$
$\text{Al}_2\text{O}_3$	-2.21	-1.19
$\text{ZrO}_2$	-2.20	-1.18
$\text{Li}_2\text{O}$	-2.13	-1.11
$\text{TiO}_2$	-1.85	-0.83
$\text{SiO}_2$	-1.76	-0.74
$\text{B}_2\text{O}_3$	-1.63	-0.61
$\text{MnO}$	-1.50	-0.48
$\text{VO}_2$	-1.30	-0.28
$\text{Na}_2\text{O}$	-1.17	-0.15
$\text{Fe}_2\text{O}_3$	-0.83	+0.18
$\text{P}_2\text{O}_5$	-0.83	+0.19

$^a E_f$  calculated from  $\Delta G$  for the reaction



$^b E_c$  calculated from  $\Delta G$  for the reaction



oxy-fluoro silica complex. The following reaction was studied by Fellner and Natiasovsky [20]:  $\text{Na}_3\text{AlF}_6 + \text{SiO}_2 \rightleftharpoons \text{NaAlO}_2 + 2\text{NaF} + \text{SiF}_4(\text{g})$ ,  $\Delta G_{1300\text{ K}}^0 = 37.54 \text{ kcal}$ . With the addition of  $\text{Al}_2\text{O}_3$  to the solution, the solubility of the  $\text{SiO}_2$  in  $\text{Na}_3\text{AlF}_6$  increases, and the fugacity of  $\text{SiF}_4$  and consequent loss of silicon decreases, indicating the existence of a stable Si-Al oxy-fluoro complex. The alumina-cryolite system has been studied extensively [21-29], and fruitful applications of these results are expected.

A number of excellent reviews [30-37] have been written that address general aspects of molten salt electrochemistry. Available are detailed discussions of furnace design, high-temperature envelopes and crucibles, melt preparation techniques, electrode materials, measurement techniques, physical models of transport, double-layer and electron-transfer phenomena, chemical models for complexation, redox and acid-base properties, and finally the advantages and disadvantages of molten salt electrochemistry as compared to aqueous and non-aqueous low-temperature electrochemistry. Several recent reviews deal exclusively with molten fluorides and their unique properties and problems [38,39].

### 3.0 EXPERIMENTAL

A schematic of the cell-furnace arrangement is shown in Fig. SP-2. The cell diameter is 35 mm. Cell materials are high-purity quartz and graphite or vitreous carbon. Ambient argon contains less than 1 ppm  $\text{O}_2$  or  $\text{H}_2\text{O}$ . The quartz muffle is sealed at both ends with water-cooled, Ni-plated brass end caps with O-ring feedthroughs for cathode, anode, and quartz windows. The furnace shell is a pyrex tube coated with a thin, semitransparent film of gold. For long-term electrolysis experiments, the cell is fitted with a quartz current shield. A graphite spacer separates the Sn from the quartz shield so as to prevent the Sn from creeping up the sides of the quartz shield.

For current efficiency studies, the current shield is not used, since it is a constant source of dissolved  $\text{SiO}_2$ . For small overpotentials, however, the characteristics of the cathode are dominated by the molten tin with virtually no deposition on the vitreous carbon wall.

The electrolyte is generally a mixture of  $\text{Na}_3\text{AlF}_6$  (99.5%) and 20 w/o LiF (99.99%). The reagents are vacuum dried in situ at  $200^\circ\text{C}$  for 12 h. Further purification of the electrolyte is achieved by preelectrolysis at a cell voltage of 2.6 V with an end point of  $10 \mu\text{A}/\text{cm}^2$  at the cathode.

Most of the results to be presented in this report are for a two-electrode cell configuration. Recently, a reasonably stable reference electrode has been developed that will permit working with a three-electrode cell and obtain the much-needed thermodynamic and kinetic data from the process.

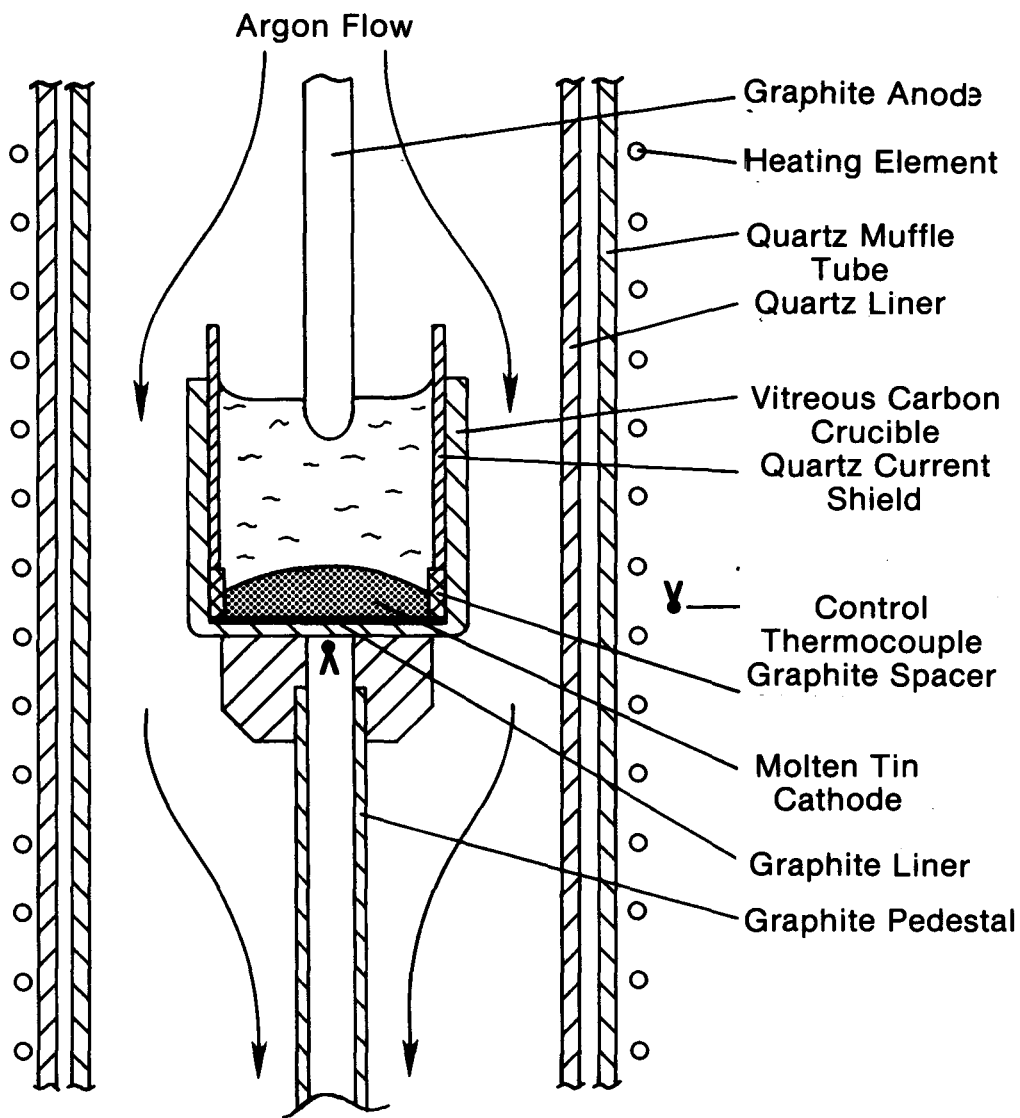
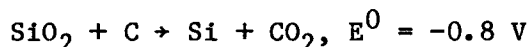


Figure SP-2. Schematic of Electrolysis Cell

## 4.0 RESULTS AND DISCUSSION

### 4.1 Current-Voltage Measurements

The curve in Fig. SP-3 is generated by measuring the response (current) of cell to a sawtooth stimulus (voltage). With suitable care, the important characteristics of this curve are reproducible. The voltage regime where the cell current begins to deviate from zero correlates well with the standard potential  $E^0$  for the reaction



Reaction and diffusion overvoltages at the carbon anode, known to be on the order of 0.3 V to 0.5 V, are the major sources for the discrepancy. The residual or background current is less than  $50 \mu\text{A}/\text{cm}^2$ , but the curve does reveal the presence of impurities as small, broad peaks at  $\phi = -1.0$  and  $-0.7$ . The absence of an inverted peak to the immediate left of the silicon reduction wave can, with caution, be interpreted as an indication of an irreversible anode reaction. An unequivocal determination can be obtained only by use of a stable reference electrode.

### 4.2 Electrochemical Current Efficiency

From a production standpoint, current efficiency (CE) is an important variable; high efficiency means lower cost. A low CE can be indicative of

- a back reaction between products of the cell reaction;
- parasitic side reactions;
- loss of material, e.g., vapor losses and inefficient recovery techniques; and
- excessive electronic conductivity.

Unfortunately, the cause is harder to determine than the effect.

Two methods for measuring the CE of the silica-cryolite system have been used. The first technique compares the integrated current,  $Q$ , with the mass of the  $\text{SiO}_2$  added to an initially pure molten electrolyte. A CE in the range of 95% to 99% is routinely measured. The end point  $Q_\infty$  for this technique is determined by extrapolating a plot of  $I$  versus  $Q$  to  $I = 0$ , where

$$Q(t) = \int_0^t I dt \text{ and } Q_\infty = Q(\infty) .$$

Figure SP-4 is a typical plot of  $I$  vs.  $Q$ . Note that near the end point  $Q_\infty$ ,  $I$  is a linear function of  $Q$ . In general, however, the functional is much more complex and, with additional information, can yield important mechanistic data. The second method compares  $Q$  with the mass of the recovered product. Using this technique, recoverable product efficiencies (RPE) are in the range of 40% to 50%. The cause of this low RPE is not known for certain at this time, but in light of the previous results, it is suspected that it is due to

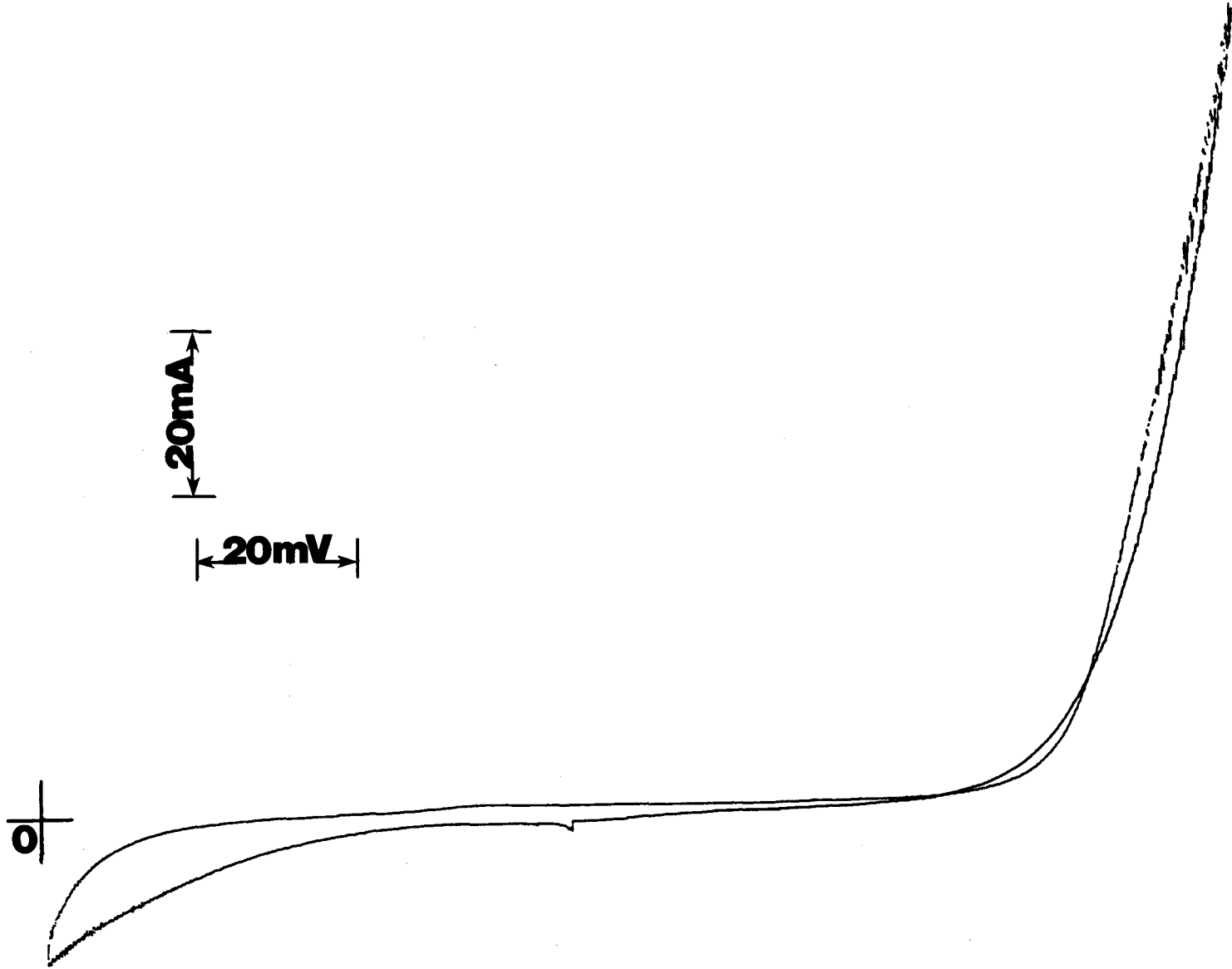
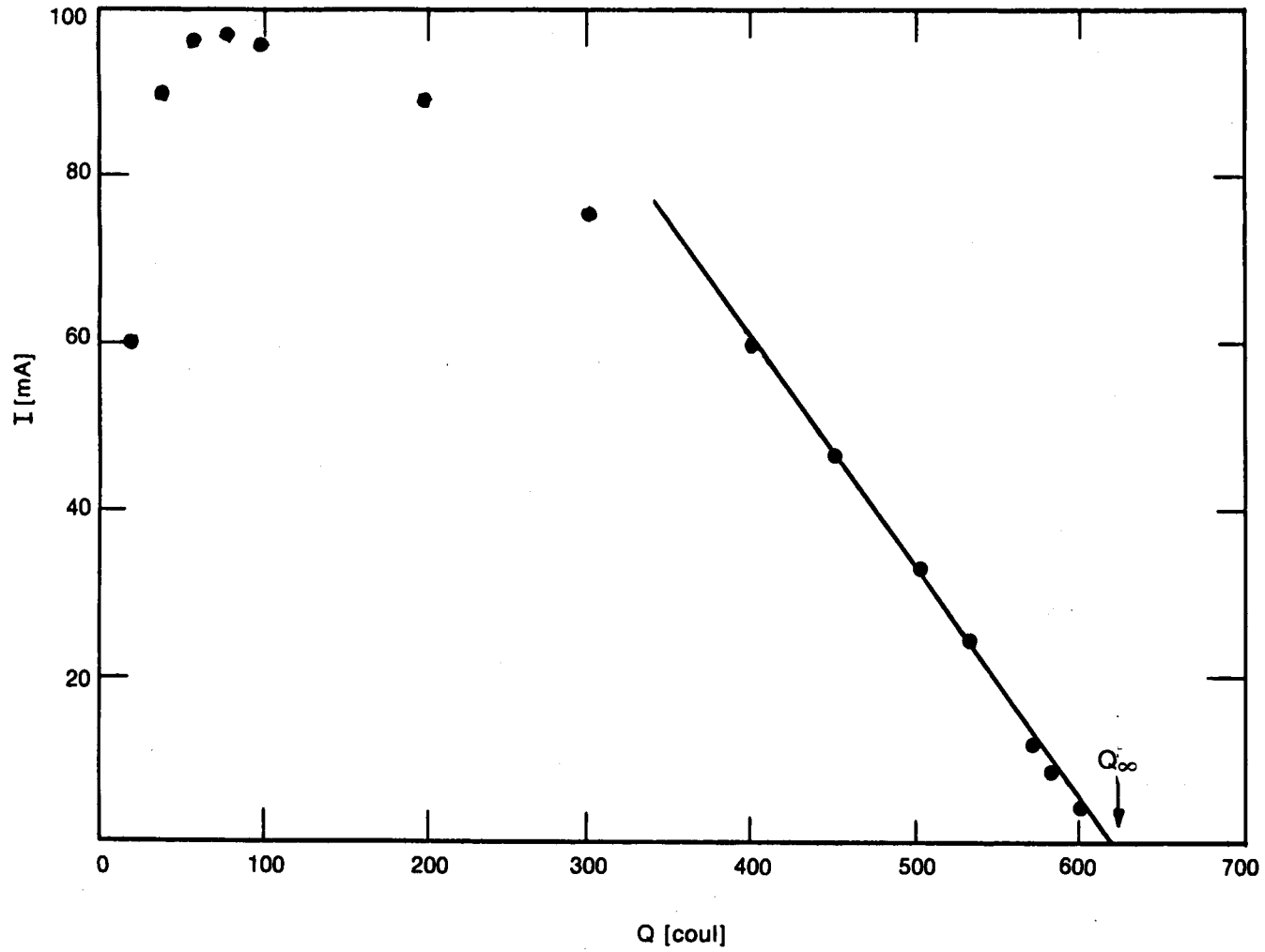


Figure SP-3. Cell Polarization Curve (25 w/o LiF, saturated SiO<sub>2</sub>, T = 860°C, area of cathode = 8 cm<sup>2</sup>)



**Figure SP-4. Cell Current vs. Integrated Cell Current  $Q$**  (Background current =  $10 \mu\text{A cm}^{-2}$ , mass of  $\text{SiO}_2 = 0.0934 \text{ g.}$ )



poor product recovery techniques, which include acid leaching and separation by filtration.

#### 4.3 Product Morphology

Previous attempts at depositing silicon on a solid (graphite) electrode invariably yielded a dendritic or powdery deposit, probably because the mass-transfer rate is diffusion-limited, which, in turn, leads to strong local variations in the growth rate. In contrast, the material recovered from a molten tin cathode is predominantly in the form of large (2 mm - 3 mm) crystallites as shown in Fig. SP-5. Microscopic examination of the Si:Sn matrix shows that the silicon growth occurs via a path similar to the vapor-liquid-solid (VLS) mechanisms. Electron transfer and silicon deposition occur preferentially at the molten-tin electrolyte interface. Silicon crystal growth then proceeds via a solution growth mechanism.

One can postulate the existence of critical current density for which the silicon reduction rate exceeds the rate at which silicon diffuses into the tin. At this point, the tin surface will become supersaturated. At a critical supersaturation, spontaneous nucleation and rapid, complete surface coverage will result. For current densities of less than 50 mA/cm<sup>2</sup>, this has not been observed.

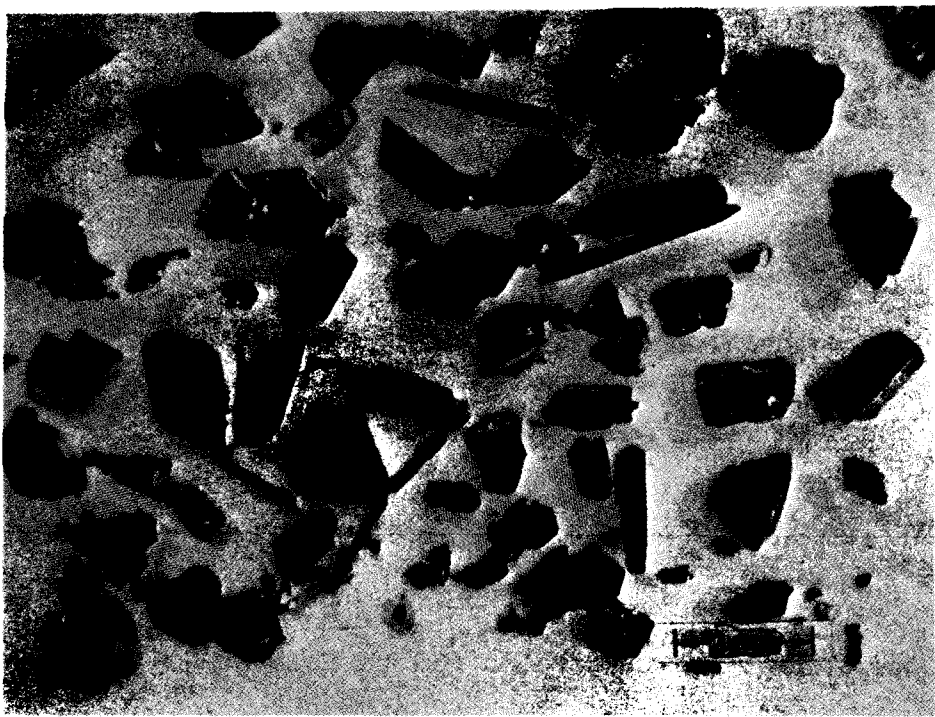
#### 5.0 FUTURE PLANS

Future work will concentrate on the bulk impurity content of electrochemically deposited silicon. Initial studies will be conducted on an extremely pure system (SiO<sub>2</sub>, electrolyte, crucible, and electrode materials) with the goal of obtaining a baseline for future comparison. Electrochemical "distribution coefficients" of various dopants (B, Al, Ti, Fe, V, Ni, Cu, etc.) will then be determined by controlled addition of the impurity oxide and chemical analysis of the doped deposit by spark source mass spectrometry and IR spectroscopy. A spinoff of these experiments will be the compilation of an electrochemical series.

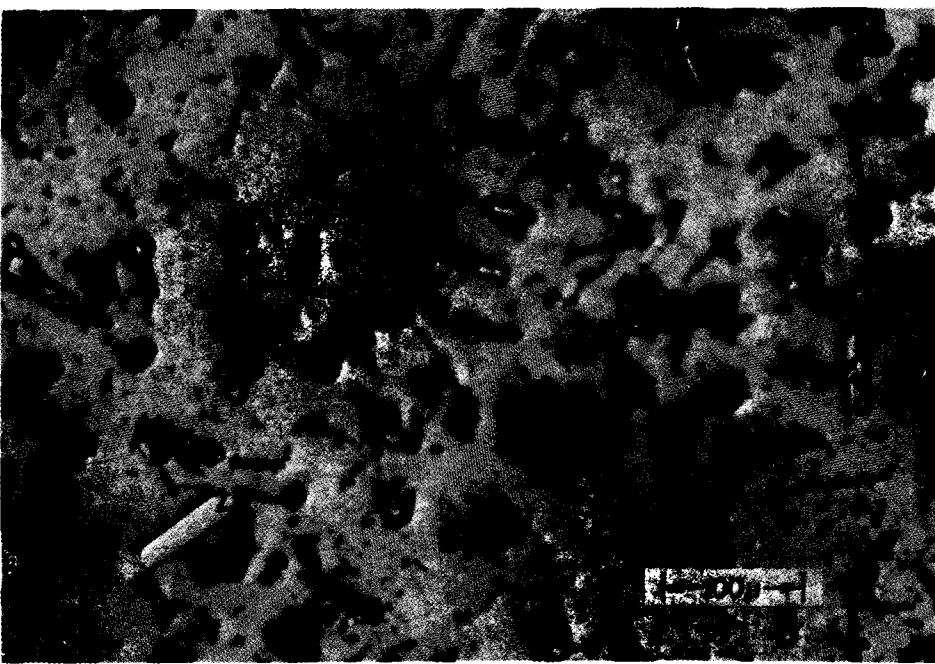
Modes of molten salt electrorefining will also be investigated. This process has applications as a potential method for refining metallurgical-grade silicon. As mentioned previously, a 99.99% pure silicon product has been obtained from a Cu-Si alloy.

Determining the real advantages and limitations of molten salt electrocrystallization of silicon is of critical importance. From an economic standpoint a one-step process that converts SiO<sub>2</sub> into solar-grade, thin-film silicon has tremendous cost-saving potential. Problems and contradictions abound. Cohen and Huggins [18] claim that the formation of an oxide film on the cathode when dissolved oxides are present precludes stable growth; stable growth is limited to oxide-free solutes and solvents [18]. However, Sethi [37] claims that in molten fluorides under cathodic conditions, oxide layers are totally removed.

Of central importance to the successful execution of these tasks will be the development of expertise in molten salt electrochemistry. To this end, it is



(a)



(b)

**Figure SP-5. Silicon Electrodeposited on (a) Molten Tin Cathode; (b) Solid (Graphite) Cathode**

anticipated that a significant fraction of the time will be devoted to the study of the basic problems germane to the electrochemical processing of silicon. This will include, for example, studies of electron transfer mechanisms in molten salts using state-of-the-art measurement techniques, such as chronocoulometry, chronopotentiometry, cyclic voltammetry, and ac impedance. A complete electron transfer mechanism study will require a detailed knowledge of the structure of the electroactive species. Raman and infrared spectroscopy will be used to attack this problem.

## 6.0 REFERENCES

1. Aster, R. W.; JPL, Document No. S-101-68, May 1978.
2. Reuschel, K.; Kersting, A. U.S. Patent 3,200,000 (1965). Sandmann, H.; Rucha, U., U.S. Patent 3,286,685 (1966). Gutsche, H. U.S. Patent 3,330,251 (1967).
3. "Large Area Silicon Sheet by EFG." Mobil-Tyco Solar Corp. Document ERDA-JPL-954355-77/4, December 1977.
4. Seidensticker, R. G.; Hopkins, R. H.; McHugh, J. P.; Duncan, C. S.; Blais, P. D.; Davis, J. R.; Rohatgi, R. 13th PVSC, IEEE, Washington, D.C. (1978).
5. Baghadi, A.; Gurtler, R. W.; Legge, R.; Ellis, R. J.; Sopori, B. 13th PVSC, IEEE, Washington, D.C. (1978).
6. Crossman, L. D.; Baker, J. A. "Semiconductor Silicon, 1977." Electrochemical Society, Princeton, N.J. (1977).
7. Shreve and Brink. Chemical Process Industries. McGraw-Hill. p. 224 1978.
8. Minet, A.; Hebd, C. R. Seane. Acad. Sci. Vol. 112: p. 1215. Paris, France (1891).
9. Fortunatov, N. S. Zap. Inst. Khim. Ukr. Acad. Nauk. Vol. 2: p. 257 (1935).
10. Dodero, M. Bull. Soc. Chim. Fr. Vol. 6: p. 209 (1939).
11. Monnier, R.; Barakat, D. Ind. Chim. Belge. Suppl. I. C. R. Congr. Intern. Chim. Ind. Liege (1958).
12. Monnier, R.; Grandjean, P. Helv. Chim. Acta. Vol. 43: p. 2163 (1960).
13. Monnier, R.; Giacometti, J. C. Helv. Chim. Acta. Vol. 47: p. 345 (1964).
14. Grjotheim, K.; Matiasovsky, K.; Fellner, P.; Silny, A. Can. Met. Quart. Vol. 10: Chapt. 2; p. 79 (1971).
15. Boe, G.; Grjotheim, K.; Matiasovsky, K.; Fellner, P. Can. Met. Quart. Vol. 10: Chapt. 2; p. 79 (1971).

16. Ibid. Vol. 10: Chapt. 4; p. 281 (1971).
17. Ibid. Vol. 11: Chapt. 3; p. 463 (1972).
18. Cohen, J.; Huggins, R. A. J. Electrochem. Soc. Vol. 123: p. 381 (1976).
19. Frazer, E. J.; Welch, B. J. Electrochim. Acta. Vol. 22: p. 1179 (1977).
20. Fellner, P.; Matiasovsky, K. Chem. Zvesti. Vol. 27: p. 737 (1973).
21. Ratkje, S. . Electrochim. Acta. Vol. 21: p. 517 (1976).
22. Mamantov, G. et al. In Proc. Inter. Sym. on Molten Salts. p. 234. Electrochemical Society, Princeton (1976).
23. Dewing, E. W. Ibid. p. 352.
24. Thonstad, J.; Rolseth, S. Ibid. p. 393.
25. Morris, D. R. Ibid. p. 469.
26. Thonstad, J. Electrochim. Acta. Vol. 14: p. 127 (1969).
27. Thonstad, J. Electrochim. Acta. Vol. 15: p. 1569 (1970).
28. Thonstad, J. Electrochim. Acta. Vol. 15: p. 1581 (1970).
29. Calandra, A. J.; Castellano, C. E.; Ferro, C. M. Electrochim. Acta. Vol. 24: p. 425 (1979).
30. Mamantov, G.; Osteryoung, R. A. In Characterization of Solutes in Non-aqueous Solvent. G. Mamantov, ed. (1976).
31. Boxall, L. G.; Jones, H. L.; Osteryoung, R. A. J. Electrochem. Soc. Vol. 120: p. 223 (1973).
32. Combes, R.; Levelut, M. N.; Tremillon, B. Electrochim. Acta. Vol 23: p. 1291 (1978).
33. Graves, A. D.; Hills, G. J.; Inman, D. In Advances in Electrochemistry and Electrochemical Engineering. Vol. IV. P. Delahay, Ed. Wiley-Interscience, New York. (1966).
34. Janz, G. J.; Reeves, R. D.; Ibid. Vol. V. (1967).
35. Jain, R.; Gaur, H. C.; Frazer, E. J.; Welch, B. J. J. Electroanal. Chem. Vol. 78 (1977).
36. Inman D.; White, S. H. J. Appl. Electrochem. Vol. 8: p. 375 (1978).
37. Sethi, R. S. J. Appl. Electrochem. Vol. 9: p. 411 (1979).

- 
38. Mamantov, G. In Molten Salts, Characterization and Analysis. G. Mamantov, ed. Marcel Decker, New York (1969).
  39. Bamberger, C. E. In Advances in Molten Salt Chemistry. Vol. III. J. Braunstein et al., eds. Plenum, New York (1975).

## SILICON CRYSTALLIZATION

Investigators: T. Ciszek, J. Hurd

## 1.0 INTRODUCTION

Research in silicon crystal growth during this period has concentrated on investigating melt growth processes with a potential for low-cost silicon sheet formation. The two techniques pursued involve sheet support structures that allow silicon continuity from the front to the back sheet surface. One technique is contiguous capillary coating [1] of silicon on and in open-pore carbon sheets. The second technique is edge-supported pulling. Here, two parallel wettable filaments are immersed in liquid silicon, and a meniscus is stabilized between the filaments and a wettable cross-member. As the cross-member, with filaments attached, is pulled away from the liquid, a solid sheet of silicon is grown that is bonded by the cross-member, the filaments, and the liquid meniscus.

## 2.0 STATUS SUMMARY

2.1 Contiguous Capillary Coating

## 2.1.1 Apparatus

Silicon sheets were grown by a process of substrate dipping similar to that used for silicon-on-ceramic (SOC) growth [2]. A vertical quartz tube furnace of 94-mm diameter with water-cooled end connections was used to contain the graphite hot-zone components under an argon environment. Heating was provided by an external RF work coil. The graphite hot-zone components and a perforated graphite substrate are shown in Fig. SC-1. The furnace shell and an opaque quartz insulator tube that normally is placed between the furnace shell and the hot-zone components have been omitted for clarity in Fig. SC-1. The substrates were mounted on a mechanically actuated stainless steel shaft that passed through an oval gas port in the furnace top plate. This port could be sealed for heating in a vacuum ambient (e.g., for baking out hot-zone components or substrates).

Thermal balancing during sheet growth was provided by two inert gas jets directed at the right and left edges of the substrate [3]. This system was useful for ensuring a uniform sheet thickness across the substrate. Melt temperature was controlled with a closed-loop system utilizing an optical radiation detector, focused on the susceptor, as the sensor. It was also possible to conduct the sheet growth experiments with only manual control of temperature.



**Figure SC-1. Hot-Zone Components for Contiguous Capillary Coating of Silicon on Porous Substrates**

### 2.1.2 Substrates

Two carbon grid structures were used as substrates: a bulk graphite machined into sheets as large as  $60 \times 40 \times 0.5$  mm in size, after which 1.5-mm diameter holes were drilled on 2.5-mm centers; and sheets of reticulated vitreous carbon, which is a very porous, open-structure glassy carbon. The two types of substrate are shown in Fig. SC-2.

### 2.1.3 Perforated Bulk Graphite Sheets

Perforated bulk graphite sheets of Poco Graphite grade DFP or Union Carbide-grade CMB are useful for the first type of substrate. However, both have some drawbacks: DFP sheets tend to warp while being coated with silicon; CMB sheets have a closer thermal expansion match to silicon and provide flatter silicon coatings. However, CMB graphite sometimes exhibits hairline cracks upon immersion in liquid silicon.

The morphology and grain size of silicon films on perforated sheet-graphite substrates are highly dependent on the silicon thickness. If the silicon film is thin, the influence of the graphite upon grain nucleation is such that a large number of fine grains are present. For example, Fig. SC-3 shows a region near a 1.5-mm hole in a DFP graphite substrate. Silicon solidified in the hole exhibits grains on the order of 0.1 mm in size, whereas the grains on the graphite adjacent to the hole are less than 0.02 mm in size. If a thick film of silicon is grown (0.5 mm - 1 mm), grains up to 0.5 mm in size are observed, as shown in Fig. SC-4. Less surface undulation is observed for thick films than for thin films, where the peak-to-peak surface variations are on the order of 40  $\mu$ m with a periodicity equal to the hole spacing. Film thickness is controlled by pulling speed and crucible temperature. Lower temperatures and/or slower pulling speeds produce thicker films.

### 2.1.4 Reticulated Vitreous Carbon

Reticulated vitreous carbon foams with porosity values of 24, 18, and 6 pores/cm were also tried as substrate materials. The corresponding approximate pore sizes are 0.4 mm, 0.6 mm, and 1.7 mm. Figure SC-5 shows the surface morphology of silicon sheets grown on these substrates. Excessive surface undulations are present with 1.7-mm pore size. The 0.4-mm pore size exhibits problems with incomplete wetting by liquid silicon at the interior of the sheet, although exterior surfaces appear completely filled. It is likely that intermediate pore sizes (0.6 mm - 1 mm) would have the best relative potential for cell substrates. As with perforated sheets, the morphology and grain size are thickness dependent. Again, the flattest surfaces and largest grains are attained with thick Si films (0.5 mm - 1 mm). Here the grain morphology is similar to that shown in Fig. SC-4 for graphite sheets.

Sheets were grown on reticulated vitreous carbon substrates over speeds ranging from 0.8 cm/min to 6 cm/min. At the higher rates, the solid/liquid interface was as much as 12 mm above the top of the meniscus, and growth progressed in a dendritic fashion from numerous nucleation sites.



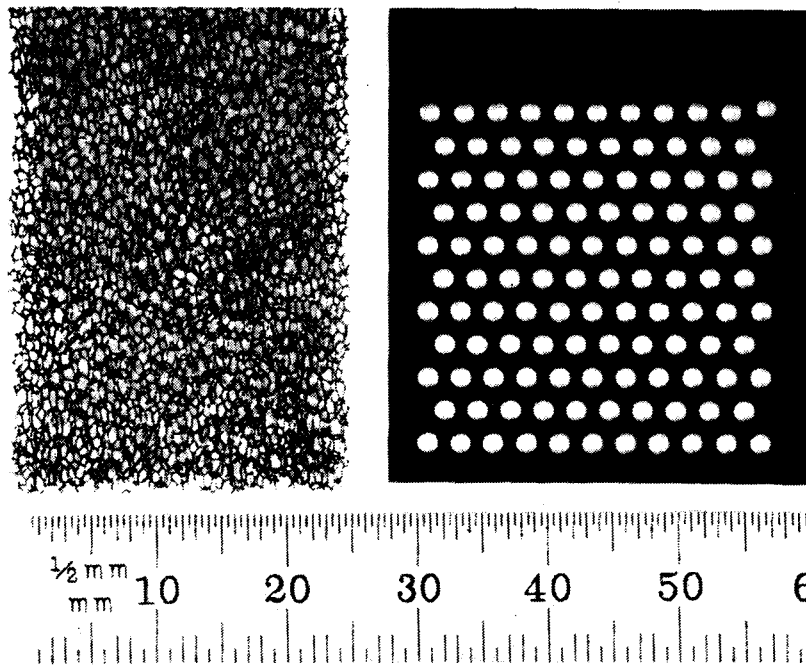


**Figure SC-2. Reticulated Vitreous Carbon (left) and Perforated Graphite Sheet (right) Substrates**

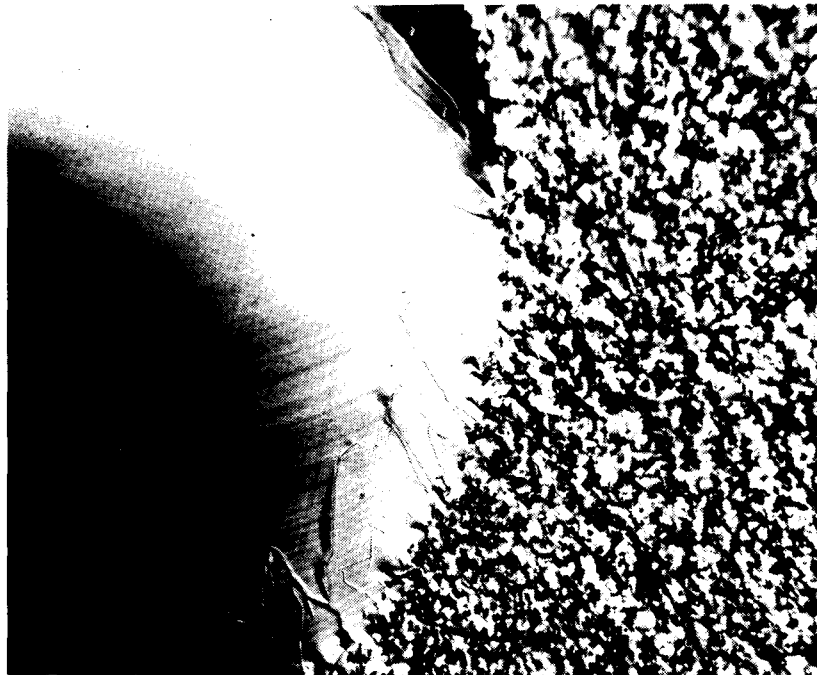


**Figure SC-3. Grain Size Variation in a Thin Silicon Film near a 1.5-mm-Diameter Perforation in the Graphite Substrate (72X)**

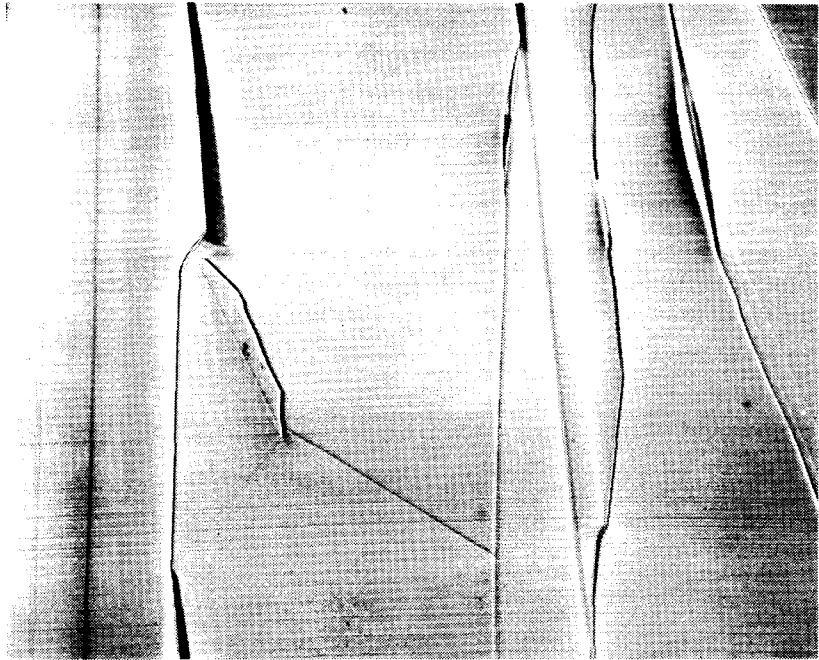


**Figure SC-4. Typical Grain Configuration for a Thick Si Film on a Perforated Graphite Substrate (72X)**

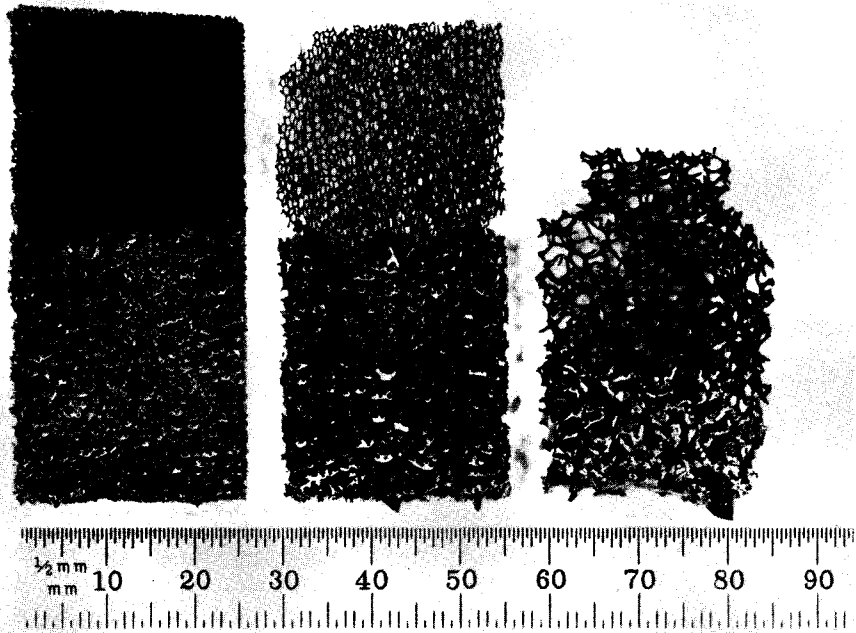


**Figure SC-5. Several Porosity Grades of Reticulated Vitreous Carbon Contiguously Coated with Silicon (24, 18, and 6 pores per cm)**

### 2.1.5 Cell Performance

Considerable difficulty has been encountered in attempts to make solar cells form contiguously coated silicon sheets. Problems include substrate exposure during chemical etching, burning of the graphite during diffusion, poor grid definition due to undulating surfaces, unexpectedly low 4-probe resistivity values apparently from contaminants in the substrate, hollow or void areas at the sheet interior, and excessive shunting.

To date, only three cells have been successfully fabricated, and they were for silicon grown on perforated graphite sheets. The data for the best one of them are given in Table SC-1 along with data for a companion Czochralski-grown control cell.

Table SC-1. SOLAR CELL DATA FOR A  
CONTIGUOUSLY COATED  
SILICON SHEET

Property	Contiguous Sheet	Control
AM0-Uncoated		
Cell area (cm <sup>2</sup> )	7.63	4.0
V <sub>oc</sub> (volts)	0.48	0.58
J <sub>sc</sub> (mA/cm <sup>2</sup> )	16.6	24.7
J <sub>sc</sub> -blue (mA/cm <sup>2</sup> )	7.8	9.3
J <sub>sc</sub> -red (mA/cm <sup>2</sup> )	9.0	15.3
Fill factor	0.46	0.74
Efficiency (%)	2.7	7.9
AM1-Coated		
Efficiency	4.3	12.1

### 2.1.6 Summary and Discussion

Contiguous silicon coatings were applied by substrate dipping to several types of porous carbon substrates. For both perforated graphite sheets and reticulated vitreous carbon, grain sizes on the order of 0.5 mm could be achieved with thick (0.5 mm - 1 mm) silicon coatings. Coating speeds up to 6 cm/min were demonstrated. The primary advantages of the growth method are the potential low-cost and -technology requirements. So far, solar cell fabrication has been plagued with difficulties, and the best cell performance to date has been an AM1 efficiency of 4.3%. Considerable shunting is exhibited as well as low values of V<sub>oc</sub> and J<sub>sc</sub>.

### 2.2 Edge-Supported Pulling

An elongated liquid silicon meniscus can be formed at the free surface of silicon in a crucible by inserting two parallel, vertical, wettable filaments,

connected by a cross-member, into the liquid. The ends of the meniscus are pinned at the filaments. The top is attached to the wettable cross-member, and the bottom rises from the free liquid surface. Under such conditions, a meniscus height of several mm can be achieved.

After such a meniscus is established, the filaments can be pulled upward. Silicon will then solidify on the cross-member, serving the same function as the original cross-member for attachment of the meniscus top. Thus, continued pulling of the filaments results in growth of a silicon sheet. The original cross-member may be made of the same materials as the filaments or it may be a silicon seed. A schematic of the edge-supported pulling process is shown in Fig. SC-6.

The filaments can be made from graphite. We have used sizes of 0.5 mm to 1.5 mm for ribbons up to 5-cm wide. Grains nucleate at the filament, and a fine grain structure exists within 2.2 mm to 3 mm of each filament. Beyond the fine-grained band, longitudinal grains of about 1 mm in width are typical for unseeded growth. Fig. SC-7 shows the NaOH-etched, 23-mm-wide central region of a 30-mm-wide sheet. Grains up to 2 cm in width have been attained with seeded growth, using a 5-cm filament spacing.

Neither thickness nor pulling speed have yet been explored intensively. The minimum thickness achieved was 0.2 mm. The highest pulling speed used was 25 mm/min. The sheets are thicker at the edges than in the Central regions, and the Meniscus is typically 2 mm to 3 mm higher in the central area than it is at the inner edges of the filaments.

Unseeded boron-doped sheets similar to the one shown in Fig. SC-7 have been fabricated into solar cells with AMI efficiencies equal to 84% of similarly processed Czochralski control cells. Diffusion lengths of up to 120  $\mu\text{m}$  were measured on the cell blanks before fabrication. Cell fill factors were identical to the values for the control cells (0.73), while both short-circuit current and open-circuit voltage were lower than the control values by about 7%. Seeded sheets have been processed into cells with over 13% AMI efficiency (90% of the CZ control cell value).

### 3.0 ACKNOWLEDGEMENTS

All sheet growth and material characterization results reported here were performed by T. Ciszek and J. Hurd. Solar cell fabrication and evaluation were performed by Applied Solar Energy Corp. and Solarex under SERI subcontract.

### 4.0 REFERENCES

1. Ciszek, T. F.; Schwuttke, G. H. NASA Tech Briefs. p. 432. Winter (1977).
2. Heaps, J. D.; Maciolek, R. B.; Zook, J. D.; Scott, M. W. Proceedings of the Twelfth IEEE Photovoltaic Specialists Conference. p. 147. Baton Rouge, Louisiana (1976).
3. Ciszek, T. F.; Schwuttke, G. H. J. Crystal Growth. Vol. 42: p. 483 (1977).

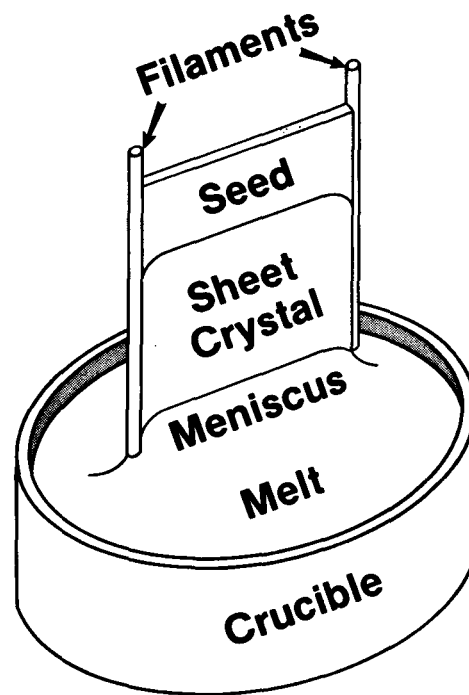


**Figure SC-6. Schematic Diagram for Edge-Supported Pulling of Silicon Sheets**

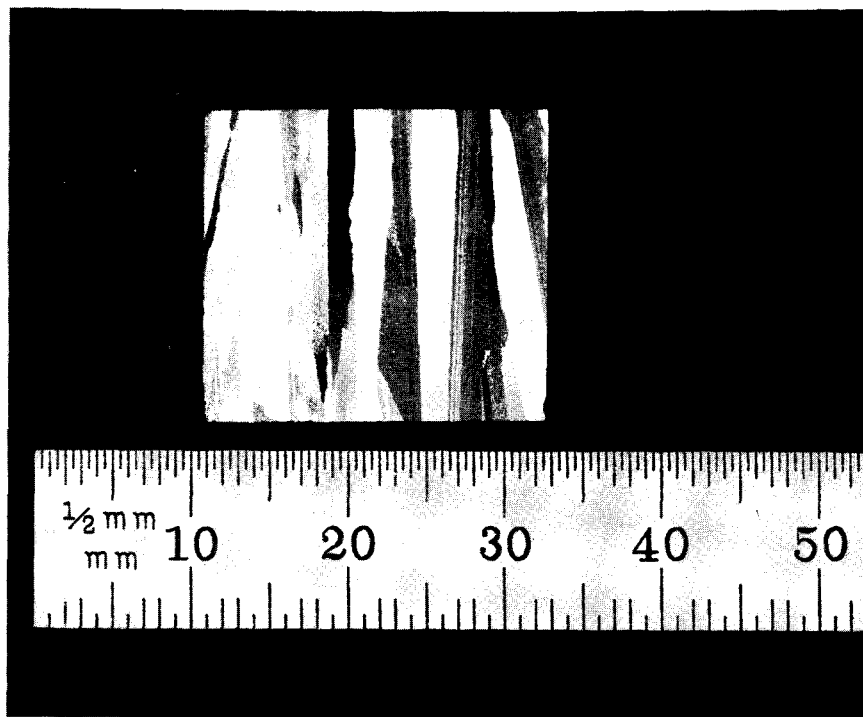


**Figure SC-7. Grain Structure of an Unseeded Silicon Sheet Grain by Edge-Supported Pulling**

## THICK-FILM TECHNOLOGY

Investigators: S. Hogan, K. Firor, R. Westfall

## 1.0 INTRODUCTION

The goal of the thick-film technology group is to define and research potential applications of the screen-printing process to low-cost future photovoltaic generation. This has led to two distinct research directions: first, the examination of metal systems for contacting to photovoltaic devices; and second, analysis of the screen printing of active semiconductor materials.

The thick-film technology (defined not by film thickness but rather by the technique of screen printing the desired film) has been successfully applied to the production of silicon cells for several years [1,2]. The process involves the printing of a metal-based ink to form the back contact and the front grid pattern. The well-documented systems in use involve printing aluminum on the back, followed by a silver overprint to allow for soldering. Upon firing the inks to sinter the metals, the aluminum diffuses into the silicon wafer and creates the back-surface fields [3]. The front contact is created by printing a silver-based ink through the grid-defining screen. After solder coating, the cells are ready for module assembly.

The scope of the metallization work in this group has been twofold. No recent survey of commercially available inks for front contacting has been done, so a comprehensive study of various inks was started. The second study has focused on determining the effects of an etching process recommended by the ink manufacturers. The results of this brief etching of the fired wafer in dilute hydrofluoric acid are controversial, and further understanding of this process will be valuable to manufacturers utilizing the contacting technique.

The procedure of successfully utilizing the thick-film technology for fabricating semiconductor-grade materials into a photovoltaic cell has been reported by only one group worldwide. In 1976, a Japanese group at Matsushita reported an 8% efficient cadmium-sulfide, cadmium-telluride (CdS-CdTe) photovoltaic cell [4]. The cell was fabricated using the screen printing process to form each layer and contacts. Because the thick-film technology requires no high vacuum, the cost effectiveness of such a technology applied in mass production would be excellent. Work has started on verification of this process as a viable technology.

## 2.0 RESEARCH AND RESULTS

2.1 Metallization

The initial impetus for a study of metallization systems for silicon cells came from several considerations. Because the thick-film laboratory was established only in July 1979, a breaking-in project was desired. The use of a nonvacuum technique of contact formation seemed attractive, and the use of thick films has been successfully implemented in microcircuit fabrication for

many years. One major cell producer, Arco Solar, employed screen printing on their production line and successfully demonstrated both the reliability and cost effectiveness of the procedure in a production situation. Past work with thick-film inks had indicated several shortcomings. The inks were often modified by the cell manufacturers to produce optimal results. This led to the ink manufacturers' not being aware of the limitations of their inks on silicon surfaces. It was also found that under previously used firing procedures, the series resistivity of the ink was too high, thereby limiting the current produced. The fired inks were subjected to an etch in hydrofluoric (HF) acid, and a subsequent increase in cell performance was attained. Figure TF-1 indicates a typical I-V curve before and after etch of a silver-based ink on a silicon cell. Despite intensive speculation, no clear conclusions had been reached as to the nature of the etching process. Work also indicated that a rapid anneal cycle precluded the necessity of an HF etch [5]. Yet another reason for performing a metallization study was the escalating cost of silver. It was hoped that some manufacturers might have developed base-metal inks suitable for use as front grids.

The study was initiated with a letter sent to all manufacturers of metallic inks. The letter detailed the study, the parameters to be evaluated, and the characteristics of the cells on which the front contacts would be printed. The manufacturers were asked to identify any metal inks they would recommend for the analysis and to provide complete information on the processing requirements. Response from the manufacturers was excellent, and the recommended inks were obtained. A grid pattern was designed for the 2-in. preprocessed wafers. More than 200 cells were run in an evaluation of the 12 silver-based inks and 8 nonnoble metal inks. Analyses of the printability of the inks, their ability to define a 125- $\mu$ m line width, their flow characteristics, and the I-V curves of the fired cells were done on the crevices. Preliminary adhesion measurements were also started.

Results of the study on the silver-based inks were quite encouraging--inks with low glass content and some doping are capable of producing good cells. Inks that had high glass contents generally exhibited a high series resistance that limited the efficiency of the cells. All of the silver-based inks required an HF etch to increase both the fill factor and current of the as-fired cells. The phosphate glass inks were very susceptible to loss of adhesion of the grid to the silicon if they were etched for more than 7 s in a 5% (by weight) solution of HF. The silicate glasses were less susceptible to this adhesion problem during short etch times, but also demonstrated peeling if over-etched. The phosphate glass inks, however, exhibited excellent I-V curves if they were first solder dipped, then etched for 90 s. This procedure appeared to have greatly decreased the time sensitivity of the etching, but was not as successful with silicate-glass inks.

The importance of the HF etch stimulated a program to determine the mechanism of cell improvement. This research was done jointly with members of the thick-film technology group and Tom Coyle and Joy Barrett of SERI's Materials Research Branch. Preliminary results indicate that the etching action of the silicon surface does not improve the output; but rather the improvement is caused entirely by a reaction within the fired ink. A removal of the associated glass is apparent, and work is being started to determine the actual mechanism that increases conductivity in the thick-film glass/silver matrix.

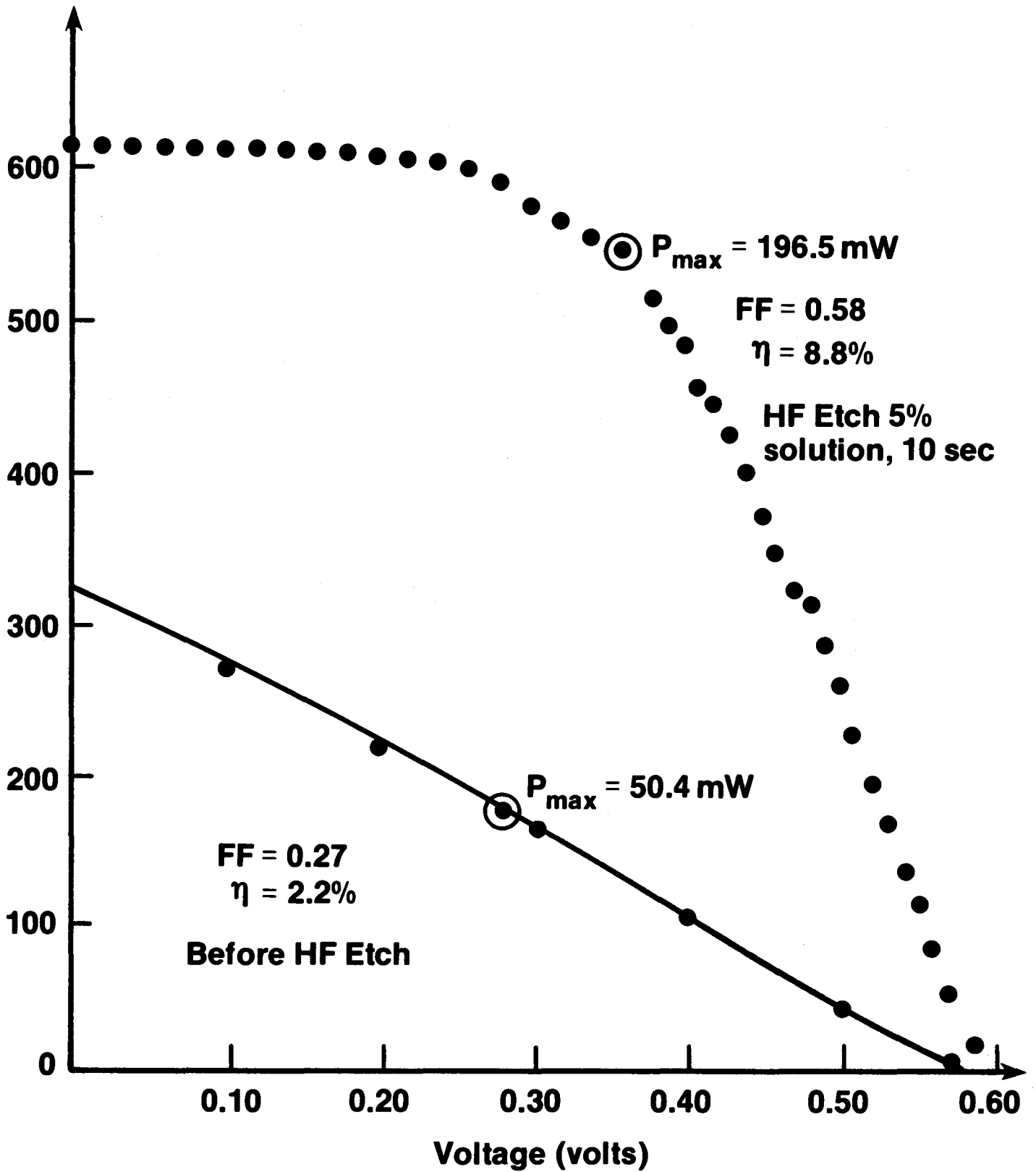


**Figure TF-1. I-V Curve of Single Crystal Silicon Solar Cell before and after HF Etch**



The work on the base-metal inks was discouraging. One aluminum-based ink and several nickel-, copper-, and chromium-based inks were tested. All inks indicated severe junction shunting when fired above 600°C, this being due to the high mobility of the metal atoms in the silicon. Normal open-circuit voltages were attainable, but the resultant short-circuit currents were typically less than 5 mA/cm<sup>2</sup>. This series resistance (and characteristic low conductivity of the metals) could be decreased (or circumvented) by coating the conductor grid with solder. Not only was this operation difficult, it also failed to increase the cell metal versus noble metal usage. For this reason, none of the commercially available base-metal inks was found to be acceptable for use in cells at present.

## 2.2 Active Layers

Research on the screen printing of active semiconductor layers represents a longer range area of high-risk research. The eventual goal is to screen print a CdS and CdTe solar cell [6]. The junction between the CdTe and the CdS would form the photovoltaic active region. Research during this period has focused on two areas, the screen printing of CdS and the vapor deposition of CdTe.

The printing and firing of films of CdS were successful. Attempts at firing films in a N<sub>2</sub> atmosphere resulted in high-resistivity materials. By manipulating the doping of the inks, in particular by using InCl<sub>3</sub> as a dopant to the CdS/CdCl<sub>2</sub> combination, the fired film's resistivity was greatly decreased. A 10% H<sub>2</sub>, 90% N<sub>2</sub> forming gas was used in the sintering furnace, and Table TF-1 shows the typical as-fired characteristics of the CdS. Measurements were made with a Van Der Pauw pattern defined using a specially designed test screen. A major drawback, however, is the porosity of the films. Scanning Electron Microscope (SEM) analyses show large areas of voids. It is anticipated that modifications in ink preparation and perhaps firing profile will help eliminate this problem. Film adhesion was excellent on both soda-lime glass and ITO-coated glass but exhibited significant peeling on quartz substrates.

The characteristics of the CdS-CdTe interface are not well understood. Rather than attempt a simultaneous characterization of both thick-film interfaces and the bulk properties of the device, it was decided to use the better defined vacuum deposition of CdTe. This would allow for a more controlled deposition of the CdTe on either a screen-printed or vacuum-evaporated CdS layer so that junction parameters could be more easily studied. The vacuum evaporation of the CdTe onto glass substrates with antimony doping has produced films with resistivities of 8 Ω cm to 12 Ω cm. Source and substrate temperatures were found to be very critical in the process, but with careful instrumentation, the films could be produced consistently. An effort to form a junction between the CdTe and screen printed CdS was unsuccessful, due to pinhole problems in the CdS.

Table TF-1. PROPERTIES OF SCREEN-PRINTED CdS

$\frac{t}{\text{(film thickness)}}$	$\frac{\text{film type}}{\rho \text{ (}\Omega \text{ cm)}}$	$\frac{\text{carrier concentration}}{\mu \text{ (cm}^2\text{/V-s)}}$
17 $\mu$	n 0.075	$1.02 \times 10^{19}$ 8

### 3.0 FUTURE DIRECTIONS

The anticipated future work in the metallization area will be threefold. (1) Adhesion and stability tests will be done on the supplied inks. Additionally, a full report on the study results will be written and made public in the next 6 months. (2) The analysis of the HF-etching procedure will continue with results also to be reported. (3) The advanced research area of base metallization represents a certain challenge. Because of the low costs associated with such potential applications, a feasibility analysis should be performed to find out if such systems can be used.

Futher directions in the active layer programs will be to continue the development of a denser screen-printed CdS. Work on developing CdTe inks will be initiated. The thin-film deposition work will continue to investigate the associated junction characteristics and to grow thin films of CdS for clean-junction formation.

### 4.0 SUMMARY

The thick-film technology group has examined 20 different thick-film inks for front contact metallization. Low glass content Ag inks with doping yield the best results, but with conventional firing require HF etching to improve the I-V curve of the device. The base-metal inks exhibited either junction shunting or too-high series resistance to make them acceptable. Work on both aspects will continue, as well as a fundamental study on the reaction of the HFD etch. Work with screen-printed CdS has shown that 0.1- $\Omega$  cm material can be produced, but the typical low densities obtained yield potential pinholing difficulties. Thin-film evaporation of CdTe has yielded p-type films of 10  $\Omega$  cm. These two techniques will be combined to study the junction of the CdS-CdTe device.

### 5.0 REFERENCES

1. Frisson, L. et al. "Screen Printed Contacts on Silicon Solar Cells with Low-Series Resistance," Proceedings of the 13th PV Specialists Conference, p. 590 (1978).
2. Field, M. B. "Thick-Film Materials for Silicon Photovoltaic Cell Manufacture," Final Report No. NASA CR-135134. Contract No. NAS 3-19441.

3. Ralph, E. L. "Recent Advancements in Low-Cost Solar Cell Processing," Proceedings of the 11th PV Specialists Conference. p. 315 (1975).
4. Nakayama, N. et al. "Ceramic Thin-Film CdTe Solar Cell," J. Appl. Phys. Vol. 15: p. 2281. Japan (1976).
5. Taylor, W. et al. "Array Automated Assembly, Phase II," Quarterly Report No. DOE/JPL 954853-78/3. Spectrolab, Inc. August 1978.
6. Ikegami, S.; Yamashita, T. Proceedings of the 21st Annual Electronic Materials Conference. Matsuskita Electric Industrial Co., Ltd. (1979).

## PHOTOVOLTAIC SURFACE AND INTERFACE RESEARCH

Investigators: L. L. Kazmerski, P. J. Ireland, P. Sheldon

## 1.0 INTRODUCTION

The Photovoltaics surface and interface program is presently composed of two research functions: the first and major activity is that of device and material analysis; the second is concerned with controlled device and material fabrication. This research activity is designed to complement the analysis function by providing thin-film and polycrystalline samples produced with specific electrical, physical, and chemical properties. This is a more recent research effort that, to date, has been largely concerned with laboratory development and program design.

For analysis, Auger electron spectroscopy (AES), secondary ion-mass spectroscopy (SIMS), and X-ray photoelectron spectroscopy (XPS) are currently used to examine interfaces (e.g., metal-semiconductor Schottky barrier, grain boundaries in polycrystalline materials) in order to correlate their chemical and compositional properties with device characteristics. The major areas of interest have been twofold:

- determination of the effects of impurities at surfaces, grain boundaries, and interfaces in photovoltaic materials and devices upon solar cell performance; and
- determination of device degradation mechanisms associated with elemental and compositional changes in solar cells that have undergone operational stresses.

This analysis activity has dealt with many of the major photovoltaic candidate materials, including Si, CdS, CdTe, Cu-ternary, InP, and GaAs, and has provided direct research interaction with both SERI in-house and outside research groups. From its inception, it has been the intention to provide a comprehensive and sophisticated surface analysis facility dedicated to photovoltaics research.

The material and device preparation activity in the surface and interface laboratory is being approached so that it complements the analysis efforts. Therefore, the primary interest was to provide a method capable of extremely controlled fabrication of thin-film layers and devices for diagnostic studies. Molecular beam epitaxy (MBE) provides the method for varying the grain size in films (permitting the investigation of grain-size problems), changing interface properties (doping, lattice match, formation of second phases), and investigating the effects of controlled-impurity levels and layer thickness. While MBE can be used effectively to provide samples with specific chemical, electrical, and physical properties for surface and interface analysis, the technique itself depends heavily upon in situ surface analysis (AES, SIMS, reflection high-energy electron diffraction) for controlled film fabrication.

## 2.0 LABORATORY CAPABILITIES

### 2.1 Surface Analysis Capabilities

The initial surface analytical instrumentation was chosen to provide, in a complementary manner, a wide range of information on solar cell materials and devices. Thus, while AES provides a great deal of spatial resolution (especially in its scanning mode) for elemental composition determination, its sensitivity limitations ( $\sim 0.1$  at. %) are compensated by the high sensitivity at low spatial resolution of SIMS. XPS, in turn, permits the exact determination of chemical composition of a layer. All are surface-sensitive techniques that give information typically from regions 10 Å to 20 Å in depth. Currently, two major surface analysis systems are in operation:

- Physical Electronics Industries Model 590 SAM/SIMS (Capabilities: scanning Auger microprobe (SAM) with 1500 Å minimum beam diameter; 1-10 atomic mass units SIMS; differentially pumped-ion source with 100- $\mu$ m minimum beam diameter; specimen introduction stage, which preserves ultrahigh-- $10^{-10}$  torr or better--vacuum analysis chamber pressure; specimen fracture stage; residual gas analyzer; specimen heating/cooling stage; microprocessor control; computer for data acquisition/reduction; graphic terminal display/control.)
- Physical Electronics Industries Model 550 XPS/SAM (Capabilities: High-resolution X-ray photoelectron spectroscopy; scanning-Auger microprobe with double-pass analyzer; differentially pumped-ion source, 100  $\mu$ m minimum beam diameter; angular resolved photoemission capability; specimen introduction stage with heating capability; computer for data acquisition/reduction; graphics terminal display/control.)

In addition, electron beam-induced current (EBIC) capabilities have been designed and incorporated into each of the systems. This permits the in situ electrical evaluation of samples being analyzed by the surface techniques. Thus, it is possible to directly correlate the results of a chemical/compositional investigation with an electrical characterization.

### 2.2 Preparation Capabilities

The system (Perkin-Elmer Physical Electronics Division Model 400 Molecular Beam Epitaxy) provides ultrahigh vacuum in each chamber, with the analysis chamber ion-pumped and the growth cryo-pumped. Eight sources are microprocessor controlled. AES and SIMS are provided in the analysis chamber. Reflection high-energy electron diffraction (RHEED), residual gas analysis, and quadrupole mass analysis are incorporated in the growth station. A sample introduction system preserves the clean, UHV conditions of the growth and analysis chambers.

### 3.0 RESEARCH SUMMARY

It is evident that photovoltaic device performance depends both on the quality of the materials involved in its makeup and the integrity of the numerous interfaces (junctions, oxide-semiconductor, metal-semiconductor, metal-oxide, grain boundaries, etc.) between and within these material layers. The focus of this program has been the application of the laboratory's surface analysis capabilities to the determination of material quality, and especially to the investigation of interface problems in photovoltaic devices [1-12]. The surface analysis capabilities available in the laboratory (AES, SAM, SIMS, XPS) provide for the simultaneous and complementary acquisition of information on the composition and chemistry of photovoltaic layers and interfaces. An example of the application of these techniques is presented in Figs. PS-1-5. These data were obtained from a GaAs-oxide structure for a Schottky-barrier solar cell in which the LPE GaAs film had purposely been grown to be polycrystalline (3- $\mu\text{m}$  grain size) [6]. Figure PS-1 presents an AES survey scan of the poly-GaAs surface, indicating the expected presence of the Ga and As signals and no other element response. However, comparison of these data to a standard GaAs spectrum (Fig. PS-2) indicates some differences in peak shape and position of the Ga signals in the 1000 eV to 1050 eV range (these differences are highlighted in the expanded spectra of Fig. PS-3). A SIMS survey taken on these same surfaces is presented in Fig. PS-4. Figure 4a shows the positive SIMS response for the standard GaAs (Fig. PS-4c), and the LPE GaAs (Fig. PS-4d) also confirms the presence of oxygen in the LPE film. Subsequently, the film was fractured in UHV, and the internal surfaces produced by fracturing were examined. The grain boundaries are now perpendicular to the AES beam. In some regions of the grain boundaries, the AES data (Fig. PS-5) show the presence of Ga-oxide layers. This oxide was confirmed to be  $\text{Ga}_2\text{O}_3$  from the XPS data presented in the insert. In this, the Ga 3d peak in GaAs is shown by the dashed line. The 3d Ga peak from the oxide is shifted by 0.9 eV from the GaAs position. This chemical shift identifies the trivalent oxide state. Consequently, SIMS was used (with greater impurity sensitivity than AES) to detect the presence of oxygen in the poly-GaAs not seen in the normal AES surface survey. The localization of the oxide was then confirmed to be on the grain boundary by using the in situ fracturing technique. Finally, the chemical state of the oxide was identified using XPS. This type of complementary analysis is very powerful in uncovering material and interface problems.

A wide variety of photovoltaic candidate materials and material systems were examined in this laboratory. The major results dealt with polycrystalline Si, GaAs, InP and CdS. A summary of this surface and interface research includes:

- First direct physical evidence for the segregation of impurities to grain boundaries in cast and directionally solidified multigrained Si. The impurity phases were determined to be localized and nonuniform [2-4,11].
- Correlation of the electrical properties of Si grain boundaries using EBIC with the compositional makeup of the same boundary regions [4,13].
- Comparative study of the chemistry and composition of oxides grown by low-temperature wet and dry processes on GaAs, identifying the phase composition and uniformity of each type [5,7].

PS-4

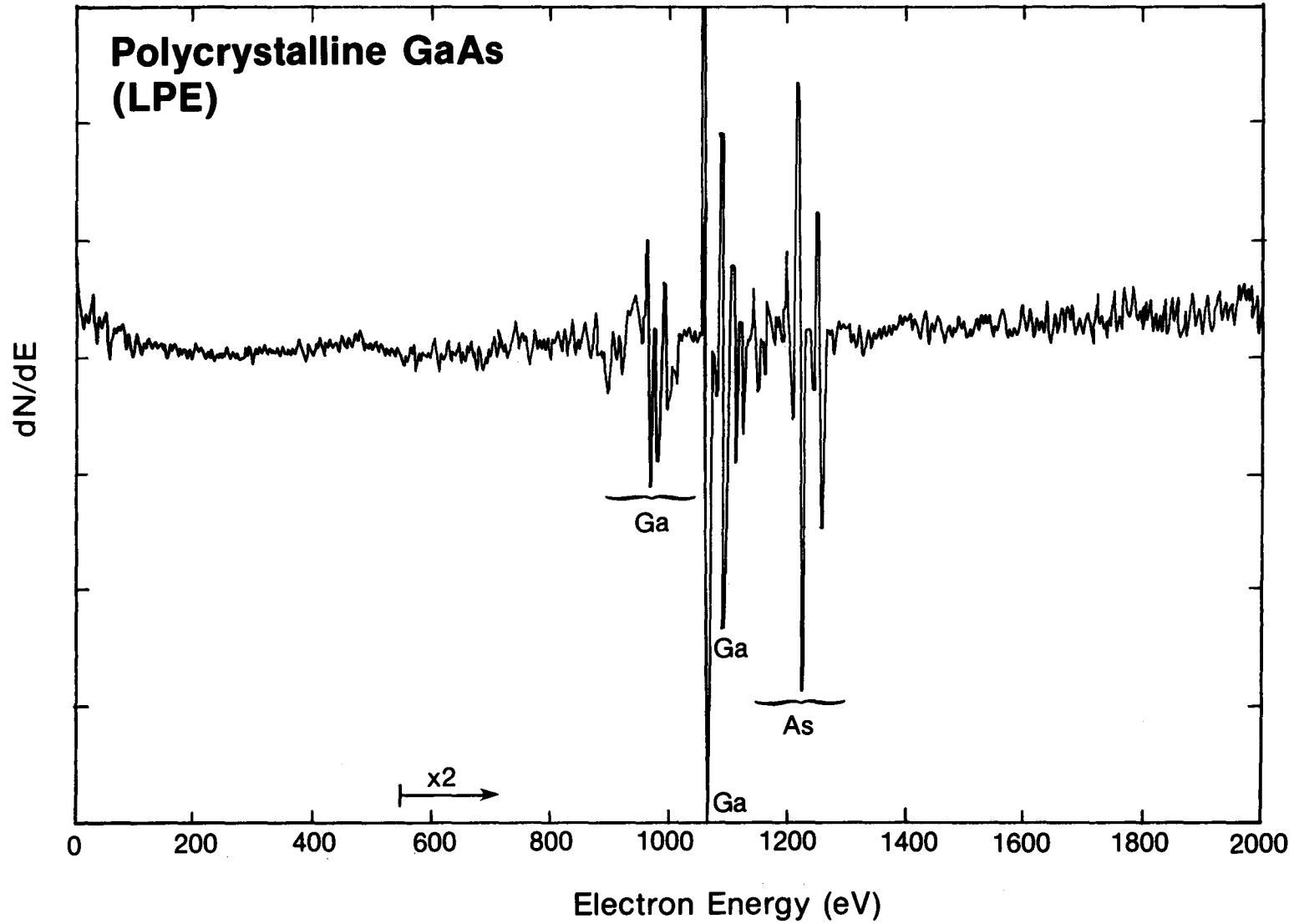
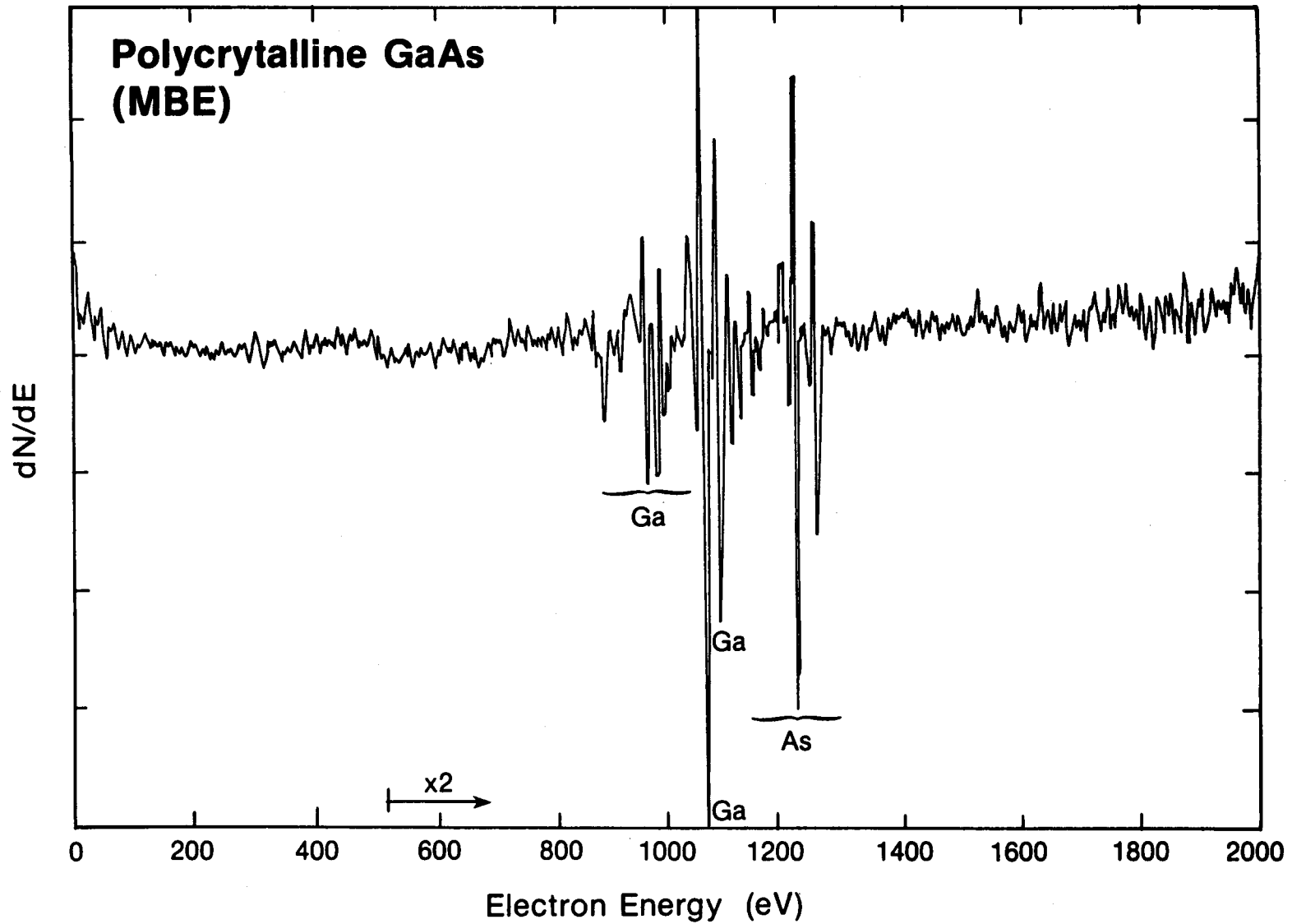
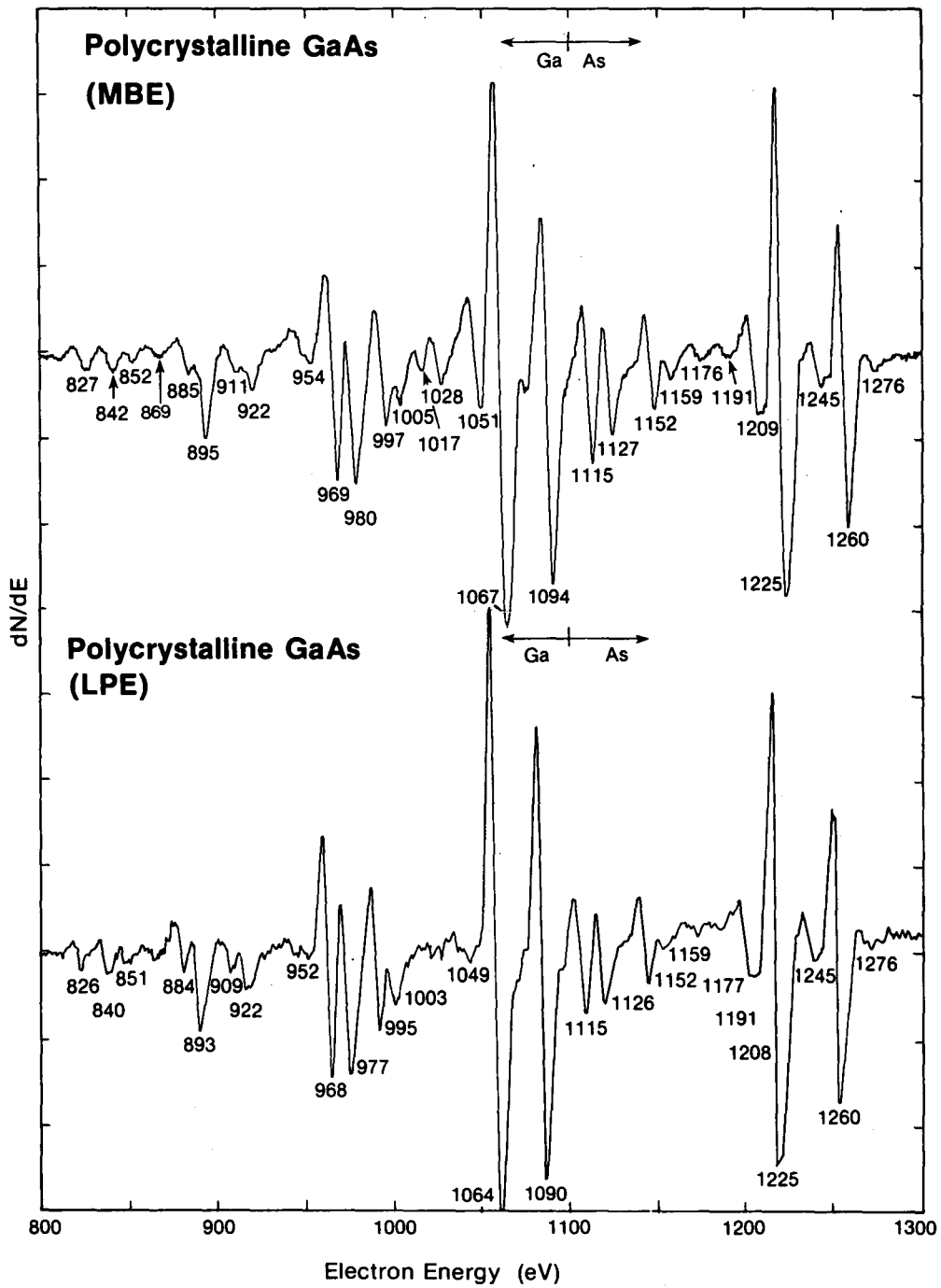


Figure PS-1. AES Spectrum of Polycrystalline GaAs Grown by LPE ( $E_p = 5$  kV,  $I_p = 0.15 \mu\text{A}$ .)



**Figure PS-2. AES Spectrum of Polycrystalline GaAs Grown by MBE, Taken under Same Conditions as Figure PS-1**





**Figure PS-3. Expanded AES Spectra Showing 800-1300 eV Range for LPE and MBE Samples in Figures PS-1 and PS-2 (Note positions and shapes of 1005, 1017, 1028 and 1051 eV peaks.)**

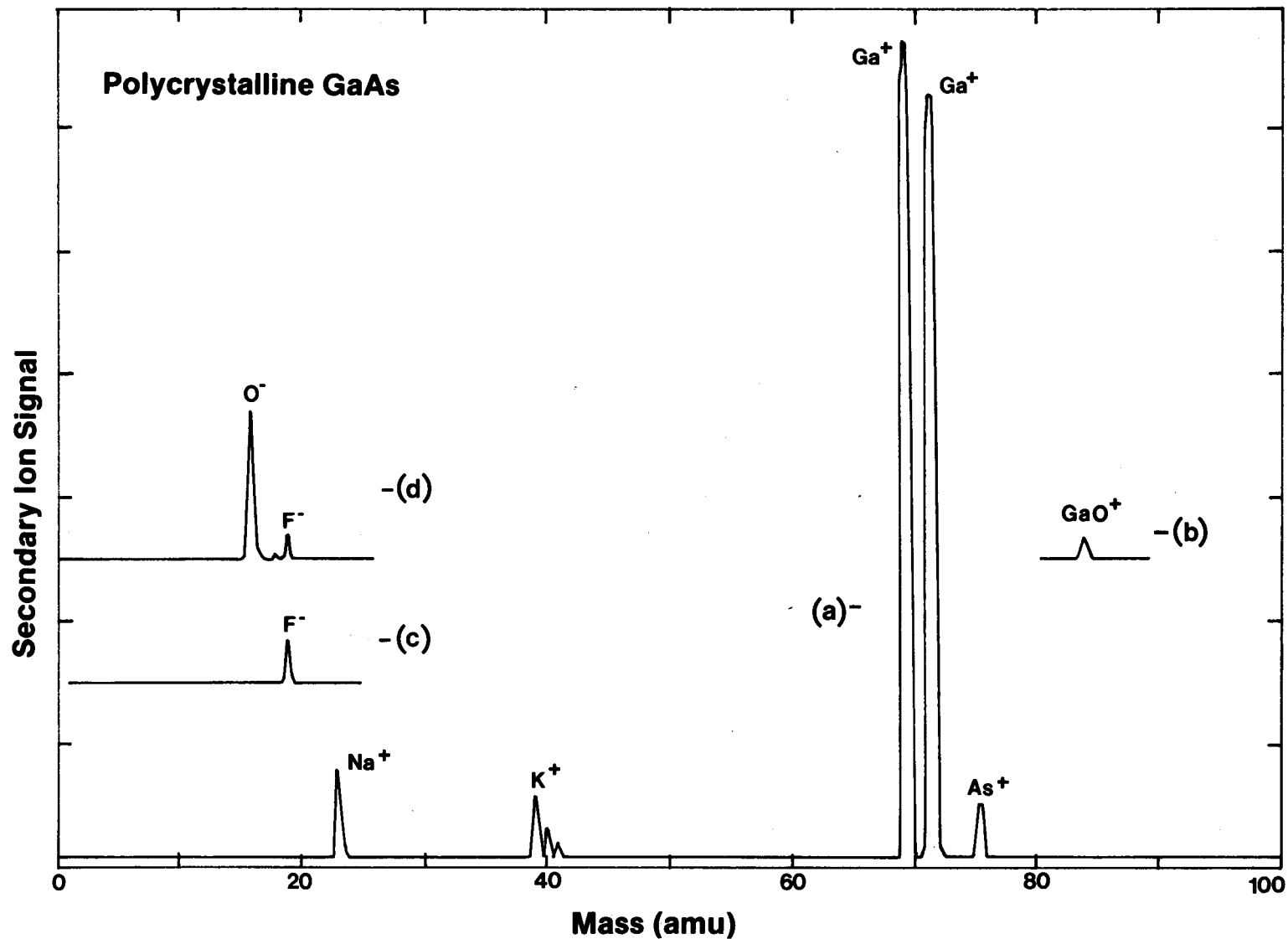


**Figure PS-4. SIMS Spectra from LPE and MBE Polycrystalline GaAs Surfaces** [(a) Total positive SIMS spectrum of MBE sample; (b) portion of positive SIMS spectrum of LPE sample showing presence of oxide species; (c) negative SIMS spectrum of MBE GaAs (no oxygen present); and (d) negative SIMS spectrum of LPE material indicating presence of oxygen in film.]

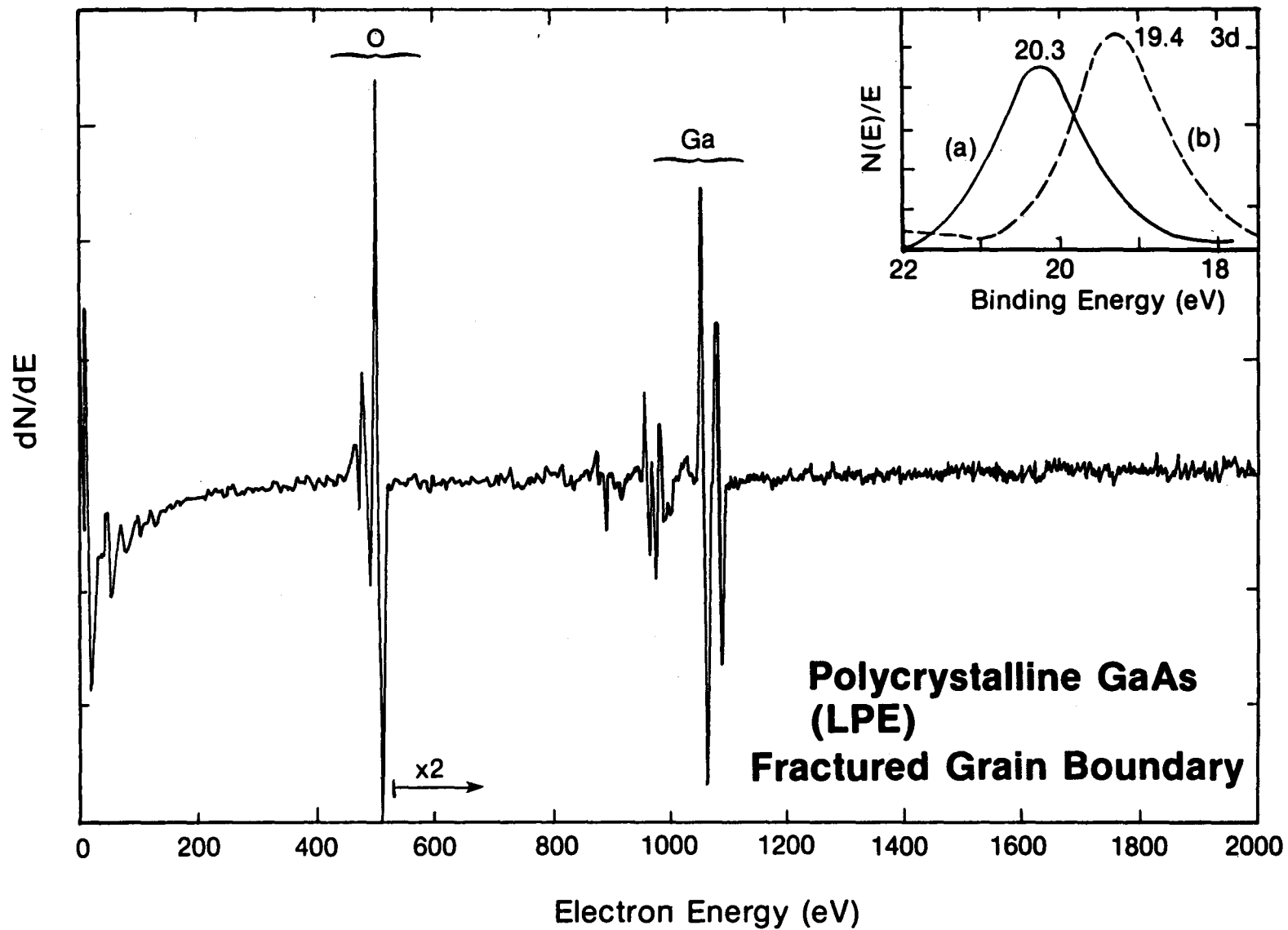


**Figure PS-5. AES Spectrum of LPE Polycrystalline GaAs Fractured to Expose Grain Boundary**  
 (Data are taken approximately  $1 \mu\text{m}$  below film surface under minimum beam diameter conditions. Insert shows XPS data; (a) this region, indicating  $\text{Ga}_2\text{O}_3$  presence; (b) reference signal for Ga 3d peak from GaAs.)

- Identification of trace impurity and dopant buildup at oxide-GaAs-grain boundary (sulfur-doped) interfaces [7].
- Angular-resolved XPS identification and relative contributions of  $As_2O_5$ ,  $As_2O_3$ , and  $Ga_2O_3$  in anodic oxides on poly-GaAs [5].
- Investigation of metal/poly-GaAs Schottky-barrier interfacial chemical interactions. Results include the identification of the  $Ga_2Au$  phase at the interface of the Au/GaAs device; the confirmation of the out diffusion of Ga from the GaAs into the Au metallization; the demonstration of the use of an intermediate oxide layer as an effective diffusion barrier for the Au-GaAs system; the identification and confirmation of Ag as a more suitable and stable metal barrier material [14].
- The determination of the grain boundary diffusion coefficient of Au into poly-GaAs [14].
- Study of grain boundary passivation in poly-GaAs by oxidation, including the identification of the phase composition of oxidized boundaries and the oxide distribution [6,7].
- Study of the chemistry and composition of tunneling oxide/InP interfaces [8,12].
- Surface analytical determination of MBE-grown Cu-ternary layers and chemical phase investigations of the CdS/CuInSe<sub>2</sub> interface [1].

A major innovation incorporated by this laboratory in the application of the surface analysis methods to the investigation of grain-boundary chemistry has been the in situ, ultrahigh vacuum fracturing procedure. This technique has been very useful in exposing the internal surfaces of films, while avoiding any artifacts which could be generated in less clean environments.

MBE growth of Cu-ternary films which was initiated as a cooperative research program before the availability of the SERI in-house program, continued. The growth parameters to produce low-resistivity CuInSe<sub>2</sub> layers were firmly established. Optical and electrical characterizations of these films were carried out in order to document the quality of such MBE-grown layers. A single-crystal CuInSe<sub>2</sub>/CdS MBE-produced device, with AM1 4.7% conversion efficiency was produced [1]. This device work is continuing in an effort to address several problems which have limited device performance.

At SERI, the MBE growth and characterization of undoped and doped GaAs thin films were initiated. These studies provide the first stages for the fabrication of single- and multiple-junction, high-efficiency solar cells. High-quality single-crystal layers have been demonstrated, and controlled n- and p-type doped films with reasonable mobilities have been produced. Growth rates and control have been implemented, and actual device fabrication is expected to begin in the summer of 1980.

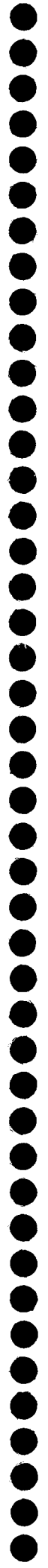
#### 4.0 REFERENCES

1. White, F. R.; Clark, A. H.; Graf, M. C.; Grindle, S. P.; Kazmerksi, L. L. "Growth of CuInSe<sub>2</sub> Films Using Molecular Beam Epitaxy." J. Vac. Sci. Technol. Vol. 16: p. 287 (1979).

2. Kazmerski, L. L.; Ireland, P. J. "Correlation of Grain Boundary Electrical Properties with Grain Boundary Impurities in Multigrained Silicon Using Surface Analytical Techniques." Proc. Photovoltaics Materials and Development Workshop: Focus on Polycrystalline Thin Films. pp. 145-151. Presented at Arlington, Va. Solar Energy Research Institute. Golden, Colo. (1979).
3. Kazmerski, L. L.; Ireland, P. J.; Ciszek, T. F. "SIMS Identification of Impurity Segregation to Grain Boundaries in Cast Multigrained Silicon." Proc. Second Int. Conf. on Secondary Ion Mass Spectroscopy. pp. 103-106. Presented at Palo Alto, Calif. Springer-Verlag, N.Y. (1979).
4. Kazmerski, L. L.; Ireland, P. J.; Ciszek, T. F. "Electrical and Compositional Properties of Grain Boundaries in Multigrained Silicon Using Surface Analysis Techniques." J. Vac. Sci. Technol. Vol. 17: p. 34 (1980).
5. Ireland, P. J.; Kazmerski, L. L.; Chu, S. S.; Lee, Y. T. "A Comparative Study of Wet and Dry Oxides on Polycrystalline GaAs by AES and SIMS." J. Vac. Sci. Technol. Vol. 17: p. 521 (1980).
6. Kazmerski, L. L.; Ireland, P. J. "Evidence for Grain Boundary Passivation by Oxidation in Thin-Film Polycrystalline GaAs Solar Cells." J. Vac. Sci. Technol. Vol. 17: p. 525 (1980).
7. Kazmerski, L. L.; Ireland, P. J.; Sheldon, P. "Grain Boundary Chemistry and Its Effects Upon the Performance of Polycrystalline Solar Cells." Proc. 14th IEEE Photovoltaics Spec. Conf. Vol. 14. San Diego, Calif. (1980).
8. Chu, T. L.; Chu, S. S.; Lin, C. L.; Chang, C. T.; Tzeng, Y. C.; Kuper, A. B.; Kazmerski, L. L.; Ireland, P. J. "Indium Phosphide Films for Photovoltaic Devices." Proc. 14th IEEE Photovoltaics Spec. Conf. Vol. 14. San Diego, Calif. (1979).
9. Kazmerski, L. L.; Ireland, P. J. "A Study of Interface Problems in Polycrystalline GaAs Schottky-Barrier and MIS Solar Cells." Surface and Interface Analysis. Vol. 1: p. 144 (1980).
10. Kazmerski, L. L. "Characterization of Grain Boundaries in Solar Cell Materials." Proc. Photovoltaics Advanced R&D Annual Review Meeting. pp. 271-286. Denver, Colo. (invited) Solar Energy Research Institute. Golden, Colo. (1979).
11. Kazmerski, L. L.; Ireland, P. J.; Ciszek, T. F. "Evidence for the Segregation of Impurities to Grain Boundaries in Multigrained Silicon Using AES and SIMS." Appl. Phys. Lett. Vol. 36: p. 323 (1980).
12. Kazmerski, L. L.; Ireland, P. J.; Sheldon, P.; Chu, T. L.; Chu, S. S.; Lin, C. L. "A Comparison of Low-Temperature Oxides on Polycrystalline InP by AES, SIMS, and XPS." J. Vac. Sci. Technol. Vol. 17 (1980).
13. Kazmerski, L. L.; Ireland, P. J. "Impurities at Grain Boundaries." J. Electrochem. Soc. (in press) (1980).

14. Kazmerski, L. L.; Ireland, P. J. "A Study of Interface Problems in Polycrystalline GaAs Schottky-Barrier and MIS Solar Cells." Surface and Interface Analysis. Vol. 1: p. 144 (1979).

**SERI** 



<b>Document Control Page</b>	1. SERI Report No. PR-611-737	2. NTIS Accession No.	3. Recipient's Accession No.
4. Title and Subtitle  Photovoltaic Research Semiannual Report		5. Publication Date July 1980	
7. Author(s) Alex Zunger		6.	
9. Performing Organization Name and Address  Solar Energy Research Institute 1617 Cole Boulevard Golden, Colorado 80401		8. Performing Organization Rept. No.	
		10. Project/Task/Work Unit No. 3221.10	
		11. Contract (C) or Grant (G) No. (C) (G)	
12. Sponsoring Organization Name and Address		13. Type of Report & Period Covered Technical Progress Report	
15. Supplementary Notes		14.	
16. Abstract (Limit: 200 words)  This report covers the research activities in SERI's Photovoltaic Research Branch during the period 1 October 1979 to 31 March 1980. It includes separate reports on: solid-state theory, high-efficiency cells, thin-film cells, silicon purification, silicon crystallization, thick-film technology, surface and interface analysis, and growth of GaAs and related compounds by metal-organic chemical vapor desposition.			
17. Document Analysis a. Descriptors Photovoltaic Cells; Research Programs; Solar Cells; Semiconductor Devices; Semiconductor Junctions; Computerized Simulation; Silicon Solar Cells; Thin Films; Thick Films; Films; Solid State Physics; Surfaces; Gallium Arsenides; Interfaces; Doped Materials; Crystal Doping; Vapor Deposited Coatings; Vanadium Oxides; Crystallization; Screen Printing; Auger Electron Spectroscopy; Epitaxy; Molecular Beams; Photoelectron Spectroscopy; Ion Spectroscopy; X-ray Spectroscopy; Spectroscopy; Schottky-Barrier Diodes; Zinc Selenides; Germanium Compounds; Tunnel Diodes; Photoluminescence; Electron Spin Resonance. c. UC Categories 63			
18. Availability Statement National Technical Information Service U.S. Department of Commerce 5285 Port Royal Road Springfield, Virginia 22181		19. No. of Pages 104	
		20. Price \$6.50	





National Renewable  
Energy Laboratory



02LIB119318